Programmable Wavelength Filters in Silicon Photonics

Mi Wang

Doctoral dissertation submitted to obtain the academic degree of
Doctor of Photonics Engineering

Supervisors
Prof. Wim Bogaerts, PhD - Umar Khan, PhD

Department of Information Technology
Faculty of Engineering and Architecture, Ghent University

GHENT
UNIVERSITY

Members of the Examination Board

Chair

Prof. Filip De Turck, PhD, Ghent University

Other members entitled to vote

Qingzhong Deng, PhD, imec

Prof. Bart Kuyken, PhD, Ghent University

Prof. Nicolas Le Thomas, PhD, Ghent University

Prof. David Marpaung, PhD, Universiteit Twente, the Netherlands

Prof. Pieter Rombouts, PhD, Ghent University

Supervisors

Prof. Wim Bogaerts, PhD, Ghent University

Umar Khan, PhD, Ghent University

Acknowledgement

Table of Contents

List of Figures

List of Tables

List of Acronyms

A

AWG	Arrayed Waveguide Grating
ARMA	Autoregressive Moving Average
ADC	Asymmetric Directional Coupler

B

BDC	Broadband Directional Coupler
BPM	Beam Propagation Method
BPF	Bandpass Filter

C

CMT	Coupled Mode Theory

D

DC	Directional Coupler

E

EME	Eigenmode Expansion Method

F

FDM	Finite Difference Method
FMM	Film Mode Matching
FSR	Free Spectral Range
FDTD	Finite Difference Time Domain

G

GA	Genetic Algorithm
GUI	Graphical User Interface

L

LUT	Look Up Table
LIDAR	Light Detection And Ranging
LPF	Low Pass Filter

M

MMI	Multi-mode Interferometer
MZI	Mach-Zehnder Interferometer

O

OADM	Optical Add-Drop Multiplexer

S

SOI	Silicon on Insulator
SiN	Silicon Nitride

SOA   Semiconductor Optical Amplifier
SiPh   Silicon photonics

T

TMM   Transfer Matrix Method

U

UWB   Ultra Wide Band

V

VTT   Technical Research Centre of Finland

W

WDM   Wavelength Division Multiplexer

X

XML   eXtensible Markup Language

Nederlandse samenvatting
–Summary in Dutch–

Geïntegreerde fotonicatechnologie maakt het mogelijk om grote en complexe fotonische systemen op een chip te implementeren. Vandaag de dag worden deze chips steeds ontworpen voor één specifieke functie. Fotonische mesh-circuits bestaande uit een netwerk van golfgeleiders, afstembare koppelaars en optische faseverschuivers [1] maken het echter mogelijk om universeel programmeerbare fotonische chips te maken die geprogrammeerd kunnen worden om verscheidene functies uit te voeren. Met zulke technologie is er de mogelijkheid om prototypes te testen en zo kan het ontwikkelproces voor nieuwe producten en toepassingen versneld worden. Dergelijke programmeerbare chips voor universeel gebruik moeten echter nog op de volgende vlakken verder ontwikkeld worden:

- de basisbouwstenen - afstembare koppelaars en optische faseverschuivers

- besturings- en optimalisatie-algoritmen

- chipverpakkingstechnieken

- toepassingsmogelijkheden

In dit proefschrift werken we naar deze technologie toe, en in het bijzonder onderzoeken we de mogelijkheden om programmeerbare golflengtefilters te implementeren.

Hierbij kijken we naar enkele fundamentele bouwstenen voor dergelijke circuits: koppelaars waarbij de signalen van twee golfgeleiders worden geschakeld. We introduceren een ontwerp voor een breedbandige koppelaar, alsook een tolerant breedbandig-afstembaar koppelcircuit.

De directionele koppelaar is een essentiële bouwsteen van veel fotonische circuits. De koppelaar wordt gebruikt voor het splitsen en combineren van licht. Een compacte, golflengte-onafhankelijke directionele koppelaar is zeer gewenst, vooral voor telecomtoepassingen zoals golflengtemultiplexering [2] en het doorschakelen van signalen [3].

Een belangrijke functie van de universeel programmeerbare chips is het filteren van licht op basis van golflengte. Golflengte filters op optische chips worden veelal gedefinieerd door licht langs verschillende paden te sturen en dan opnieuw te combineren. Afhankelijk van het padlengteverschil en de golflengte van het licht

krijgt men een hoge of lage transmissie.Dit soort functies kan men ook implementeren in een universeel programmeerbaar mesh van golfgeleiders, maar de discrete bouwstenen van dergelijke circuits zorgt er voor dat de filters hoge verliezen en een kleine vrij spectraal bereik hebben (Eng: *free spectral range* of (FSR)).

Daarom stellen we hier een gespecialiseerd programmeerbaar filtercircuit voor, bestaande uit een gekoppelde ringresonator in een Mach-Zehnder interferometer (MZI). We hebben niet alleen het circuit ontworpen, maar ook de synthese- en optimalisatiealgoritmes om het circuit te configureren. Een dergelijk programmeerbaar filter zou gebruikt kunnen worden in fotonische systemen zoals een optische interleaver of een pompdempingsfilters.

1   Passieve component - breedbandige koppelaar

Een breedbandige koppelaar kan op vele manieren worden gerealiseerd. Voor de 2×2 asymmetrische directionele golfgeleiderkoppelaar [4] is aangetoond dat de component breedbandig is (werkt over een breed golflengtebereik), alsook compact van formaat en eenvoudig van structuur. Bovendien is de component eenvoudig te fabriceren.
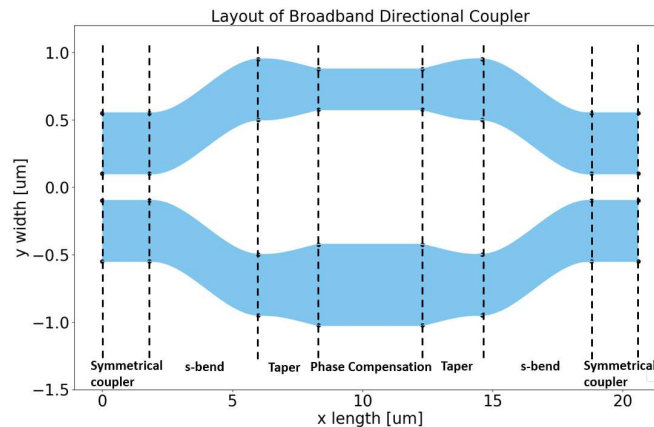
Figuur 1: Schematische tekening van een breedbandige directionele koppelaar bestaande uit een Mach-Zehnder interferometer (MZI)

De layout van het ontwerp wordt gegeven in Fig. **??**, en is gelijkend op een Mach-Zehnder interferometer(MZI). We zien dat de component is samengesteld uit 4 onderdelen: een symmetrische koppeling, een s-bocht, een taper en een fasecompensatiegedeelte. Deze lay-out is gekozen als veberting op de lay-out gegeven in [4] omdat we hebben geconstateerd dat de parasitaire koppeling in het fasecompensatiegedeelte en het tapergedeelte niet kon worden genegeerd.

We vergroten niet enkel de afstand tussen de golfgeleiders in de fasecompen-

satiesectie, maar we hebben ook een meer rigoureuze simulatiemethode gebruikt
in vergelijking met transfermatrixmethode (TMM) in [4] - Eigenmode expansion
(EME) voor de optimalisatie van de component. Deze methode is tijdrovend in
vergelijking met TMM, maar is nog steeds acceptabel omdat het variëren van de
lengte snel is vanwege de interne werking van het EME algoritme.

We bouwen het breedbandkoppelingsmodel met EME in de simulatiesoftware
FIMMPROP. Het initiële ontwerp is symmetrisch, waarbij de lengte van de ingang-
en uitgangskoppelaar hetzelfde zijn. Vervolgens worden twee parameters ingesteld
als variabelen in de volgende optimalisatiestap, namelijk de lengte van de ingangs-
en uitgangskoppelaar en de lengte van de fasecompensatiesectie. In dit proefschrift
wordt het Kriging-optimalisatie-algoritme [5] uit de ooDACE [6] toolbox gebruikt.
Deze routines zijn ontwikkeld door de Universiteit Gent, en wij gebruiken ze om
de bandbreedte van het breedbandkoppelingsmodel te optimaliseren voor verschil-
lende doelwaarden van de vermogenkoppeling.

Door gebruik te maken van de optimalisatiemethode Kriging worden enkele
geoptimaliseerde ontwerpen geselecteerd en getoond in Fig. **??**. De gedetailleerde
ontwerpinformatie voor geoptimaliseerde ontwerpen wordt gegeven in Tabel 3.1:

Doel	simulatie uitkomst	fout	ontwerpparameters
$k = 0.3$	$k = 0.302$	$\delta = 0.04$	$L_1 = 12.5787um$ $L_2 = 8.470um$
$k = 0.5$	$k = 0.508$	$\delta = 0.0363$	$L_1 = 9.905um$ $L_2 = 8.646um$
$k = 0.7$	$k = 0.724$	$\delta = 0.0162$	$L_1 = 7.234um$ $L_2 = 8.793um$
$k = 0.9$	$k = 0.9$	$\delta = 0.0173$	$L_1 = 3.079um$ $L_2 = 8.958um$

Tabel 1: ontwerpparameters van de geoptimaliseerde koppelaars in Fig. 9

We merken dat de dispersie groter is in de breedbandige ontwerpen met klei-
nere koppelwaarden. Zoals we kunnen zien in Tabel 3.1, verandert de lengte van
de ingangs- en uitgangskoppelaar nogal voor verschillende ontwerpen, maar de
lengte van de fasecompensatiesectie blijft min of meer constant.

Het ontwerp kan verder worden geoptimaliseerd door het aantal optimalisatie-
parameters te vergroten.

2 Tolerant, breedbandig afstembaar 2×2 koppelcircuit

Waar we in een eerste stap een koppelaar hebben geoptimaliseerd met een statische
koppelsterkte, hebben we voor een programmeerbaar circuit een basisbouwsteen
nodig waarbij de koppeling afstembaar wordt, zoals getoond in Fig. 10. Om te
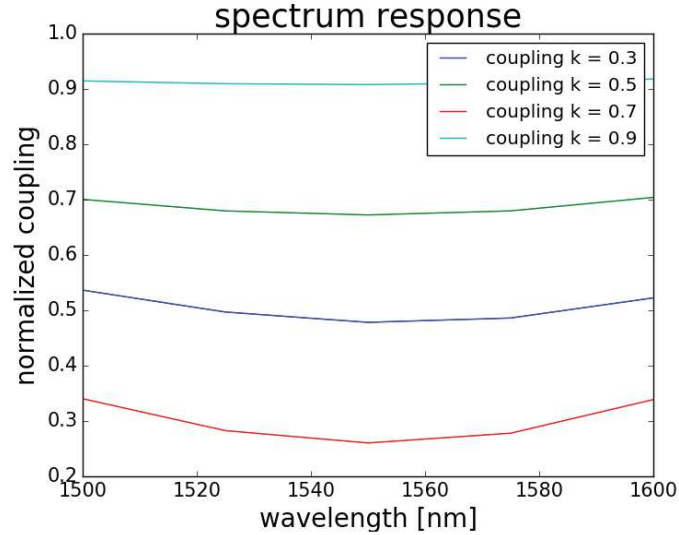
Figuur 2: Spectrale respons van enkele geoptimialseerde ontwerpen

beschikken over voldoende configuratiemogelijkheden hebben we in zo een component ten minste twee instelbare parameters p_1 en p_2 nodig om zowel de vermogenssplitsing κ als de faseverschuiving $\Delta\phi$ onafhankelijk van elkaar te kunnen afregelen. Dit noemen we een 2×2 optische poort. Een gebruikelijke manier om een dergelijke afstembare 2×2 koppelaar te implementeren is een gebalanceerde Mach-Zehnder interferometer (MZI) met een elektrisch-aangestuurde faseverschuiver in elke arm.

De MZI is opgebouwd uit twee statische 50:50 koppelaars (bv. de directionele koppelaars besproken in de vorige sectie), verbonden met twee golfgeleiders met geïntegreerde faseverschuivers. Voor die laatste worden veelal eletrische weerstanden gebruikt die de golfgeleiders lokaal opwarmen. De koppelingsrespons van de MZI kan van minimum naar maximum worden verschoven door de fasevertraging af te stemmen tussen 0 en π. Om het volledige koppelingsbereik van 0-100% te verkrijgen, moeten de twee statische koppelaars echter een perfecte 50:50-splitsingsbalans hebben, wat niet eenvoudig te ontwerpen is over een breed golflengtebereik [8]. Alhoewel onze eerder beschreven component dicht in de buurt komt, is die nog steeds gevoelig aan variatie bij fabricage.

Als oplossing breiden we de traditionele MZI uit met een tweede trap, waarbij we opnieuw een koppel golfgeleiders met een fasevertrager inbouwen. In dit werk stellen we het ontwerp van deze tweetraps-MZI als volgt voor: Fig. 11.

We demonstreren dat het circuit tolerant is voor fabricage-variatie en golflengte-onafhankelijk is door de volgende simulatie. We nemen aan dat het circuit bestaat uit imperfecte DC's met een koppelingsverhouding van 40:60 bij 1550 nm. In Fig. 12 tonen we de vermogenskoppeling η bij 1550 nm (witte contouren), en be-

$$\begin{bmatrix} B_1 \\ B_2 \end{bmatrix} = \begin{bmatrix} \cos\dfrac{\theta}{2} & j\sin\dfrac{\theta}{2} \\ j\sin\dfrac{\theta}{2} & \cos\dfrac{\theta}{2} \end{bmatrix} \cdot \begin{bmatrix} e^{j\phi_1} & 0 \\ 0 & e^{j\phi_2} \end{bmatrix} \begin{bmatrix} A_1 \\ A_2 \end{bmatrix}$$
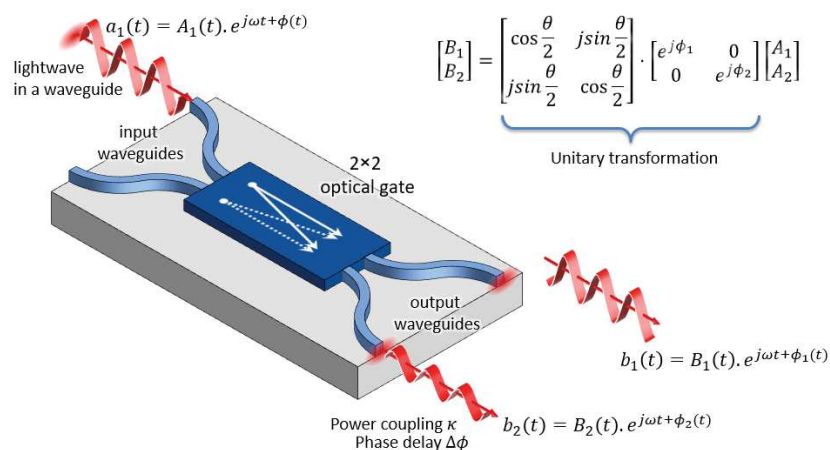
Figuur 3: Een 2 × 2 optische poort mengt de golven van twee ingangsgolfgeleiders, waardoor zowel de vermogenskoppeling als de fasevertraging wordt gecontroleerd [7]. Een gebruikelijke manier om een afstembare 2 × 2 koppelaar te implementeren is een gebalanceerde Mach-Zehnder interferometer (MZI) met faseverschuiver in elke arm.

dekken we deze met de maximale afwijking $\Delta\eta$ binnen het golflengtebereik van 1525-1575 nm. Voor elke gewenste koppelingswaarde kunnen we de twee faseverschuivers zo afstemmen dat we deze koppelingswaarde binnen 3% krijgen over het gehele golflengtebereik voor een bijna uniforme respons. We kunnen binnen
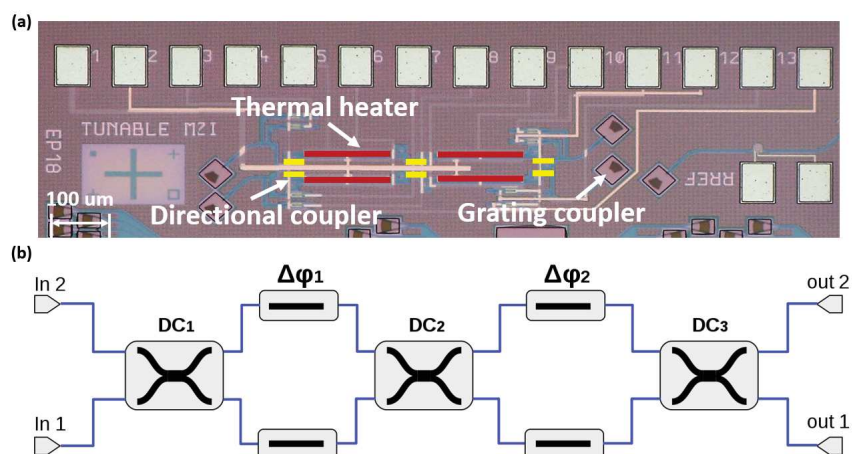
Figuur 4: (a) Microscoopfoto van de gefabriceerde chip. (b) Tweetraps MZI 2 × 2 afstembare koppelaar.

de gele contour een gebied (donkerblauwe) vinden waar de kruistransmissie vrijwel constant wordt, wat wijst op een vlakke spectrale respons en een breedbandige werking. De witte cirkels geven de verdeling van de koppelingsverhouding aan volgens de fasecombinatie van faseverschuiver 1 en faseverschuiver 2 bij een golflengte van 1550 nm. De gele contour overlapt met de verschillende witte cirkels van koppelingsverhouding van 0% tot 100%. Dit betekent dat we de faseverschuivers kunnen afstemmen om breedbandige werking te bekomen voor elke willekeurige koppelingsverhouding.

We hebben we dus een afstembaar koppelingscircuit ontworpen en gedemonstreerd met een koppelingsbereik van 0-100%, zelfs onder invloed van fabricagevariaties, zowel in simulatie als in experimenten. We laten ook zien dat we het circuit kunnen sturen om een vlakke spectrale respons te verkrijgen over een golflengtebereik van 50-nm.
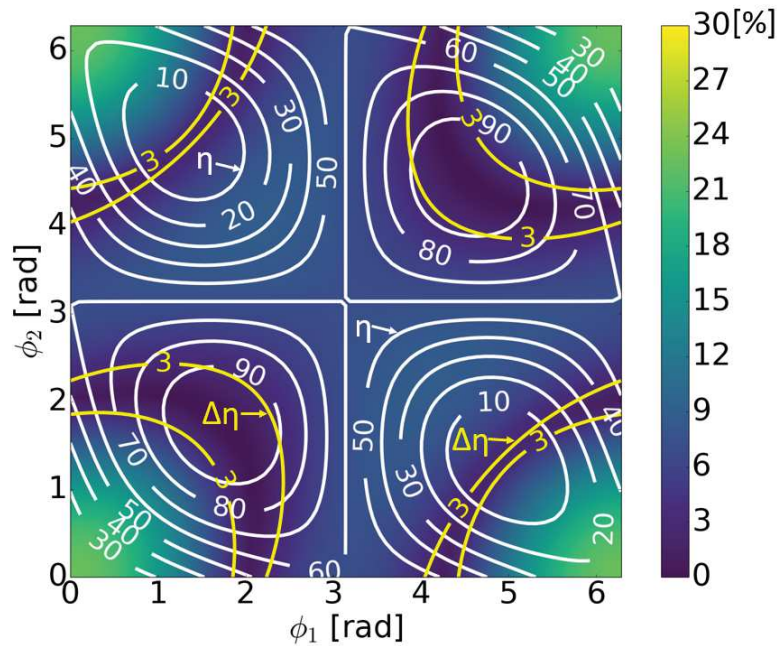
Figuur 5: *Gesimuleerd resultaat van de kruistransmissie η bij een golflengte van 1550 nm en de maximale afwijking van de kruiskoppeling Δη in het golflengetbereik van 1525 tot 1575 nm voor de tweetraps afstembare koppelaar met imperfecte directionele koppelaars met 40:60 koppelingsverhouding. De donkere lijnen in de grafiek geven het gebied aan met een afwijking van 3 % van de gewenste koppeling binnen een golflengtebereik van 50 nm rond 1550 nm. Aangezien dit gebied alle koppelingswaarden van 0-100% bevat, kunnen we de schakeling afstemmen op een 50 nm breedbandkoppelingsregime met een tolerantie van 3%.*

3   MZI-filter met dubbele ring

Filters zoals gekoppelde resonator optische golfgeleiders (CROW) [9], microgolf-notchfilters [10] of ring-geladen MZI's [11] kunnen worden gecreëerd in de universele mesh-circuits. Een enkele ringresonator wordt normaal gesproken definieerd door een meshcel die gevormd door zes afstembare koppelaars, terwijl de meeste in die configuratie niet als koppelaar gebruikt worden. Daardoor is de omtrek van de ring langer dan nodig en worden er ook overdreven veel optische verliezen opgestapeld. De performantie van een ring in een golfgeleider-mesh is daardoor meestal inferieur aan die van een speciaal ontworpen ring resonator, wat het gebruik ervan voor microgolftoepassingen en als optische filters zou beperken. In dit werk stellen we een programmeerbaar filtercircuit voor dat gelijkaardige configureerbaarheid biedt zoals een universeel mesh, maar met minder koppelaars en dus betere performantie.

Wanneer golflengtefilters worden geïmplementeerd als een golfgeleidercircuit, bestaan ze uit een samenstelling van koppelaars, vertragingslijnen, faseverschuivers en ringresonatoren. Deze componenten worden gebruikt om licht te manipuleren om constructieve of destructieve interferentie te bekomen bij bepaalde golflengten, zo wordt bvb. een filterdoorlaatband wordt gegenereerd. We kunnen twee basisklassen van filters identificeren, eindige impulsrespons (Eng: *finite impulse response* of FIR) filter en oneindige impulsrespons (Eng: *infinite impulse response* of IIR) filter. Een FIR-filter bestaat uit voorwaartse vertragingen zoals Mach-Zehnder interferometers of gebundelde golfgeleider-roosters, en deze worden ook wel *moving average* (MA) filters genoemd. Het IIR-filter is samengesteld uit feedbackloops zoals ringresonatoren, en wordt ook wel een autoregressie (AR) filter genoemd.

We presenteren hierbij een filtercircuit dat zowel MZI- als dubbele ringresonatoren bevat, met kenmerken van zowel IIR-filter als FIR-filter. Dergelijke filters, die beide kenmerken combineren, worden daarom autoregressie/moving-average (ARMA) filters genoemd. Een typisch voorbeeld van zo'n ARMA-filter is een ringgeladen MZI, d.w.z. een MZI met een ringresonator in één of beide armen.

Het filtercircuit dat we hier voorstellen, breidt de traditionele ringgeladen MZI uit door een dubbele (gekoppelde) ringresonator te gebruiken die de twee armen van de MZI verbindt. De schematische tekening van de filter wordt getoond in Fig. 16. Dit circuit heeft dezelfde functionaliteit als een ringgeladen MZI met een enkele ring in elke arm, maar de extra koppeling vereenvoudigt de configuratie.

De filter van de tweede orde kan ook in cascade worden geschakeld om filters van een hogere orde te realiseren. Het circuit bevat de tweetraps koppelaar (besproken in de vorige sectie) aan de ingang en uitgang om zo het effect van dispersie verder te reduceren. Een combinatie van lokale en globale optimalisatiestrategieën om de filter te programmeren, met behulp van op maat gemaakte objectieffuncties, is getest in zowel simulatie als experiment. Het uiteindelijke optimalisatieresultaat wordt getoond in Fig. 17 voor drie filterspecificaties. Voor zover wij weten, is dit de eerste keer dat een globale optimalisatiestrategie rechtstreeks wordt gebruikt in ARMA-filtersynthese en -simulatie zonder enige aanvullende vereiste. We breiden
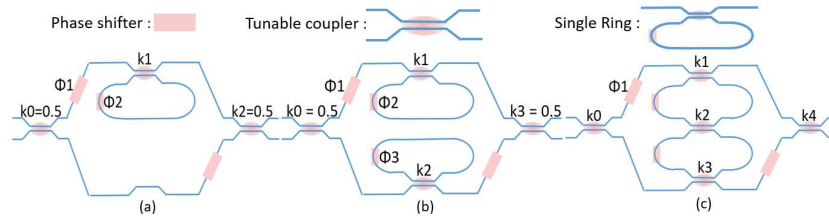
Figuur 6: Schematische tekening van de MZI met een enkele ring wordt getoond in (a), schematische tekening van een MZI met dubbele ring wordt getoond in (b), schematische tekening van gekoppelde ring MZI wordt getoond in (c). Het belangrijkste verschil tussen ons ontwerp gegeven in (c) en de ringgeladen MZI gegeven in (b) is dat de twee ringen zijn verbonden met een afstembare koppelaar, het is duidelijk dat het ontwerp in (c) kan worden geconfigureerd tot een MZI met vertragingslengte van tweemaal de ringomtrek, wat niet mogelijk is met het ontwerp in (b). De faseverschuiver wordt weergegeven als een roze vierkant, de afstembare koppelaar wordt weergegeven als een normale directionele koppelaar met een roze stip in het midden, de enkele add-drop-ring wordt geconstrueerd door de ingangs- en uitgangspoort van de afstembare koppelaar aan dezelfde kant aan te sluiten .

de optimalisatiestrategie verder uit in experimenten en demonstreren het gebruik ervan in een praktische casus voor programmeerbare filtercircuits.

4   Samenvatting

In dit proefschrift hebben we enkele problemen behandeld die te maken hebben met universele programmeerbare fotonische chips. Eerst hebben we een breedbandige optische koppelaar ontworpen. Een dergelijke koppelaar helpt de bandbreedte van het programmeerbare circuit te verbeteren. Vervolgens hebben we een tolerant breedbandig en afstembaar koppelcircuit voorgesteld, dat de belangrijkste bouwsteen is voor de programmeerbare circuits. We hebben we een filterontwerp uitgewerkt op basis van een MZI met een gekoppelde dubbele ring waarvoor de afstand tussen resonanties (Free Spectral Range) groot genoeg is terwijl de verliezen niet te hoog worden. Deze filter zou kunnen gebruikt worden als een pump-rejectrion filter of een optische interleaver.
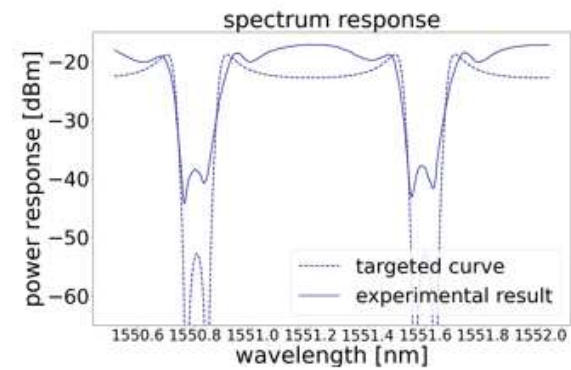
(a): ellip(2,2,17,0.8,'low') ; a = [1, 1.28,0.62] ; b = [0.59, 1.13, 0.59]
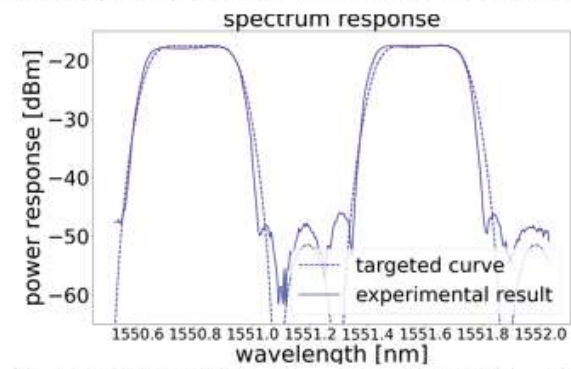
(b): ellip(2,0.03,17,0.21,'low') ; a = [1, -0.212,0.239] ; b = [0.3,0.4,0.3]
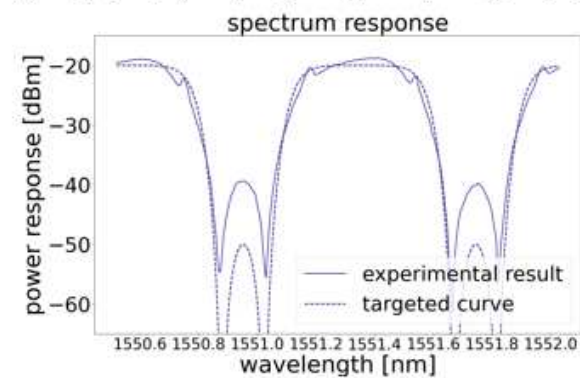
(c): cheby2(2, 15, 0.75, 'low'); a = [1, 0.44,0.25] ; b = [0.46, 0.77, 0.46]

Figuur 7: Experimentele resultaten voor het programmeerbare filterontwerp.

Referenties

[1] Adil Masood, Marianna Pantouvaki, Guy Lepage, Peter Verheyen, Joris Van Campenhout, Philippe Absil, Dries Van Thourhout, and Wim Bogaerts. *Comparison of heater architectures for thermal control of silicon photonic circuits*. In 10th International Conference on Group IV Photonics, pages 83–84, 2013.

[2] Folkert Horst, William M.J. Green, Solomon Assefa, Steven M. Shank, Yurii A. Vlasov, and Bert Jan Offrein. *Cascaded Mach-Zehnder wavelength filters in silicon photonics for low loss and flat pass-band WDM (de-)multiplexing*. Opt. Express, 21(10):11652–11658, May 2013.

[3] Qing Fang, Jun Feng Song, Tsung-Yang Liow, Hong Cai, Ming Bin Yu, Guo Qiang Lo, and Dim-Lee Kwong. *Ultralow Power Silicon Photonics Thermo-Optic Switch With Suspended Phase Arms*. IEEE Photonics Technology Letters, 23(8):525–527, 2011.

[4] Zeqin Lu, Han Yun, Yun Wang, Zhitian Chen, Fan Zhang, Nicolas A. F. Jaeger, and Lukas Chrostowski. *Broadband silicon photonic directional coupler using asymmetric-waveguide based phase control*. Opt. Express, 23(3):3795–3808, Feb 2015.

[5] Samee ur Rehman, Matthijs Langelaar, and Fred van Keulen. *Efficient Kriging-based robust optimization of unconstrained problems*. Journal of Computational Science, 5(6):872–881, 2014.

[6] Ivo Couckuyt, Tom Dhaene, and Piet Demeester. *ooDACE toolbox, a Matlab Kriging toolbox: Getting started*. 2013. User manual for program ooDACE toolbox.

[7] Wim Bogaerts, Daniel Pérez, José Capmany, David A. B. Miller, Joyce Poon, Dirk Englund, Francesco Morichetti, and Andrea Melloni. *Programmable photonic circuits*. Nature, 586(4):1476–4687, 2020.

[8] David A. B. Miller. *Perfect optics with imperfect components*. Optica, 2(8):747–750, Aug 2015.

[9] Joyce KS Poon, Jacob Scheuer, Yong Xu, and Amnon Yariv. *Designing coupled-resonator optical waveguide delay lines*. JOSA B, 21(9):1665–1673, 2004.

[10] David Marpaung, Blair Morrison, Ravi Pant, Chris Roeloffzen, Arne Leinse, Marcel Hoekman, Rene Heideman, and Benjamin J. Eggleton. *Si3N4 ring resonator-based microwave photonic notch filter with an ultrahigh peak rejection*. Opt. Express, 21(20):23286–23294, Oct 2013.

[11] Christi K Madsen and Jian H Zhao. *Optical filter design and analysis*. 1999.

English summary

Integrated photonics technology makes it possible to build large and complex photonic systems-on-chip. These circuits which process optical signals in waveguides on the surface of a chip, are usually designed for a specific function. However, mesh circuits consisting of interconnected waveguides, tunable beam couplers and optical phase shifters [1] enable universal programmable chips [2] which can be reconfigured for multiple functions. Such generic chips can be programmed to test prototypes and thus help speed up the development process for new products powered by photonics. The developments of these general purpose programmable chips lay in following categories: the basic building blocks - tunable couplers and optical phase shifters, control and optimization algorithms, packaging and applications.

1. Tunable couplers. Tunable coupler is often a tunable optical 2×2 coupler, that can change its coupling ratio from 0% to 100%.

2. Optical phase shifters. Optical phase shifter is used to control the phase of light by a change in the effective refractive index.

3. Control and optimization algorithms. Since thermal cross-talk, electrical cross-talk, dispersion induced by couplers , fabrication variation of optical components will degrade our filter performance, thus the optimisation algorithm is needed in real time measurements.

4. Packaging. The packaging of the chip includes Fibre-to-Grating Coupling, Electrical Connections, Thermal Management and etc.

5. Applications. Applications for programmable photonic circuits including: Microwave signals can be transported over fiber and processed in the optical domain for xDSL and 5G applications. Optical sensor systems can be used in construction, automotive, security and medical environments, such as for optical coherence tomography (OCT), or frequency-modulated continuous wave (FMCW) LiDAR.

The directional coupler is an essential building block of the photonic circuit. It is used for splitting and combining light. A compact, wavelength independent directional coupler [3] is highly desired, especially for telecom applications such as wavelength-division-multiplexing [4] and signal switching [5]. In this thesis, we proposed a broadband coupler design. To make them programmable, we need

to be able to change the coupling ratios, however the broadband nature is obtained. A two-stage Mach–Zehnder interferometer (MZI) has been proposed as a tolerant broadband tunable coupler circuit [6] in this thesis.

One key function of the universal programmable chips is a programmable filter. It is possible to program wavelength filters in a universal programmable waveguide mesh, using the tunable couplers to distribute the light over multiple paths (including resonant rings) and then interfere these to achieve a wavelength dependent response. However, the available path lengths in these waveguide meshes can be quite long, introducing substantial optical losses and limiting the 'free spectral range' (FSR) of the filter. We propose a dedicated programmable filter component. We also developed the corresponding filter synthesis and optimization algorithm for this circuit. Such a programmable filter could find its applications in photonic systems as an optical interleaver or pump rejection filter.

5   Passive broadband coupler

In wavelength circuits, there are many points where the light needs to be split, often with well controlled fractions that are constant over a wide wavelength range. The most common case is a 50:50 couplers, where the imbalance is the most critical parameter.

The normal directional coupler is dispersive. Although MMI is also widely used as broadband splitter and combiner, however it has some extra loss and also backrefection sometimes. The MMI is based on multi-mode interference, and this only works well for a few specific values of power coupling.

A broadband coupler could be realized by many approaches. Among these works [7] [8] [9] [10], the 2×2 asymmetric-waveguide-assisted directional coupler [7] is demonstrated to be broadband (operating over a wide wavelength range), compact in size, simple in structure, and easy to fabricate.

The layout of such a component is given in Fig. 1.9. The layout is a MZI-shaped design, it is composed of 4 sub-sections: a symmetrical coupler, 2 s-bends, a taper section and a phase compensation section. This layout is chosen instead of using the layout given in paper [7] since we have found that the coupling in the phase compensation section and the taper section could not be ignored. Thus, we not only separate the distance in the phase compensation section, but also we have chosen a more rigorous simulation method compared to transfer matrix method (TMM) in paper [7] - (eigenmode expansion) EME for the component simulation since previous study with TMM method did not take the coupling in the taper section and phase compensation section into account. This method although is time-consuming compared to TMM, it is still acceptable since the sweeping of the length is fast due to the nature of EME.

We built the broadband coupler model with EME in FIMMPROP, which is a commercial optical mode solver replying on the rigorous EME method. The initial design is set as symmetric in which the length of the input and the length of output coupler are the same. Then two parameters are set as variables in the next
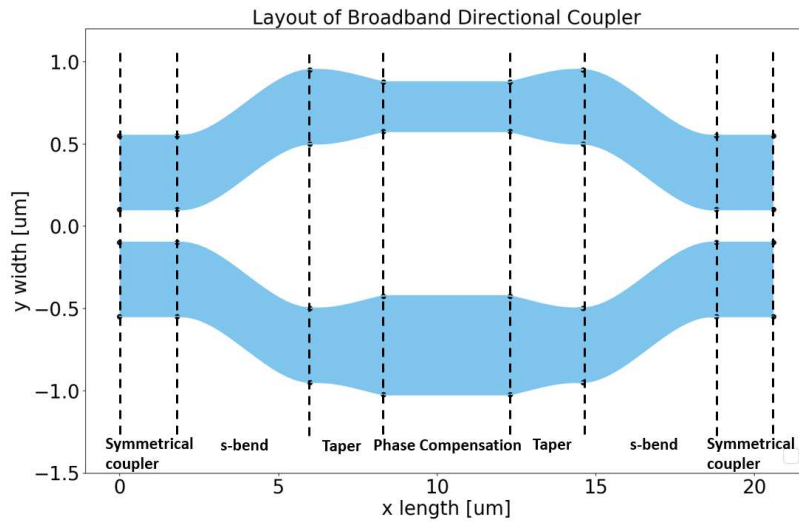
Figure 8: Layout of a broadband directional coupler implemented by a MZI

optimization step. In this thesis, the optimization algorithm [11] of the ooDACE [12] toolbox developed by the SUMO group of IDlab at Ghent University-imec is used to optimize the broadband performance of such design.
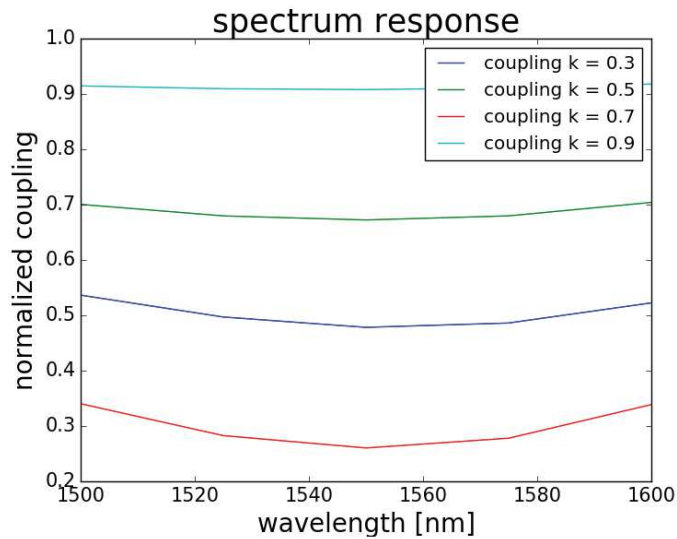
Figure 9: Spectrum response of a few selected optimized design is plotted. Five wavelengths 1500, 1525, 1550, 1575 and 1600 nm are used in the optimization process.

By using the optimization method Kriging, the spectral response of a few optimized designs are selected and shown in Fig. 9. The detailed design information for the optimized designs are given in Table 2:

target coupling value	simulation result	deviation	design parameters
$k = 0.3$	$k = 0.302$	$\delta = 0.04$	$L_1 = 12.5787um$
			$L_2 = 8.470um$
$k = 0.5$	$k = 0.508$	$\delta = 0.0363$	$L_1 = 9.905um$
			$L_2 = 8.646um$
$k = 0.7$	$k = 0.724$	$\delta = 0.0162$	$L_1 = 7.234um$
			$L_2 = 8.793um$
$k = 0.9$	$k = 0.9$	$\delta = 0.0173$	$L_1 = 3.079um$
			$L_2 = 8.958um$

Table 2: Design parameters of a few optimized designs in Fig. 9 are given, we optimized 4 coupler designs within 100 nm wavelength range of the central wavelength 1550 nm. The simulation result is the average coupling value calculated by averaging the couplings of 5 different wavelengths. The deviation describes how dispersive a coupler is, it is calculated by the maximum difference between the simulated couplings of 5 different wavelengths and the target coupling value. L_1 is the length of the input and output coupler and L_2 is the length for the phase compensation section.

The dispersion is larger in the broadband designs with small coupling values. As we can see from Table 3.1, the length of the input and output coupler changes quite a lot for different designs, however the length of the phase compensation section kept similar.

The design could be further optimized by increasing the number of optimization parameters such as the height of the s-bend and the widths of the phase compensation section.

6   Tolerant, Broadband Tunable 2×2 Coupler Circuit

In a programmable waveguide circuit, the flow is controlled by the couplers between the waveguides. To make this reconfigurable, tunable couplers are needed where the coupling strength can be changed during operation, besides, it is desired to have the broadband behaviour. Also, the relative phase shift between the waveguides needs to be controlled. We propose a tolerant broadband tunable coupler circuit in this section.

The basic building block of a programmable circuit is a tunable coupler shown in Fig. 10, at least two adjustable parameters p_1 and p_2 are needed to independently control the power splitting κ and the phase shift $\Delta\phi$. A common way of implementing a tunable 2×2 coupler is a balanced Mach-Zehnder interferometer (MZI) with a phase shifter in each arm.
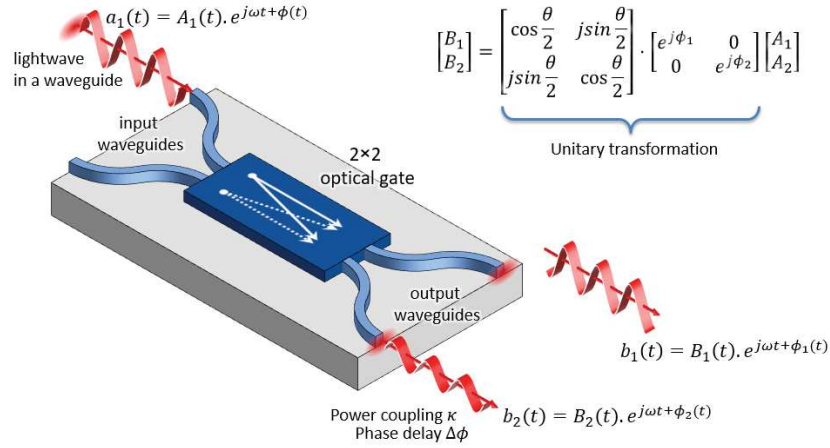
Figure 10: A 2×2 optical gate mixes the waves from two input waveguides, controlling both the power coupling and the phase delay [2]. A common way of implementing a tunable 2×2 coupler is a balanced Mach-Zehnder interferometer (MZI) with phase shifter in each arm.

The MZI is constructed from two static 50:50 couplers such as the broadband DCs from the previous section, connected with two delay lines with integrated phase shifters (e.g. heaters). The coupling response of the MZI can be swept from minimum to maximum by tuning the phase delay from 0 to π. However, to obtain the full 0-100% coupling range, the two static couplers need to have a perfect 50:50 splitting balance, which is not easy to design over a wide wavelength range [13].

In this work, we proposed the design of a two-stage MZI, as shown in Fig. 11.

We demonstrate that the circuit is tolerant to fabrication variation and wavelength-independent. Let's assume that the circuit consists of imperfect DCs of 40:60 coupling ratio at 1550 nm, which is a significant deviation from the designed value of 50:50. In Fig. 12, we plot the simulated power coupling η at 1550 nm (white contours), and overlay it with the maximum deviation $\Delta\eta$ within the wavelength range of 1525-1575 nm. For any given desired coupling value, we can tune the two phase shifters such that we obtain an almost uniform spectral response over the entire wavelength range. The coupling deviation over the entire wavelength range compared to the targeted coupling value is within 3%.we can find inside the yellow contour (the dark blue region) where the cross transmission becomes almost non-dispersive indicates a flat spectral response and broadband operation. The white circles indicates the coupling ratio distribution according to the phase combination of phase shifter 1 and phase shifter 2 at 1550 nm. The yellow contour overlaps with different white circles of coupling ratio from 0% to 100%. It means that we could tune the phase shifters to find broadband operation for any arbitrary coupling ratio.

We had this circuit fabricated on IMEC's standard ISiPP50G silicon photonics

platform. In total 3 different designs for the two-stage MZI tunable coupler have been fabricated, with different nominal design values for the directional couplers. Device A has a DC designed with 60:40 split ratio at wavelength 1550 nm, device B with a 65:35 DC, and device C with a 70:30 DC.

The experimental result is compared with simulation. Fig. 14(a-b) show the simulation results of the coupling at 1550 nm and the variation over a 50-nm range (both in dB scale). The dark blue region in Fig. 14(b) surrounded by the yellow lines have <1 dB variation, (For a 3 dB coupler, the 1 dB variation region would span from -2 dB to -4 dB. For a -20 dB coupling ratio, the 1 dB region spans from -19 dB to -21 dB.) Fig. 14(c-d) is the corresponding experimental result, and we can see a good qualitative agreement. The black rectangles in Fig. 14(c-d) correspond to the phase space plotted in Fig. 14(a-b).

We can now use the obtained 2-D transmission maps as a look-up table (LUT) for configuring the tunable coupler to search for a desired coupling ratio. This gives us the transmission curves plotted in Fig. 15. We see that the variation for larger coupling ratios are significantly larger than that of smaller coupling ratios.

In conclusion, We designed and demonstrated a simplified tunable coupler circuit with 0-100% coupling range even under conditions of fabrication variations both in simulation and experiments. We also show that we can bias the circuit to obtain a flat spectral response over a wavelength range of 50 nm.
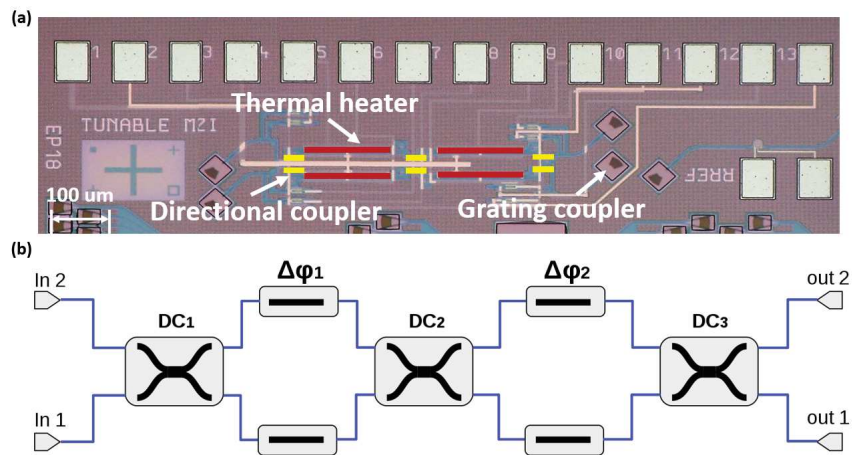
Figure 11: (a) Microscope picture of the fabricated device.(b) Two-Stage MZI 2×2 tunable coupler.

7 Double ring loaded MZI filter

Tunable couplers are an essential part for building programmable wavelength filters. Wavelength filters on photonic circuits are used to filter out one or more wavelength bands from a spectrum, for instance to separate telecommunication channels [4], perform spectroscopic measurements [14], or perform filtering operations on optically encoded microwave signals [15].

Wavelength filters are made by splitting up light into multiple paths with different delays, and recombining them again to create wavelength-dependent interference [16]. There are different implementations, such as coupled-resonator optical waveguides (CROW) [17], ring resonator notch filters [18] or ring-loaded MZIs [19].

When implemented as a waveguide circuit, optical filters are composed of couplers, delay lines, phase shifters, or ring resonators. These components are used to manipulate light to have constructive or destructive interference at certain wavelengths, such that a filter passband is generated.
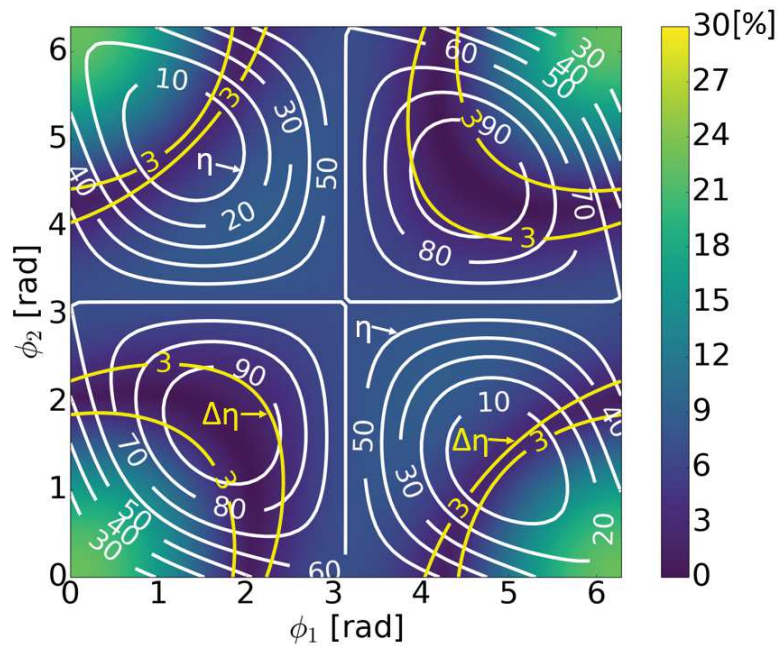
Figure 12: Simulated result of cross transmission η at 1550 nm and the maximum deviation of the cross coupling $\Delta\eta$ from 1525 to 1575 nm for the two-stage tunable coupler with imperfect DCs of 40:60 coupling ratio. The dark lines in the graph indicate the region of 3% deviation from the desired coupling within a 50 nm wavelength range of 1550 nm. As this region contains all coupling values from 0-100%, we can tune the circuit to a 50 nm broadband coupling regime with a tolerance of 3%.
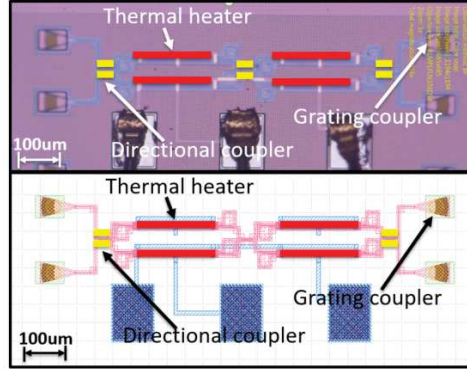
Figure 13: Fabricated chip on the IMEC ISiPP50G platform. (a) microscopic image of the fabricated chip and (b) the corresponding GDS layout of the design.

A single ring resonator is normally generated by a mesh cell composing six tunable couplers, and thus the round-trip length and loss for a single ring in a mesh is larger compared to a simple custom-designed ring resonator, the higher loss would result in a larger linewidth of the ring resonance, and the longer roundtrip length would reduce the free spectral range. This could limit the functionality of these general-purpose meshes for microwave photonic applications. In this work, we propose a dedicated programmable filter circuit that offers similar levels of programmability but with shorter path lengths, lower losses and a smaller number of tuning elements.

We can identify two basic classes of filters, i.e. finite impulse response (FIR) filter and infinite impulse response (IIR) filter. An FIR filter is usually composed by forward delays such as MZIs or arrayed waveguide gratings, and these are also called moving average (MA) filters. The IIR filter is composed by feedback loops such as ring resonators, and are also called autoregression (AR) filters [19].

We hereby present a filter circuit which incorporates both MZI and double ring resonators, which has features from both IIR filter and FIR filter. Such filters, which combine both characteristics, are therefore called auto-regression/moving average (ARMA) filters. A typical example of such ARMA filter is a ring-loaded MZI, i.e. an MZI with a ring resonator in one or both arms. The schematic of ring-loaded MZI is given in Fig. 16(a) and (b).

The filter circuit we propose here extends the traditional ring loaded MZI by using a double (coupled) ring resonator that links the two arms of the MZI. The schematic drawing of the filter is shown in Fig. 16. This circuit has similar functionality as a ring loaded MZI with a single ring in each arm, but the additional coupling facilitates the configuration.

The second-order filter can also be cascaded to realize higher-order filters. A single stage of this programmable filter has N degrees of freedom for its configuration. We need to tune the N independent phase shifters to obtain the filter response
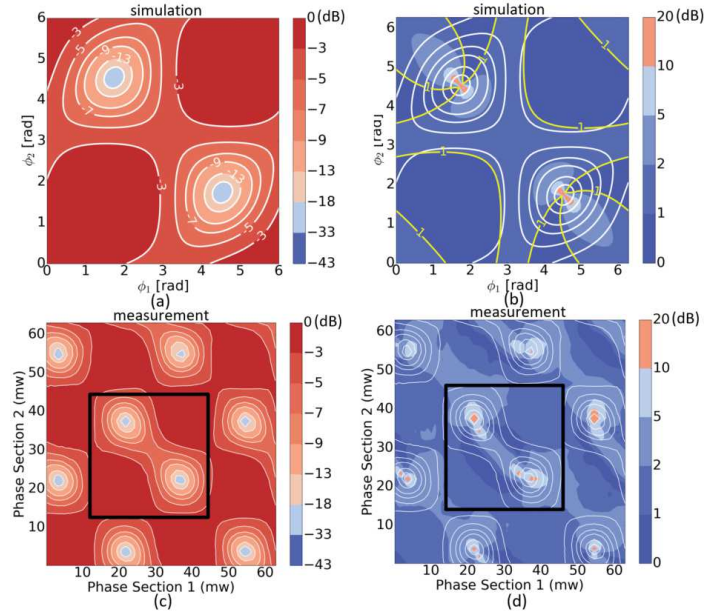
Figure 14: Comparison between simulation and experiment for device A (50:50). (a) Simulation result of the coupling at a wavelength of 1550 nm on a logarithmic (dB) scale. (b) Variation plot on a logarithmic (dB) scale.(c,d) Corresponding experimental results for (a,b).
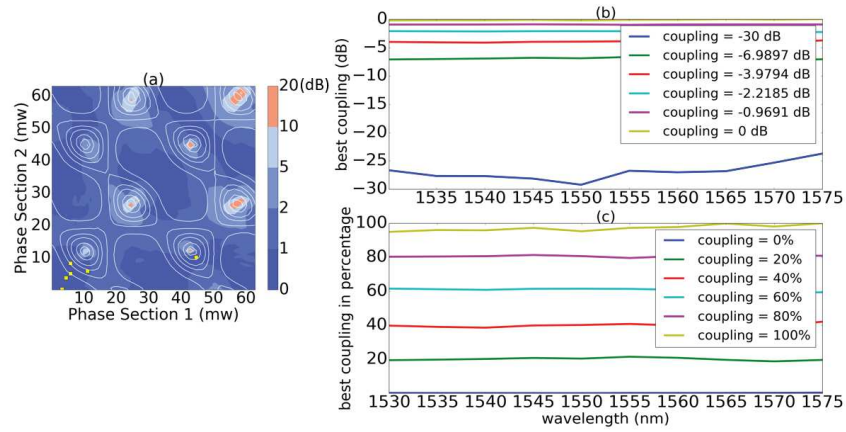
Figure 15: Similar to Fig. 14(d), the experimental result for the cross port of device B (65:35) is shown in Fig. 15a, the yellow dots corresponds to coupling values in (b) Coupling values of 0-100% in steps of 20% are plotted using the LUT of Fig. 15(a) in linear scale in Fig. 15(b) and in logarithmic scale in Fig. 15(c).

.
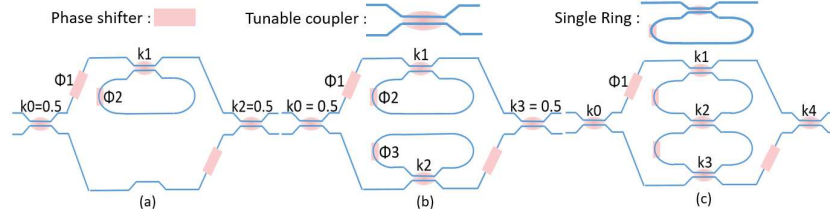
Figure 16: Schematic drawing of the single ring loaded MZI is shown in (a), schematic drawing of double ring loaded MZI is shown in (b), schematic drawing of coupled ring loaded MZI is shown in (c). The main difference between our design given in (c) and the ring loaded MZI given in (b) is that the two rings are connected with a tunable coupler, it is obvious that the design in (c) could be configured to a MZI with delay length of twice the ring circumference, which is not straightforward with the design in (b). The phase shifter is shown as a pink box, the tunable coupler is shown as a normal directional coupler with a pink dot in the middle, the single add drop ring is constructed by connecting the input and output port of the tunable coupler on the same side.

that we desire. Thus, a sequential configuration scheme or an optimization step is required to configure the second-order filter design.

The circuit incorporates a two-stage input and output coupler as discussed in the previous section to further reduce the effect of dispersion. A combination of local and global optimization strategies to program the filter, using tailored objective functions, have been tested in simulation and experiments. The final optimization result is shown in Fig. 17 for three filter specifications. Fig. 5.16 shows that the measured transmission matches well with the targeted simulation curve, the extinction ratio of 20 dB is achieved by all the filter types, some even have an extinction ratio of 30 dB.

The experimental result is obtained first by assigning the phase shifters with the calculated phase values (see the supplementary material for the programmable filter design), however the crosstalk of different electronic channels of the digital-to-analog convector and thermal crosstalk of the phase shifters degrades the spectrum responses severely compared to the original prediction. Therefore the optimization algorithm is needed to finetune the device. To our best knowledge, this is the first time a global optimization strategy is directly used in optical ARMA filter synthesis and simulation without any monitor photon diode inside the circuit. We further extend the optimization strategy into experiments and demonstrated its use in practical case for programmable filter circuits.

8 Summary

In this thesis, we address some key problems related to programmable chips. First, we designed a broadband coupler component. Such coupler helps to improve the

bandwidth of the programmable circuit. Then, we proposed a tolerant broadband and tunable coupler circuit, which is the main building block for the programmable circuits. In order to address the large FSR and higher insertion loss related to the general-purpose programmable chip, a double ring loaded MZI design has been proposed as a programmable filter. This filter design could be used as a pump-rejection filter or an optical interleaver.

(a): ellip(2,2,17,0.8,'low') ; a = [1, 1.28,0.62] ; b = [0.59, 1.13, 0.59]

(b): ellip(2,0.03,17,0.21,'low') ; a = [1, -0.212,0.239] ; b = [0.3,0.4,0.3]

(c): cheby2(2, 15, 0.75, 'low'); a = [1, 0.44,0.25] ; b = [0.46, 0.77, 0.46]
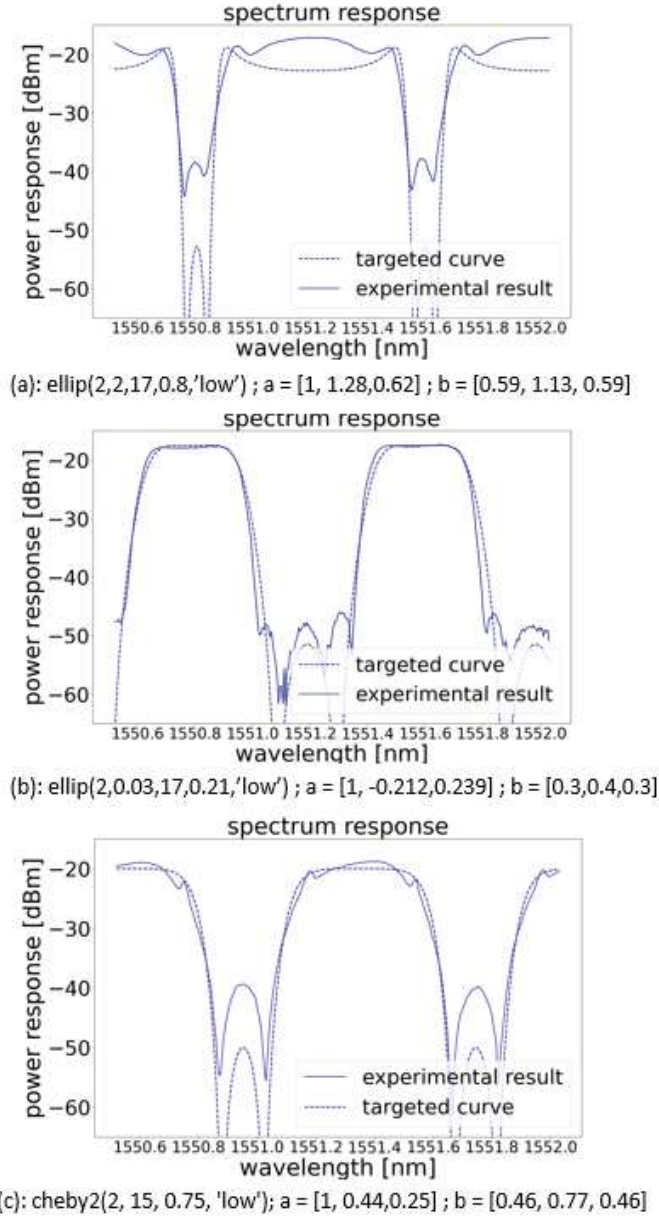
Figure 17: Experimental transmission spectra of the double ring-loaded MZI filter. Each plot shows the target design (with the a_i and b_i coefficients listed below the plot). The experimental results are obtained by optimizing the spectral response from the chip outputs by driving the on-chip actuators in real time. From the measurement we can see, the experimental results matches the simulation very well, and the overall extinction ratio exceeds 20 dB for all designs.

References

[1] Adil Masood, Marianna Pantouvaki, Guy Lepage, Peter Verheyen, Joris Van Campenhout, Philippe Absil, Dries Van Thourhout, and Wim Bogaerts. *Comparison of heater architectures for thermal control of silicon photonic circuits*. In 10th International Conference on Group IV Photonics, pages 83–84, 2013.

[2] Wim Bogaerts, Daniel Pérez, José Capmany, David A. B. Miller, Joyce Poon, Dirk Englund, Francesco Morichetti, and Andrea Melloni. *Programmable photonic circuits*. Nature, 586(4):1476–4687, 2020.

[3] Zeqin Lu, Han Yun, Yun Wang, Zhitian Chen, Fan Zhang, Nicolas Jaeger, and Lukas Chrostowski. *Broadband silicon photonic directional coupler using asymmetric-waveguide based phase control*. Optics Express, 23:3795–3808, 02 2015.

[4] Folkert Horst, William M.J. Green, Solomon Assefa, Steven M. Shank, Yurii A. Vlasov, and Bert Jan Offrein. *Cascaded Mach-Zehnder wavelength filters in silicon photonics for low loss and flat pass-band WDM (de-)multiplexing*. Opt. Express, 21(10):11652–11658, May 2013.

[5] Qing Fang, Jun Feng Song, Tsung-Yang Liow, Hong Cai, Ming Bin Yu, Guo Qiang Lo, and Dim-Lee Kwong. *Ultralow Power Silicon Photonics Thermo-Optic Switch With Suspended Phase Arms*. IEEE Photonics Technology Letters, 23(8):525–527, 2011.

[6] Mi Wang, Antonio Ribero, Yufei Xing, and Wim Bogaerts. *Tolerant, broadband tunable 2× 2 coupler circuit*. Optics express, 28(4):5555–5566, 2020.

[7] Zeqin Lu, Han Yun, Yun Wang, Zhitian Chen, Fan Zhang, Nicolas A. F. Jaeger, and Lukas Chrostowski. *Broadband silicon photonic directional coupler using asymmetric-waveguide based phase control*. Opt. Express, 23(3):3795–3808, Feb 2015.

[8] Kimmo Solehmainen, Markku Kapulainen, Mikko Harjanne, and Timo Aalto. *Adiabatic and multimode interference couplers on silicon-on-insulator*. IEEE Photonics Technology Letters, 18(21):2287–2289, 2006.

[9] R. Halir, A. Maese-Novo, A. Ortega-Mo nux, I. Molina-Fernández, J. G. Wangüemert-Pérez, P. Cheben, D.-X. Xu, J. H. Schmid, and S. Janz. *Colorless directional coupler with dispersion engineered sub-wavelength structure*. Opt. Express, 20(12):13470–13477, Jun 2012.

[10] MZ Alam, J Niklas Caspers, J Stewart Aitchison, and Mo Mojahedi. *Compact low loss and broadband hybrid plasmonic directional coupler*. Optics express, 21(13):16029–16034, 2013.

[11] Samee ur Rehman, Matthijs Langelaar, and Fred van Keulen. *Efficient Kriging-based robust optimization of unconstrained problems*. Journal of Computational Science, 5(6):872–881, 2014.

[12] Ivo Couckuyt, Tom Dhaene, and Piet Demeester. *ooDACE toolbox, a Matlab Kriging toolbox: Getting started*. 2013. User manual for program ooDACE toolbox.

[13] David A. B. Miller. *Perfect optics with imperfect components*. Optica, 2(8):747–750, Aug 2015.

[14] B. Imran Akca and Christopher R. Doerr. *Interleaved Silicon Nitride AWG Spectrometers*. IEEE Photonics Technology Letters, 31(1):90–93, 2019.

[15] Eric A. Kittlaus, Prashanta Kharel, Nils T. Otterstrom, Zheng Wang, and Peter T. Rakich. *RF-Photonic Filters via On-Chip Photonic–Phononic Emit–Receive Operations*. Journal of Lightwave Technology, 36(13):2803–2809, 2018.

[16] Lei Zhang, Haiyang Zhao, Haoyan Wang, Sizhu Shao, Wenjing Tian, Jainfeng Ding, Xin Fu, and Lin Yang. *Cascading Second-Order Microring Resonators for a Box-Like Filter Response*. J. Lightwave Technol., 35(24):5347–5360, Dec 2017.

[17] Joyce KS Poon, Jacob Scheuer, Yong Xu, and Amnon Yariv. *Designing coupled-resonator optical waveguide delay lines*. JOSA B, 21(9):1665–1673, 2004.

[18] David Marpaung, Blair Morrison, Ravi Pant, Chris Roeloffzen, Arne Leinse, Marcel Hoekman, Rene Heideman, and Benjamin J. Eggleton. *Si3N4 ring resonator-based microwave photonic notch filter with an ultrahigh peak rejection*. Opt. Express, 21(20):23286–23294, Oct 2013.

[19] Christi K Madsen and Jian H Zhao. *Optical filter design and analysis*. 1999.

1

Introduction

Photonics [1] is the physical science and application of light generation, detection, and manipulation through emission, transmission, modulation, signal processing, switching, amplification, and sensing. It is vital to high speed communication system where light is used as a carrier. One reason that optical communication is attractive is that it is cheaper and faster than its electronics counterpart. Photonics is advantageous in power consumption compared to electronics, which made it a perfect candidate for optical interconnects in data centers [2] [3].

1.1 Silicon Photonics

Silicon photonics (SiPh) is a material platform from which photonic integrated circuits (PICs) can be made. The material silicon is used as the main fabrication element. A PIC usually contains multiple components arranged in a circuit to implement a broadband range of functions, such as wavelength filtering, modulation, sensing, etc.

SiPh is compatible with CMOS (electronic) fabrication, which allows SiPh PICs to be manufactured using established CMOS foundry infrastructure. The CMOS process also allows the co-integration with electronics and low-cost-at-high-volume fabrication of integrated optical device due to the nature of the technology [4]. Students or researchers can now access active silicon photonics fabrication, e.g., via the multi-project wafer services offered by Europractice, AIM photonics, and others.

There are a large number of applications based on silicon photonic systems that are emerging in recent years, including LIDAR systems, bio-sensing, nonlinear optics, microwave photonics and coherent communication. Areas of biosensing [5], LIDAR [6], transceivers [7] are now commercializing themselves, lots of startups companies are involved in these areas.

1.1.1 Introduction to few basic building blocks

1.1.1.1 Waveguide

The fundamental building block in a PIC is the waveguide. The transmission of light is guided through the it. It also connects all the other components on chip, such as splitters, combiners, modulators and lasers. A typical waveguide in silicon photonics consists of a silicon core surrounded by another (dielectric) materials with lower refractive index, usually air or silicon oxide (SiO2). This structure allows light to be confined in the core through total internal reflection. Normally the waveguide is designed to be single model and polarization independent.

The typical demensions of a waveguide in silicon photonics is given in Fig. 1.1, the tight structures allows the miniaturization of the photonic components and the integration of a large number of components in a reduced space compared to PLC, thus made the possible for large scale programmable photonics.
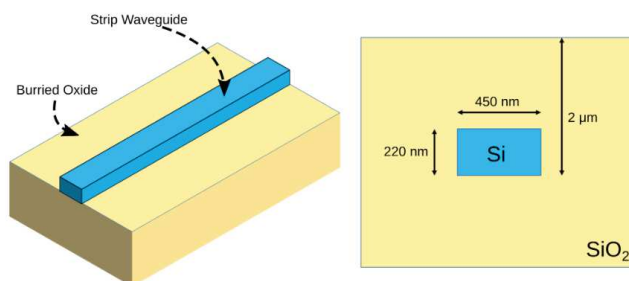
Figure 1.1: (a) Air cladding SOI waveguide. (b) Typical geometry and dimensions for a single mode silicon-on-insulator strip waveguide with silicon oxide cladding

1.1.1.2 Coupler

In wavelength circuits, there are many points where the light needs to be split, often with well controlled fractions that are constant over a wide wavelength range. The directional coupler is the most common way to implement a waveguide coupler. The schematic of a directional coupler is given in Fig. 1.2.The operation principle of the conventional directional coupler is illustrated as follows: light is

launched into one arm and excites the even and odd supermodes of the two parallel waveguides. The beat length of these two modes is given in Eq. 1.1.

$$L_\pi = \frac{\lambda}{2(n_{even} - n_{odd})} \tag{1.1}$$

The normal directional coupler is very dispersive in high-contrast systems, also it is quite sensitive to fabrication variations due to the narrow coupling gap.Thus, a broadband directional coupler design is highly desired in most applications.

A power coupling ratio,κ, is associated with each directional coupler. The coupling ratio is determined by the length of region where the two waveguides are coupled.
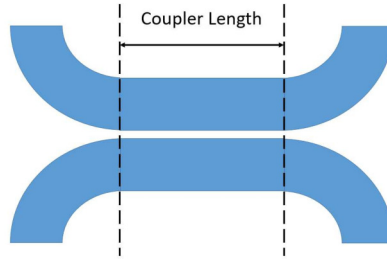
Figure 1.2: The directional coupler is composed of two coupled waveguides. The waveguide is given as blue region. The power coupling ratio, κ is determined by the length of region where the two waveguides are coupled.

1.1.1.3   Ring resonator

In general a ring resonator consists of a looped optical waveguide and a coupling mechanism to access the loop. A typical all-pass ring resonator constructed by feeding one output of a directional coupler back into its input is shown in Fig. 2.9. When the waves in the loop build up a round trip phase shift that equals an integer times 2π, the waves interfere constructively and the cavity is in resonance.

The spectral response of the ring resonator is given as in Fig. 1.4. The free spectral range (FSR) of the ring resonator is defined by the the wavelength range between two resonances.

1.1.2   Passive devices

The Y branch, multi-mode interferometer (MMI), Directional coupler (DC), grating coupler, Arrayed waveguide grating (AWG) are common passive devices. The Y branch , MMI and DC are commonly used as 50/50 splitters [8]. The MMI has certain back-reflections. We hereby introduce few basic passive components.
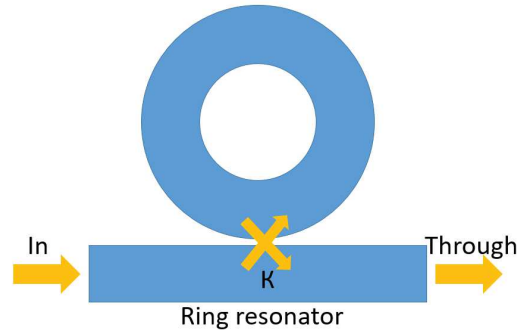
Figure 1.3: All pass ring
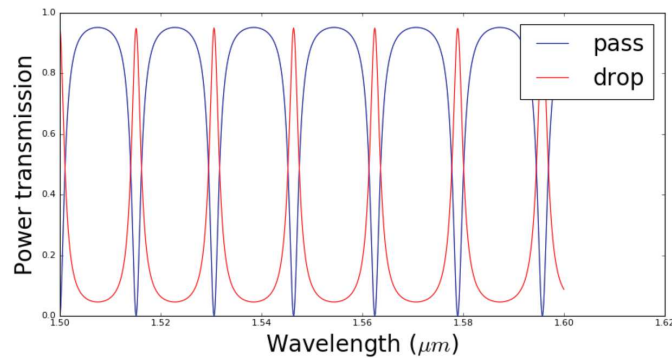
Figure 1.4: Spectral response of the ring resonator

1.1.3 Active devices

Detectors, modulators and lasers are common active devices. Optical modulation and tuning are based on carrier depletion in a PN-junction and carrier injection in a PIN junction [9].

Optical modulators imprint an electrical signal on an optical wave, termed the optical carrier. Amplitude, phase, frequency, and polarization of the optical carrier and any combination of the above can be exploited for encoding the information [10].

The photo-detector converts the optical signal to an electrical signal. Since silicon is not a good light absorber for standard telecommunication wavelength, thus, epitaxial germanium growth [11], III-V bonding [12], plasmonic absorption [13] are used to develop the photodetector.

Silicon is an indirect-band semiconductor, thus it is not possible to generate light with pure silicon. Integration of lasers and optical amplifiers on the silicon platform are made use of the following approaches: co-packaging, bonding (hy-

brid lasers), germanium lasers and monolithic growth.

All devices suffer from fabrication variations, which leads to the deviation of the desired transmission from actual transmission. This effect degrades the performance of the circuit [14], especially for large photonic circuits.

Waveguides are dispersive, many devices are also wavelength dependent because of the high refractive index contrast and the small dimensions. Thus a broadband component such as broadband coupler is higher desired.

There is one passive component in which we are particularly intereted in, because it is essential for large-scale programmable photonic circuits: A broadband 2×2 coupler. We want both a passive device that delivers a fixed power coupling ratio over a whole wavelength range, and an active circuit that can be tuned to deliver a specific coupling ratio over a similarly wide wavelength range. The broadband nature of the component would enable multiple applications such as optical interleaver and switches. It would also benefit or improve the performance of the programmable photonic circuit. We will briefly introduce the development of such component.

1.1.4 Technical challenge

Silicon Photonics has been rapidly developing in the past decade, and many development of Si-based photonic technologies for communication have demonstrate its potential to be used for commercial products. Besides the rapid progress, there are always technical challenges.

1.1.4.1 Propagation loss and radiation loss in bending

The propagation loss is mainly determined by the line-width roughness. The typical loss of the waveguide is in the order of $0.2\ dB/cm$ to $1.0\ dB/cm$. The formula to calculate the scattering loss as given in Eq. 1.2, is shown below:

$$\alpha = \frac{\delta^2 \cdot \kappa}{k_0 \cdot d^4 \cdot n_1} \tag{1.2}$$

where δ is root-mean square roughness and the correlation length of the surface roughness structure is denoted as l_c, k_0, d, and n_1 are wavevector of the light in vacuum, the half-width of the core, and effective index. The κ depends on the wave-guide geometry and statistical distribution of the roughness, in which l_c is included.

The radiation loss is mainly caused by the bending section. The Euler bend [15] is demonstrated to be able to reduce the loss of the bend significantly, thus the radius of the bends could be reduced accordingly, which facilities more compact design and layout size reduction for large photonic circuit designs. There are also other methods to improve the propagation loss.3 µm thick SOI platform have

been used to realize long and low-loss wave-guide spirals [16]. The multi-mode waveguide is said to reduce the waveguide loss in the coupler and in the ring cavity, and therefore achieve high Q factors compared to previous implementations of resonators in SOI without sacrificing the free-spectral range [17].

1.1.4.2 Coupling to external fiber

There are two kinds of couplers normally used in silicon photonics, edge coupler and grating coupler. Both of these couplers utilize a taper structure. The mode in the silicon photonic waveguide is diffracted from the taper and captured by a silica-based waveguide in the edge coupler case. For grating coupler, the light leaking from the taper is captured by the grating and coupled to the fiber. The length of the taper in the normal straight grating coupler is too long, few hundred μm length are needed, thus a curved grating coupler has been proposed to reduced the length of the taper [18]. In order to improve the coupling efficiency, few methods have been proposed, such as optical proximity correction (OPC) for the curved grating fabrication [19], or reflection coatings to reducing the light leaking to the substrate [20] . The difference of the edge coupler and grating coupler also lie in the coupling efficiency they can achieve, the location on the chip and the working bandwidth. The edge coupler, as the name suggests, can only be put on the edge of the chip, thus, it limits the usage of such kind of couplers. However, due to its high coupling efficiency and broadband operation wavelength range, such coupler is widely used in commercial products for laser packaging. Grating coupler is used for applications that do not require a wide bandwidth.

1.1.4.3 Polarization dependent devices

Since most of the devices on the standard silicon photonic platform are only for a single polarisation, thus polarization rotator or polarization converter is needed in order to manipulate two polarizations on chip.

1.2 Research direction

1.2.1 Photonic molecules

Photonic molecules are structures formed by the coupling of two or more optical micro-cavities (which could be referred to as a photonic atom in the molecule). Photonic molecules can be used to realize complex optical energy states and modes, analogous to those found in molecules, with properties useful for applications like spectral engineering, analog computation, many body physics simulations, and quantum optics.

These optical cavities can be constructed by means of a circular waveguide structure, called a ring resonator, resulting in a ring lattice structure. Some designs for photonic molecules maded with coupled ring resonators are given in Fig. **??**.
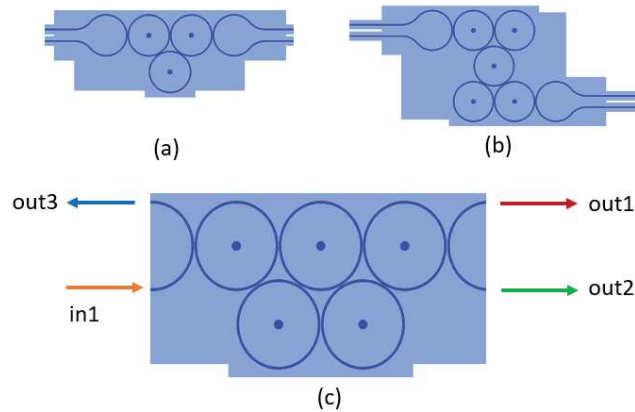
Figure 1.5: (a),(b) and (c) are three examples of photonic molecules built with coupling ring resonators.

There are several ways to model the ring lattice, including the Coupled Mode Theory (which tries to build a physical model of the structure at large) and a circuit modeling approach in which this structure is being viewed as a complex network of several discrete components (the circuit modeling is implemented via the Caphe engine, from Luceda photonics). In this research the circuit model is built by the Caphe engine, the spectral response of the five ring structure given in Fig. 1.5(c) is shown in Fig. 1.6.

The experimental result for the five ring structure is given in Fig. 1.7.First results indicate that the experimental results don't agree with the simulations for large lattices. The hypothesis for the origin of this mismatch is believed to be geometrical variations on the optical chip, leading to variations in effective index. To compensate for these variations due to fabrication, it should be possible to compensate for them by placing phase shifters (implemented by a heating element) at certain locations in the lattice or the photonic molecule structure could be implemented on a fully programmable mesh circuits, in which the couplings and phase of each individual component could be controlled or programmed, thus helps to compensate the fabrication variation.

1.2.2   Programmable mesh circuit

The programmable PICs are based on the concept that the flow of light could be manipulated in real-time. The light redistribution could then be performed under
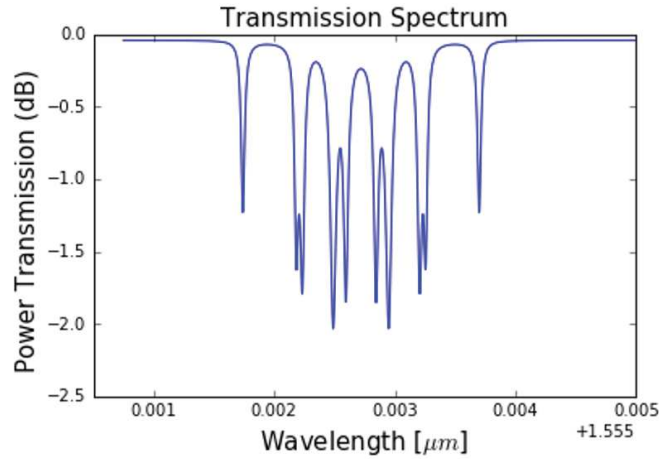
Figure 1.6: Spectral response by Caphe model of the five ring structure, the coupling between forward mode and backward mode results into a complex spectrum.
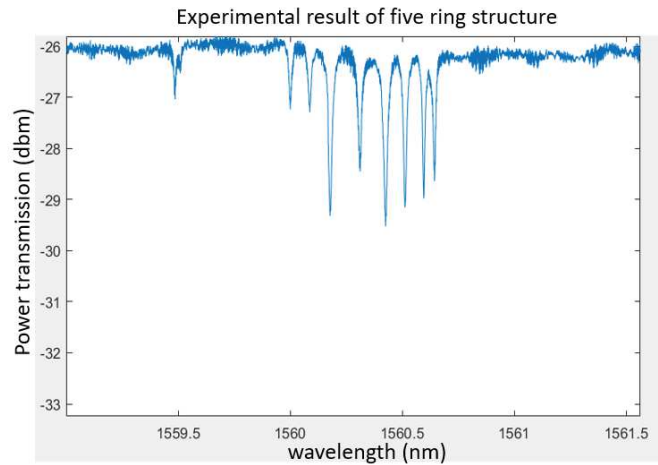
Figure 1.7: Spectral response by Caphe model of the five ring structure, the coupling between forward mode and backward mode results into a complex spectrum.

software control. There are two types of programmable circuits, feed-forward mesh and feed-back mesh circuit.

In forward only mesh networks [21] [22], light flows in one direction, interfering in 2×2 gates at every stage, Fig. 1.8a is a simple example of a forward only mesh.The feed-forward mesh circuit is able to perform linear optical computations such as matrix-vector products.

The feed-back mesh circuit [23] [24] is recirculating, where light can be routed

in loops and back to the input ports. The feed-back loop can be connected in different typologies, including square mesh shown in Fig. 1.8b, hexagonal mesh shown in Fig. 1.8c, triangular mesh shown in Fig. 1.8d and alternative connection typologies. When evaluating these typologies against integration metrics (such as footprint or gates per area) or functional metrics (such as reconfiguration capability,losses,and the choice of filter periodicity) a hexagonal mesh is particularly attractive, especially because all ports can be used as input or output interchangeably. However as we can see from Fig. 1.8c, in order to build a single ring resonator, 6 2×2 gates on each side of the hexagonal cell form a circle, thus the FSR of the ring resonator of the hexagonal cell and the internal loss of it is higher compared to normal ring resonator where only one gate is needed. Beside, the more the gates, the higher the power consumption. In other words, the general purpose programmable chip sacrifices the performance to get the programmability and configurability. Same as electronics, the ASIC chips are better in performance.
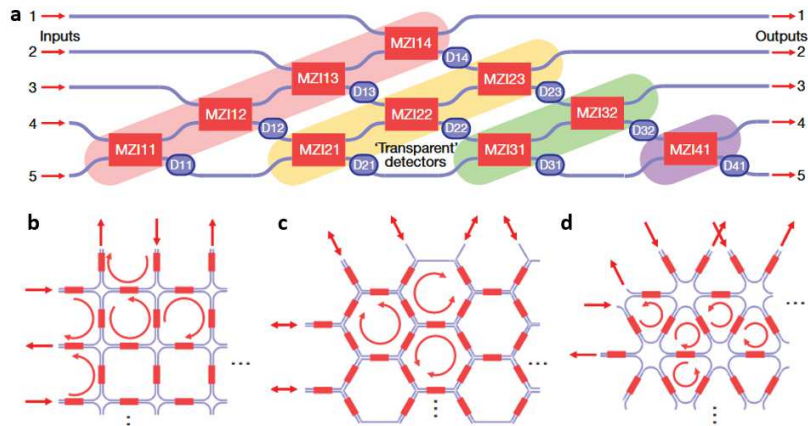
Figure 1.8: (a) Forward-only meshes of 2×2 optical gates. (b) square cells (c) hexagonal cellls (d) triangular cells

For a large programmable PICs, not only the photonic design matters, the electronic control, packaging, algorithm and software layer are also important for the system development.

The directional coupler is an essential building block of the photonic circuit. It is used for splitting and combining light. A compact, wavelength independent directional coupler [25] is highly desired, especially for telecom applications such as wavelength-division-multiplexing [26] and signal switching [27]. In this thesis, we proposed a broadband coupler design.

1.2.2.1   Broadband coupler

An essential component in large scale programmable circuit is a directional coupler, or tunable directional coupler. Optimally, we would like to have a broadband directional coupler.

A broadband directional coupler has a constant coupling ratio with about $0.1dB$ variation over a larger wavelength range. Such broadband directional coupler can be engineered as a sub-wavelength grating assisted directional coupler [28], MZI (Mach-Zehnder interferometer) [29], and asymmetric directional coupler [25]. We have chosen the cascaded MZI as our design for broadband directional coupler. The following steps are performed in our work.

1. The component design of the broadband directional coupler is a single stage MZI. The phase difference is achieved by two waveguides with different widths.

2. The layout of the design is shown in Fig. 1.9. It is composed of a coupler section, a taper section, a S-bend section and a phase compensation section with two waveguides of different widths.

3. Each component has its own T-matrix model. The T-matrix model of the whole design is multiplication of the T-matrix of each component.And the T-matrix is compared with the FDTD simulation.

4. The T-matrix model overlooked the coupling in the taper section, thus a more accurate model based on eigenmode expansion (EME) is built by Fimmprop.

5. A parameter sweep is conducted based on the EME model. The length of the directional coupler and the length of the phase compensation section is set as parameters to be swept. The initial sweep provided us a parameter space to use in the next optimization step.

6. An optimization algorithm such as Kriging optimization is applied.

7. The optimized design is verified with FDTD simulation.

8. The broadband directional coupler will be fabricated by E-beam, the devices will be measured and the data will be compared with the simulation.

9. We could also add heaters on the phase compensation section. In this way, the design constrains will be loosened and we are also able to compensate for the fabrication variation to a certain extent.
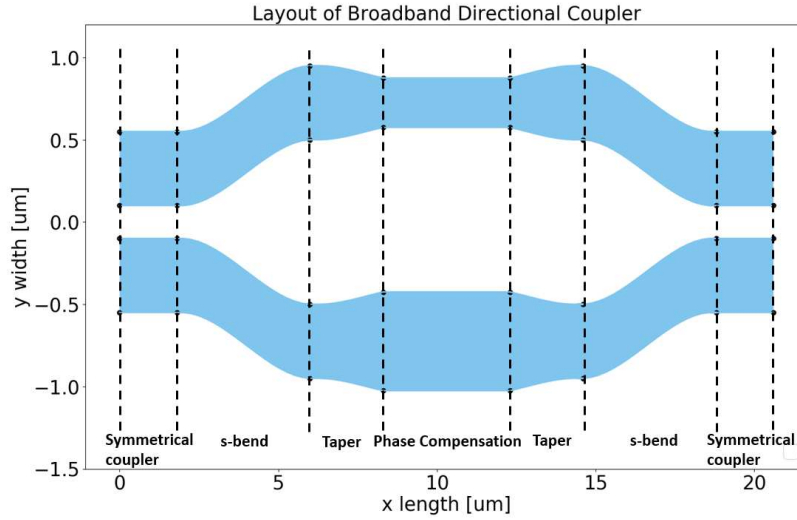
Figure 1.9: Layout of a broadband directional coupler implemented by a MZI

1.2.2.2   Tolerant, broadband, tunable coupler circuit

The broadband coupler enables the creating of more tolerant circuits and filters, but to make them programmable we need to be able to change the coupling ratio, but at the same time keep the broadband behaviour. We propose a tolerant broadband tunable coupler circuit shown in Fig. 1.10. We show that this circuit can be tuned for a uniform coupling over a wide bandwidth of 50 nm, making it easier to construct wavelength filters or route broadband light through a programmable circuit [22].

The design of the two-stage is depicted in Fig. 1.10a. The circuit connects three DCs with two sets of balanced delay lines with phase shifters. In our fabricated device we incorporated phase shifters in all arms of the circuit, so we have 4 phase shifters, but in practice it is possible to fully control the coupling with only two phase shifters. We can adjust the transmission by tuning the phase shift in the two stages. The device can be tuned from 0% to 100% as long as the three directional couplers have a balance that is better than 25:75. This makes the circuit tolerant to fabrication imperfections and even local variability, as it is not required that all three DCs perform identically.

We demonstrate that the circuit is tolerant to fabrication variation and wavelength-independent by the following simulation. We assume the circuit consists of imperfect DCs of 40:60 coupling ratio at 1550 nm. In Fig. 12, we plot the power coupling η at 1550 nm (white contours), and overlay it with the maximum deviation

$\Delta\eta$ within the wavelength range of 1525-1575 nm. For any given desired coupling value, we can tune the two phase shifters such that we obtain this coupling value within 3% over the entire wavelength range for an almost uniform response.

We can find inside the yellow contour (the dark blue region) where the cross transmission becomes almost non-dispersive indicates a flat spectral response and broadband operation. The white circles indicates the coupling ratio distribution according to the phase combination of phase shifter 1 and phase shifter 2 at 1550 nm. The yellow contour overlaps with different white circles of coupling ratio from 0% to 100%. It means that we could tune the phase shifters to find broadband operation for any arbitrary coupling ratio. Figure 1.12 shows the simulated cross power transmission for the best operating point for coupling values of 0%,10%,40%,70%,90% and 100%. The maximum dispersion of coupling power is 3% between 1525 nm and 1575 nm.

We designed and demonstrated a simplified tunable coupler circuit with 0-100% coupling range even under conditions of fabrication variations. We also show that we can bias the circuit to obtain a flat spectral response over a wavelength range of 50 nm. This work is published in [8].

1.2.2.3 Technology development of heaters

Today most programmable photonic circuits use electrically-driven heaters. These thermal tuners consume several mW electrical power, has a time constants of 10-100 μs [30]. The thermal crosstalk or the efficiency of the thermal heater could be improved with undercut designs [31].When thermal insulation is applied, heater
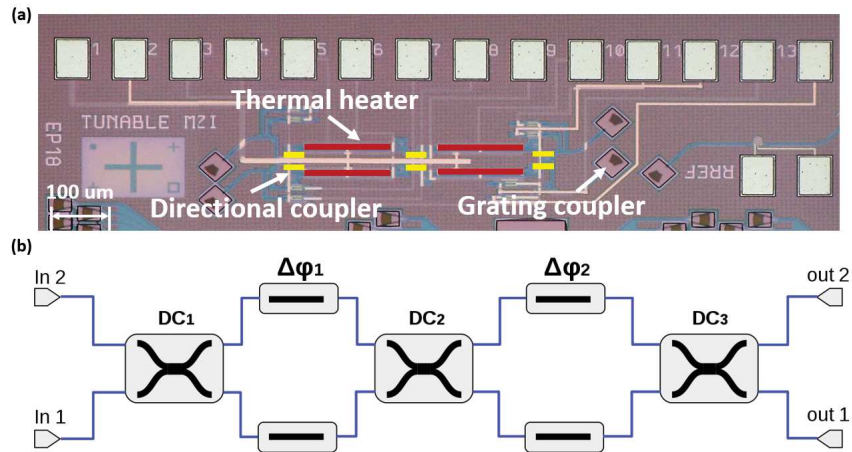
Figure 1.10: (a) Microscope picture of the fabricated device.(b) Two-Stage MZI 2×2 tunable coupler.

efficiency improves with a factor of 20, but at the cost of a slower response time. Other kinds of heaters such as a PIN diode and a resistor with diode can all work as heaters. An alternative is using the waveguide itself as a resistor, by lightly doping it, but this will induce additional loss in the waveguide.Other materials such as liquid crystal [32], piezoactuators and MEMS [33] are being investigated. The MEMS device realized in MORPHIC project [34], is broadband and "zero-charge" when latching is applied. Once such device is configured, the state will be static, the power consumption of this kind of MEMS is considered to be low compared with "always on" heaters.

1.2.2.4   Programmable filter composed by double ring loaded MZI

The current limitations for such programmable PICs lay in large insertion loss, high crosstalk, small FSR and large power consumption. In some applications, the programmable component is more versatile and has advantages in lower loss,
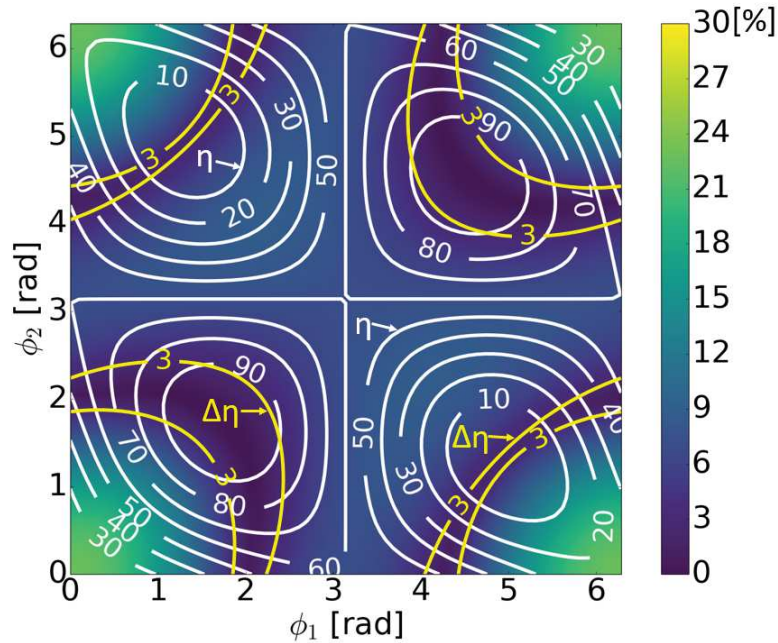
Figure 1.11: Simulated result of cross transmission η at 1550 nm and the maximum deviation of the cross coupling Δη from 1525 to 1575 for the two-stage tunable coupler with imperfect DCs of 40:60 coupling ratio. The dark lines in the graph indicate the region of 3% deviation from the desired coupling within a 50 nm wavelength range of 1550 nm. As this region contains all coupling values from 0-100%, we can tune the circuit to a 50 nm broadband coupling regime with a tolerance of 3%.
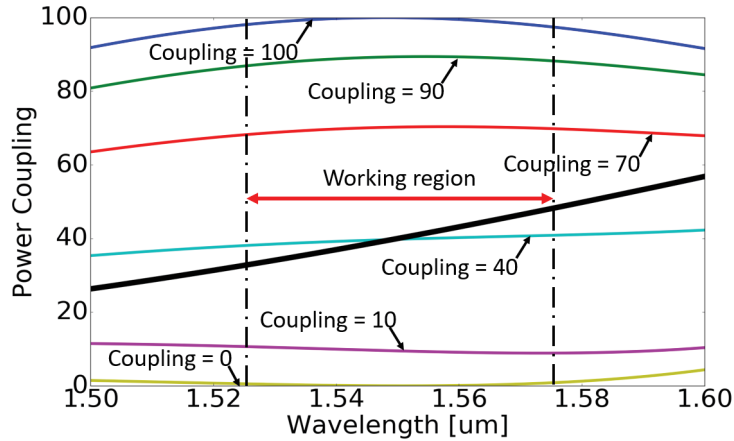
Figure 1.12: The simulated cross power transmission for 0%,10%,40%,70% 90% and 100% coupling ratio.Within the working region between 1525 nm and 1575 nm indicated by the dashed line, the device works as a broadband coupler with a deviation less than 3%. Outside this working region, the coupler suffers more wavelength dispersion. The dispersive response of a single DC with 40:60 coupling ratio at 1550 nm is also shown by black bold line.

lower cross-talk, larger FSR and so on. A programmable component has less tunable elements, therefore less power consumption and easier to control. It also has short path length, therefore has lower loss and shorter ring lengths which increasing the FSR. A programmable filter design have been proposed in this work, such programmable component is not only configurable but also addressed the problems with large programmable circuit.

The filter circuit is quite essential in lots of applications, it has its applications in telecommunication as interleaver, in quantum systems as pump rejection filter, in microwave systems as notch filter and etc. Programmable filters provide more flexibility in controlling the filters in photonic systems. The free space arbitrary waveform generator has been commercialized by Key-sight using LCoS. Here we propose a novel filter circuit that incorporates a balanced Mach-Zehnder interferometer (MZI) loaded with a double coupled ring resonator in integrated photonics. The filter circuit we propose here extends the traditional ring loaded MZI by using a double (coupled) ring resonator that links the two arms of the MZI. The schematic drawing of the filter is shown in Fig. 5.1.

The second-order filter can also be cascaded to realize higher-order filters. As shown in Fig. 5.1(b), a fourth order filter is built by cascading two second order filters.

We applied a global optimization algorithm to fit the filter parameters, where
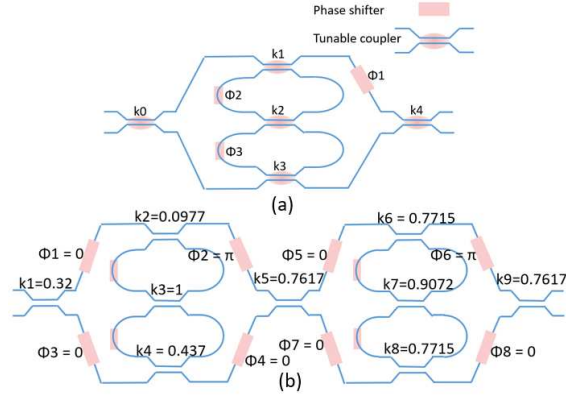
Figure 1.13: (a) Schematic drawing of the filter circuit , the phase shifter is shown as a pink box. (b) Schematic drawing of a two stage filter.

the optimization target function is carefully tailored to the problem. We applied this optimization schemes both in simulation and experiments. Since thermal cross-talk, electrical cross-talk, dispersion induced by couplers , fabrication variation of optical components will degrade our filter performance, thus the optimisation algorithm is needed in real time measurements. As the measurement data is noisy and the initial guess might be not accurate due to crosstalk, the *Powell* is chosen in experiments. The final optimization result is shown in Fig. 1.14 for three filter specifications.

We have proposed an MZI filter circuit loaded with a coupled double ring resonator to realize a configurable second-order auto regressive-moving-average (ARMA) filter, and demonstrated optimization of the tuning coefficients both in simulation and in experiments. The results of this has been submitted to scientific report.

1.3   Thesis outline

Chapter 2 covers the basics of filter design. The goal of this chapter is to introduce most of the prerequisites that will be used in later chapters. Then, in chapter 3, we will discuss the design of the passive broadband directional coupler, which is very interesting to improve the bandwidth of our filter design. In chapter 4, we will then extend this to a tunable broadband coupler circuit. In chapter 5, we will go in to the details on the principles, simulation and experiments with programmable wavelength filter based on the coupled ring loaded MZI.And in chapter 6, we will introduce some of old projects and future directions. Chapter 6 also concludes the whole thesis.
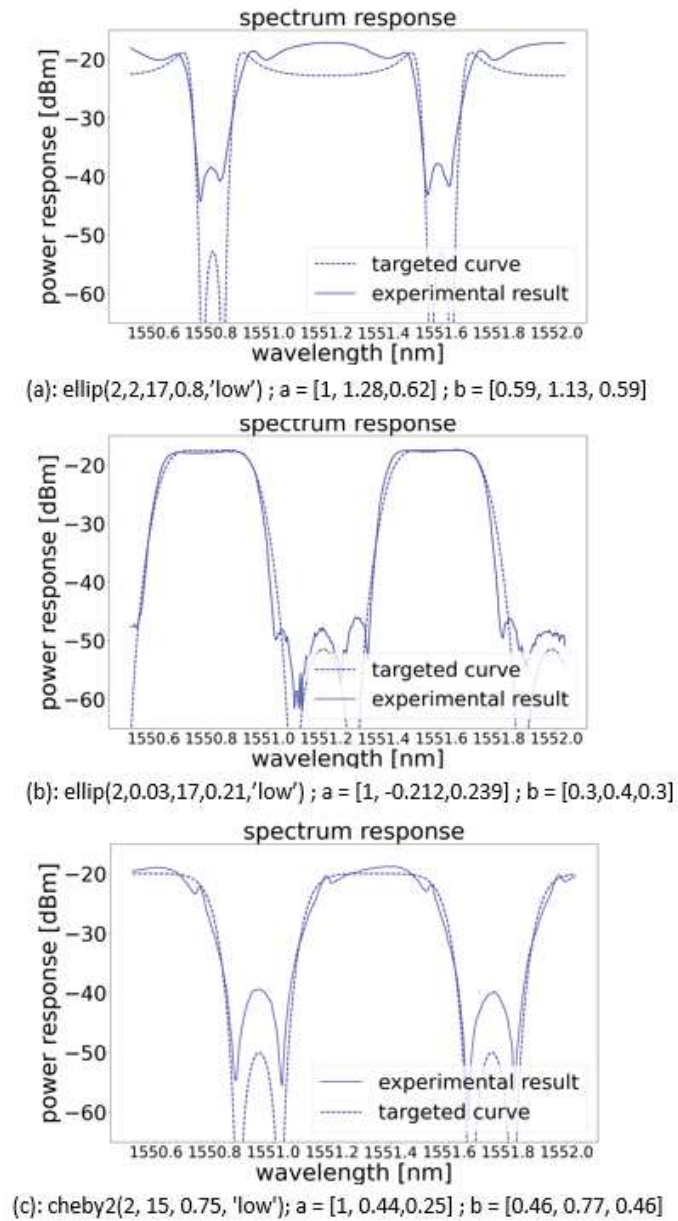
Figure 1.14: Experimental results for programmable filter design.

1.4 Publications

Publications in international journals

[1] A. Ribeiro, S. Declercq, U. Khan, M. Wang, L. Van Iseghem, W. Bogaerts
     Column-row addressing of thermo-optic phase shifters for controlling large sil-

icon photonic circuits. IEEE Journal on Selected Topics in Quantum Electronics, 26(5), p.6100708 (8 pages) doi:10.1109/JSTQE.2020.2975669 (2020)

[2] M. Wang, A. Ribeiro, Y. Xing, W. Bogaerts. *Tolerant, Broadband Tunable 2x2 Coupler Circuit*. Optics Express, 28(4), p.5555-5566 doi:10.1364/OE.384018 (2020).

[3] Y. Xing, M. Wang, A. Ruocco, J. Geessels, U. Khan, W. Bogaerts. *A Compact Silicon Photonics Circuit to Extract Multiple Parameters for Process Control Monitoring*. OSA Continuum, 3(2), p.379-390 doi:10.1364/OSAC.383711 (2020).

[4] Y. Ye, M. Wang, D. Spina, W. Bogaerts, T. Dhaene. *Time-domain characterization of photonic integrated filters subject to fabrication variations*. Journal of Lightwave Technologies, 37(21), p.5561-5570 doi:10.1109/JLT.2019.2933311 (2019).

Publications in international conferences

[5] W. Bogaerts, L. Van Iseghem, X. Chen, I. Zand, H. Deng, M. Wang, Y. Zhang, Y. Liu, K.P. Nagarjun, U. Khan. *Programmable Silicon Photonic Circuits (invited)*. publication in International Symposium on Photonic and Electronic Convergence (ISPEC 2021), (submitted).

[6] W. Bogaerts, L. Van Iseghem, X. Chen, I. Zand, H. Deng, M. Wang, K.P. Nagarjun, U. Khan. *Technologies for large-scale programmable photonic circuits (invited)*. publication in Progress in Electromagnetic Research (PIERS), China, (submitted).

[7] W. Bogaerts, L. Van Iseghem, M. Wang, H. Deng, X. Chen, I. Zand, K.P. Nagarjun, U. Khan. *Programmable Photonic Circuits (invited)*. SPIE Photonex (invited), United Kingdom, doi:10.1117/12.2600687 (2021).

[8] W. Bogaerts, L. Van Iseghem, M. Wang, H. Deng, I. Zand, X. Chen, K.P. Nagarjun, U. Khan. *Programmable Silicon Photonics (invited)*. International Conference on Solid State Devices and Materials (SSDM) , p.E-2-01 (2021)

[9] W. Bogaerts, M. Wang, X. Chen, H. Deng, I. Zand, L. Van Iseghem, K.P. Nagarjun, U. Khan. *General-Purpose Programmable Photonic Chips*. IEEE Photonics Society Summer Topicals (invited), p.WB2.1 doi:10.1109/SUM48717.2021.9505805 (2021)

[10] W. Bogaerts, X. Chen, I. Zand, M. Wang, H. Deng, L. Van Iseghem, A. Rahim, U. Khan. *Tutorial: Programmable Integrated Photonics*. European

Conference on Optical Communication (ECOC) (invited), p.paper Tu4B-1 (3 pages) doi:10.1109/ECOC48923.2020.9333192 (2020).

[11]   W. Bogaerts, X. Chen, M. Wang, I. Zand, H. Deng, L. Van Iseghem, A. Ribeiro, A. Diaz Tormo , U. Khan   *Programmable Silicon Photonic Integrated Circuits (invited)*. IEEE Photonics Conference (IPC) (invited), Canada, p.ThD2.1 doi:10.1109/IPC47351.2020.9252475 (2020).

[12]   W. Bogaerts, A. Rahim, X. Chen, L. Van Iseghem, H. Deng, M. Wang, I. Zand, A. Ribeiro, A. Diaz Tormo , U. Khan *Programmable Photonic Circuits: a flexible way of manipulating light on chips*. Frontiers in Optics (invited), United States, doi:10.1364/FIO.2020.FTh1C.1 (2020)

[13]   W. Bogaerts, A. Ribeiro, M. Wang, L. Van Iseghem, H. Deng, I. Zand, X. Chen, U. Khan *Technologies for large-scale programmable photonic circuits*. AOS Australian Conference on Optical Fibre Technology (ACOFT) and Australian Conference on Optics, Lasers, and Spectroscopy (ACOLS) 2019 (invited), p.11200-55 (2019).

[14]   M. Wang, A. Ribeiro, Y. Xing, W. Bogaerts *Tolerant, Broadband Tunable 2x2 Coupler Circuit*. IEEE Photonics Society Summer Topicals, United States, p.paper WE3.3 (2 pages) doi: 10.1109/PHOSST.2019.8794978 (2019).

[15]   A. Ribeiro, U. Khan, L. Van Iseghem, M. Wang, S. Declercq, W. Bogaerts *Driving and control techniques for large scale programmable photonics circuits*. PhotonIcs & Electromagnetics Research Symposium (PIERS) (invited), Italy, p.2568 (2019).

[16]   Y. Xing, M. Wang, A. Ruocco, J. Geessels, U. Khan, W. Bogaerts *Extracting Multiple Parameters from a Compact Circuit for Performance Evaluation*. European Conference on Integrated Optics (ECIO 2019), Belgium, p.W.Po1.9 (2019).

References

[1] Graham T. Reed. *Silicon Photonics: The State of the Art*. Wiley-Interscience, USA, 2008.

[2] A. F. Benner, M. Ignatowski, J. A. Kash, D. M. Kuchta, and M. B. Ritter. *Exploitation of optical interconnects in future server architectures*. IBM Journal of Research and Development, 49(4.5):755–775, 2005.

[3] J.D. Meindl. *Interconnect limits on gigascale integration (GSI)*. In 2001 6th International Symposium on Plasma- and Process-Induced Damage (IEEE Cat. No.01TH8538), pages 1–, 2001.

[4] W. Bogaerts, R. Baets, P. Dumon, V. Wiaux, S. Beckx, D. Taillaert, B. Luyssaert, J. Van Campenhout, P. Bienstman, and D. Van Thourhout. *Nanophotonic waveguides in silicon-on-insulator fabricated with CMOS technology*. Journal of Lightwave Technology, 23(1):401–412, 2005.

[5] J. Gonzalo Wangüemert-Pérez, Abdelfettah Hadij-ElHouati, Alejandro Sánchez-Postigo, Jonas Leuermann, Dan-Xia Xu, Pavel Cheben, Alejandro Ortega-Moñux, Robert Halir, and Íñigo Molina-Fernández. *[INVITED] Subwavelength structures for silicon photonics biosensing*. Optics Laser Technology, 109:437–448, 2019.

[6] Christopher V. Poulton, Ami Yaacobi, David B. Cole, Matthew J. Byrd, Manan Raval, Diedrik Vermeulen, and Michael R. Watts. *Coherent solid-state LIDAR with silicon photonic optical phased arrays*. Opt. Lett., 42(20):4091–4094, Oct 2017.

[7] Richard Jones, Pierre Doussiere, Jeffrey B. Driscoll, Wenhua Lin, Haijiang Yu, Yulia Akulova, Tin Komljenovic, and John E. Bowers. *Heterogeneously Integrated InPSilicon Photonics: Fabricating Fully Functional Transceivers*. IEEE Nanotechnology Magazine, 13(2):17–26, 2019.

[8] Mi Wang, Antonio Ribero, Yufei Xing, and Wim Bogaerts. *Tolerant, broadband tunable 2× 2 coupler circuit*. Optics express, 28(4):5555–5566, 2020.

[9] Hui Yu, Wim Bogaerts, and An De Keersgieter. *Optimization of Ion Implantation Condition for Depletion-Type Silicon Optical Modulators*. IEEE Journal of Quantum Electronics, 46(12):1763–1768, 2010.

[10] Georgios Sinatkas, Thomas Christopoulos, Odysseas Tsilipakos, and Emmanouil E. Kriezis. *Electro-optic modulation in integrated photonics*. Journal of Applied Physics, 130(1):010901, 2021.

[11] L. Colace, G. Masini, F. Galluzzi, G. Assanto, G. Capellini, L. Di Gaspare, E. Palange, and F. Evangelisti. *Metal-semiconductor-metal near-infrared light detector based on epitaxial Ge/Si*. Applied Physics Letters, 72(24):3175, June 1998.

[12] Hsu-Hao Chang, Ying hao Kuo, Richard Jones, Assia Barkai, and John E. Bowers. *Integrated hybrid silicon triplexer*. Opt. Express, 18(23):23891–23899, Nov 2010.

[13] Ilya Goykhman, Boris Desiatov, Jacob Khurgin, Joseph Shappir, and Uriel Levy. *Locally Oxidized Silicon Surface-Plasmon Schottky Detector for Telecom Regime*. Nano Letters, 11(6):2219–2224, 2011. PMID: 21604793.

[14] Zeqin Lu, Jaspreet Jhoja, Jackson Klein, Xu Wang, Amy Liu, Jonas Flueckiger, James Pond, and Lukas Chrostowski. *Performance prediction for silicon photonics integrated circuits with layout-dependent correlated manufacturing variability*. Opt. Express, 25(9):9712–9733, May 2017.

[15] Matteo Cherchi, Sami Ylinen, Mikko Harjanne, Markku Kapulainen, and Timo Aalto. *Dramatic size reduction of waveguide bends on a micron-scale silicon photonic platform*. Opt. Express, 21(15):17814–17823, Jul 2013.

[16] Abdul Rahim, Jeroen Goyvaerts, Bertrand Szelag, Jean-Marc Fedeli, Philippe Absil, Timo Aalto, Mikko Harjanne, Callum Littlejohns, Graham Reed, Georg Winzer, Stefan Lischke, Lars Zimmermann, Dieter Knoll, Douwe Geuzebroek, Arne Leinse, Michael Geiselmann, Michael Zervas, Hilde Jans, Andim Stassen, Carlos Domínguez, Pascual Muñoz, David Domenech, Anna Lena Giesecke, Max C. Lemme, and Roel Baets. *Open-Access Silicon Photonics Platforms in Europe*. IEEE Journal of Selected Topics in Quantum Electronics, 25(5):1–18, 2019.

[17] Maurizio Burla, Benjamin Crockett, Lukas Chrostowski, and José Azaña. *Ultra-high Q multimode waveguide ring resonators for microwave photonics signal processing*. In 2015 International Topical Meeting on Microwave Photonics (MWP), pages 1–4, 2015.

[18] Frederik Van Laere, Günther Roelkens, Melanie Ayre, Jonathan Schrauwen, Dirk Taillaert, Dries Van Thourhout, Thomas F. Krauss, and Roel Baets. *Compact and Highly Efficient Grating Couplers Between Optical Fiber and Nanophotonic Waveguides*. J. Lightwave Technol., 25(1):151–156, Jan 2007.

[19] Wim Bogaerts, Vincent Wiaux, Pieter Dumon, Dirk Taillaert, Johan Wouters, Stephan Beckx, Joris Van Campenhout, Bert Luyssaert, Dries Van Thourhout, and Roel Baets. *Large-scale production techniques for photonic*

nanostructures. In Louay A. Eldada, editor, Nano- and Micro-Optics for Information Systems, volume 5225, pages 101 – 112. International Society for Optics and Photonics, SPIE, 2003.

[20] Masatoshi Tokushima, Jun Ushida, Toshinori Uemura, and Kazuhiko Kurata. *Shallow-grating coupler with optimized anti-reflection coating for high-efficiency optical output into multimode fiber*. Applied Physics Express, 8(9):092501, aug 2015.

[21] David A. B. Miller. *Self-configuring universal linear optical component*

Invited

. Photon. Res., 1(1):1–15, Jun 2013.

[22] Antonio Ribeiro, Alfonso Ruocco, Laurent Vanacker, and Wim Bogaerts. *Demonstration of a 4×4 port universal linear circuit*. Optica, 3(12):1348–1357, Dec 2016.

[23] Wim Bogaerts, Daniel Pérez, José Capmany, David A. B. Miller, Joyce Poon, Dirk Englund, Francesco Morichetti, and Andrea Melloni. *Programmable photonic circuits*. Nature, 586(4):1476–4687, 2020.

[24] Daniel Pérez, Ivana Gasulla, and José Capmany. *Programmable multifunctional integrated nanophotonics*. Nanophotonics, 7(8):1351–1371, 2018.

[25] Zeqin Lu, Han Yun, Yun Wang, Zhitian Chen, Fan Zhang, Nicolas Jaeger, and Lukas Chrostowski. *Broadband silicon photonic directional coupler using asymmetric-waveguide based phase control*. Optics Express, 23:3795–3808, 02 2015.

[26] Folkert Horst, William M.J. Green, Solomon Assefa, Steven M. Shank, Yurii A. Vlasov, and Bert Jan Offrein. *Cascaded Mach-Zehnder wavelength filters in silicon photonics for low loss and flat pass-band WDM (de-)multiplexing*. Opt. Express, 21(10):11652–11658, May 2013.

[27] Qing Fang, Jun Feng Song, Tsung-Yang Liow, Hong Cai, Ming Bin Yu, Guo Qiang Lo, and Dim-Lee Kwong. *Ultralow Power Silicon Photonics Thermo-Optic Switch With Suspended Phase Arms*. IEEE Photonics Technology Letters, 23(8):525–527, 2011.

[28] Lu Liu, Qingzhong Deng, and Zhiping Zhou. *Subwavelength-grating-assisted broadband polarization-independent directional coupler*. Opt. Lett., 41(7):1648–1651, Apr 2016.

[29] K Jinguji, N Takato, A Sugita, and M Kawachi. *Mach-Zehnder interferometer type optical waveguide coupler with wavelength-flattened coupling ratio*. Electronics Letters, 26(17):1326–1327, 1990.

[30] Adil Masood, Marianna Pantouvaki, Guy Lepage, Peter Verheyen, Joris Van Campenhout, Philippe Absil, Dries Van Thourhout, and Wim Bogaerts. *Comparison of heater architectures for thermal control of silicon photonic circuits*. In 10th International Conference on Group IV Photonics, pages 83–84. IEEE, 2013.

[31] Adil Masood, Marianna Pantouvaki, Guy Lepage, Peter Verheyen, Joris Van Campenhout, Philippe Absil, Dries Van Thourhout, and Wim Bogaerts. *Comparison of heater architectures for thermal control of silicon photonic circuits*. In 10th International Conference on Group IV Photonics, pages 83–84, 2013.

[32] Wim Bogaerts, Lukas Van Iseghem, Pierre Edinger, Hamed Sattari, Alain Yuji Takabayashi, Xiangfeng Chen, Hong Deng, Peter Verheyen, Antonio Ribeiro, Umar Khan, Niels Quack, and Kristinn B. Gylfason. *Low-Power Electro-Optic Actuators for Large-Scale Programmable Photonic Circuits*. In Conference on Lasers and Electro-Optics, page STh1Q.4. Optical Society of America, 2021.

[33] Wim Bogaerts, Pierre Edinger, Alain Yuji Takabayashi, Iman Zand, Xiangfeng Chen, Xiaojing Wang, Hamed Sattari, Peter Verheyen, Moises A. Jezzini, Giuseppe Talli, Saurav Kumar, Marco Garcia Porcel, Antonio Ribeiro, Gaehun Jo, Niels Quack, Kristinn B. Gylfason, Frank Niklaus, and Umar Khan. *Building Large-Scale Programmable Photonic Circuits Using Silicon Photonic MEMS*. In OSA Advanced Photonics Congress (AP) 2020 (IPR, NP, NOMA, Networks, PVLED, PSC, SPPCom, SOF), page PsTh1F.1. Optical Society of America, 2020.

[34] Carlos Errando-Herranz, Alain Yuji Takabayashi, Pierre Edinger, Hamed Sattari, Kristinn B. Gylfason, and Niels Quack. *MEMS for Photonic Integrated Circuits*. IEEE Journal of Selected Topics in Quantum Electronics, 26(2):1–16, 2020.

2

Component design and Filter design basics

Optical filters are key function for photonic circuits, they are used for many applications including WDM channel selection, sensors, spectrometers, interleavers and etc. Optical filters have many different requirements, it is important to have a good understanding of filters, therefore we give an introduction to filters. Filters can be implemented as building blocks/geometries (e.g. gratings) or as circuits. In both cases, we need to understand the fundamental building blocks and we need to model them. That is why we first explain the different modelling and design strategies for building blocks.

The chapter is organized as following: first, the component design basics are introduced to the reader. We start with the modelling approaches including EME, 3D FDTD, 2D FDTD, BPM, CMT, TMM. Then the comparison between EME and FDTD is made. Then we go to filter design basics. Different types of filters, specification of filters, the mathematical representation of the filter design , the classification of different types of filters are introduced. Then we conclude this part with the applications of the filters. The chapter servers as prerequisites for chapter 3 and chapter 5.

2.1   Component design basics

Typical circuits consist of a few fundamental building blocks of silicon photonic systems building blocks built on a silicon-on-insulator wafer: passive components such as wave- guides, couplers and filters, and active devices such as modulators and photodetectors. Using these, large systems can be pieced together without significant re-engineering at the device level. The performance of the components are determined by its geometry which is defined by the mask layout. The modelling of these components is done by simulating the physics inside. For passive blocks, the modelling is by solving the Maxwell's equations. The modelling of active blocks involves the electrical and thermal modelling as well.

The behaviour of passive blocks is captured in a scatter matrix, which describes coupling from port (mode) to port (mode). This scatter matrix is reciprocal if the component is not time-varying.

There are different techniques to model a passive block, including EME, FDTD, TMM, BPM and etc. Each has its advantages and weaknesses.

2.1.1   Modelling and design approaches

In this section, we present an overview of the simulation and design tools for silicon photonic component and circuit design. The broadband coupler in chapter 3 was designed with Eigenmode solver for different coupling cases.

2.1.2   Mode solvers

The mode can be calculated by different methods. These methods are FMM, FDM, FEM solver and effective index method.

The FDM solver is also called finite difference mode solver. The non-uniform meshes is supported by it, with automatic refinement in regions where higher resolution is needed. The FDM solver is particularly well suited to model wavegudies with high index contrast waveguides, bent waveguides, waveguides with curved interfaces.

FMM Solver is used to find the modes of a polarisation-independent structure. A lot of parameters can be calculated for each mode, including the group index, mode dispersion, effective index, mode loss in the case of leaky modes or bend modes. These parameters can be scanned by varying geometry of the waveguide, allowing to fine tune the design for specific purposes. The FMM solver is recommended for waveguides with a rectangular geometry, or a geometry that can be simply discretised into rectangles, typically epitaxially grown structures, SOI structures, ridge and rib waveguides.

The FEM solver is ideal to solve complex waveguide geometries whose highly optimised mesh can adapt itself to virtually any arbitrary shape. The FEM solver

uses automatic mesh refinement techniques which allow it to increase the resolution exactly where it is needed as shown in Fig. 2.1.
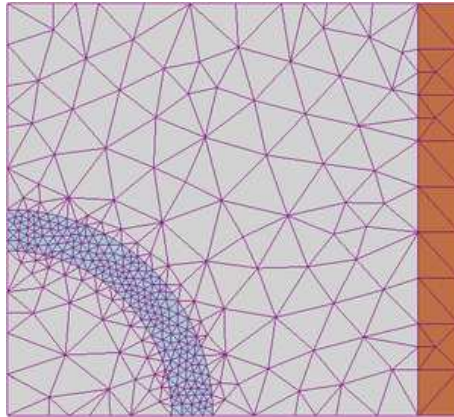
Figure 2.1: FEM solver

The effective index mode solver is an approximate method which is both fast and reliable in finding the estimates for modes.The effective index mode solver is best for weakly guided structures and 1D+z calculations.

2.1.2.1 Eigenmode Expansion Method (EME)

The EME method is a frequency domain method for solving Maxwell's equations. This methodology involves 2 steps [1]:

1. The modal decomposition of electromagnetic fields into a basis set of eigenmodes. These modes are computed by dividing the geometry into multiple cells and then solving for the modes at the interface between adjacent cells. Scattering matrices for each section are then formulated by matching the tangential E and H fields at the cell boundaries. This is the most time consuming portion of the EME calculation. In this step, FDE solver is used.

2. The simulation is now in analysis mode, and the solution to each section can be propagated bi-directionally to calculate the S matrix of the entire device. The internal fields can also be reconstructed, if desired. This step can be carried out very quickly.Once in analysis mode, the user can change the propagation distance of each section arbitrarily without having to repeat step 1. This is why the EME method is very efficient for scanning the lengths of devices.

Eignenmode calculations are useful in determining the band structures in periodic structures such as photonic crystals and Bragg gratings, Lumerical MODE is

well suited for structures such as MMI, directional couplers, tapers, gratings, etc. It is implemented in CAMFR , FIMMPROP and Lumerical MODE.

This method will be used intensively in the following simulation for the broadband coupler. And the main advantage of such method is that the change of the length will not cost more simulation time, thus it is very friendly if sweeping of length for a component is necessary.

2.1.2.2   3D FDTD

The most general and rigorous time-domain approach is the finite difference time domain (FDTD) method, in the design of the broadband coupler, the FDTD is used to verify the simulation result from Fimmprop.

The FDTD technique is a numerical method used for solving the three-dimensional (3D) Maxwell equations. This technique is particularly useful for analyzing the interaction of light with complicated structures with sub-wavelength-scale features. FDTD is the numerical calculation for Maxwell's equations, the accuracy converges to the exact solution when the mesh size getting smaller. FDTD is a time domain method and simulates the propagation of a electromagnetic pulse. In the spectral domain, it contains a broad spectrum of wavelength components. Thus, a single simulation provides the response of a optical system for a wide range of wavelengths. FDTD can model dispersive and nonlinear materials, thus it can be extended to include electronic interactions such as those found in semiconductor lasers and optical amplifiers.

The 3D FDTD is quite computationally expensive since the simulation timestep is sub-femotosecond. The Lumerical FDTD Solutions efficiently and accurately models the device response over a wide optical bandwidths with the material dispersion taken into account. The S-parameters generated with Lumerical FDTD is later used for system modelling. In the broadband circuit simulation, the S-parameters generated or measured with real experiments are inserted in the circuit model. When simulating S-parameters in FDTD, multiple simulations are needed to know the coupling from each port to each other port. In some cases, one can use symmetry and reciprocity to reduce the number of simulations. Actually this technique can be even generalized for the system level simulation with Ipkiss.

For calculating S-parameters, the FDTD solver needs to calculate the overlap with the eigenmodes of the waveguide ports. This is only analytically correct for the center wavelength of the pulse. For other wavelengths, the eigenmode overlap calculation will have a slight error. So it is often a good idea to simulate the S-parameters for a few central wavelengths.

FDTD calculations can be used for calculation of waveguide bends, coupling coefficients in directional couplers, fiber grating couplers, edge couplers, Y-branch splitters, waveguide crossings, and polarization splitter rotators.

The procedure for FDTD simulation is described as following:

1. The optical materials such as silicon, silicon oxide, germanium, metals are defined.

2. The structure is drawn, either via GUI or generated by the script. The structure geometry could be parameterized , which helps with design optimization.

3. The simulation volume is defined. Normally the device should fit in the simulation space, sometimes, the simulation area can be just a fraction of the total device extent. Several simulation parameters need to be specified.

   (a) Mesh: the mesh is defined by the number of mesh points per wavelength in the material. The smaller the mesh, the larger the simulation time.

   (b) The boundary condition is defined. Normally the boundary condition of perfect matching layers (PML) is used. The PMLs are used to absorb all the light leaving the simulation and it is implemented by numerous layers, which consumes more computation time. Metallic boundaries (perfect reflectors) are used when there is an expectation that no light will be incident on a boundary.

   (c) The simulation time for feed-forward designs such as directional couplers, grating couplers, Y-branches are typically estimated by $t = L/v_g$, where L is the propagation length, v_g is the group velocity in a certain material. Thus we normally specify a much larger time than t and when the residual fields in the simulation volume have faded out below a certain threshold.

4. The optical sources are added. The source is usually defined by calculating the modes for the waveguide and the fundamental TE mode is chosen and launched into the waveguide. The central wavelength is specified with an optical bandwidth. The source should be placed within the simulation volume and $1 - 2$ mesh points away from the boundary.

5. Monitors are added. Monitors are used to measure the optical field quantities, both E and H, at the chosen locations. A 2D monitor is used to measure the field profile at the output of the waveguide. A mode monitor takes this field profile and overlaps it with the local waveguide mode.

6. Convergence testing is performed. The simulation results should converge to a stable value when decreasing the mesh size and increasing the simulation volume.

7. Analyses are performed. This type of analyse depends very much on the design you have.

8. Parameter sweeping. Numerous simulations are performed for various geometric parameters, wavelengths, polarization, etc. Optimization algorithm , such as genetic algorithm or particle swarm algorithm can be used in the optimization. In broadband device optimization, particle swarm are utilized in the optimization process.

2.1.2.3   2D FDTD

The 2D FDTD is applied to structures which are invariant in one dimension. This method does not consider coupling between the TE and TM modes, hence it can not be used to model devices such as polarization rotators. Fiber grating couplers with straight gratings can be approximated with gratings that are infinitely long. The 2D FDTD simulation can be done in seconds while it may take minutes or hours with 3D FDTD. It is normally used for large devices and prototyping designs when parameters sweeping is needed.

2.1.2.4   Beam Propagation Method (BPM)

BPM is developed for slowly varying structures with small index of refraction contrasts. This technique is suitable for designing "sub-circuit" components such as arrayed waveguide gratings and Mach-Zehnder interferometers.

   Not in submicron silicon photonics. Explain the technique a bit more, and explain why it is not suitable for high-contrasts structures. 8-9 lines should be enough, but now it is not clear to people who are not familiar with the field.

2.1.2.5   Coupled Mode Theory (CMT)

The coupled mode theory is based on perturbation, the set of modes of the system is perturbed. For example, the modes of a directional coupler is calculated first as two separated waveguide modes, then the two waveguides are brought together, there is the coupling between them, the original waveguide modes are slightly perturbed. The Bragg gratings are also considered as forward- and backward-travelling modes for the straight waveguide, then the grating induces perturbations that couples the forward- and backward- going modes.

2.1.2.6   Transfer Matrix Method (TMM)

TMM provides an exact solution for one-dimensional structures such as thin-film reflectors, Distributed Bragg Reflectors in Vertical Cavity Lasers (VCSELs), etc.

2.1.3 Comparison between EME and FDTD

In this section, a comparison between EME and FDTD is done. Both methods are widely used in component design, however both of them have advantages and disadvantages.

The FDTD method scales well with parallelization, the large simulation could be cut into pieces and each could be simulated separately. Such parallelization would help save the simulation time. FDTD simulates the propagation of a pulse of light (tens to hundreds of femtoseconds long), which contains a broad spectrum of wavelength components. The system's response to this short pulse is related to the transmission spectrum via the Fourier transform. Thus, a single simulation provides the response of the optical system for a wide range of wavelengths at once.The boundary conditions are defined as Perfect Matching Layers ,which are used to absorb all the light leaving the simulation.The FDTD also converges well for arbitrary geometries. FDTD converges as the mesh size is reduced but halving of the unit cell comes with a 16x increase in simulation time.

For the EME simulation, the computational cost scales well with propagation distance. When we only would like to change the distance of a certain cell in the EME simulation, for example a taper simulation, the modes calculated by the previous simulation could be reused and only a distance change is applied in the S-matrix, thus the length scan of a component can be very quick. This is also the reason why we chose to use EME for our broadband coupler simulation, since the length of each section would be an important parameter for the optimization. The EME can also handle periodic structures along the propagation direction very well. EME converges as the number of modes is increased, and as the mesh size in the transverse direction is reduced.

The EME thus is better than FDTD for design with large structure length and only 1 section is needed for long uniform regions such as MMI. The FDTD is favorable for its broadband simulation and it is normally used for 3D scattering problems, splitters and grating couplers.

2.2 From components to circuits

These circuit simulations rely on behavioral models for each of the devices or components in the circuit. A behavioral model allows to simulate the circuit sufficiently fast without loosing too much accuracy. The behavioral model for a passive device is a scatter matrix, which is extracted from FDTD, EME , etc. The behavioral model could also be the analytical formula fitted to a measurement result. To make a circuit, the components are connected together, and the scatter matrix of the entire circuit can be calculated from the S-matrix of the components and the connectivity matrix. The scatter matrix of the entire circuit is a more approximate

but faster model compared to a full physical simulation such as FDTD or BPM.

For time-domain simulations, signals are propagated between the compoennts and coupled from the input ports to the output ports described by a the model of the building blocks.

2.3   Filter Design Basics

Optical filters have been widely used in lots of applications, such as telecommunication interlevers , spectroscopy and oscillators. An optical filter is basically a 4- port device including in, pass, drop, and add port (add port is sometimes not needed and drop port is sometimes just loss or radiation). It basically passes signal of desired wavelength and rejects all the other wavelengths as designed.

2.3.1   Different types of filters

Filters are widely used in optical communication systems- filters, bandpass filter, multiplexer and optical add-drop multiplexer. Interleavers are periodic bandpass filters.

Bandpass filters (BPFs) are a type of filter that suppresses the optical power transmission outside the filterband but allows a certain wavelength window to pass. In case of a single channel transmission, the bandpass filter plays a role of reducing the noise added by optical amplifiers thus improves the signal to noise ratio (SNR). BPFs are also an essential components used for multiplexing and de-multiplexing wavelengths in a WDM system. The function of a bandpass filter is shown in Fig. 2.2 (a). Low-pass filters (LPF) and high-pass filters (HPF) are filters which can provide a sharp cut-off either above or below a particular wavelength. The low-pass filter transmitted long wavelength radiation, while the high-pass filter blocks the long wavelength transmission.

As shown in Fig. 2.2 (b), a multiplexer combines different wavelengths into a single channel. The same device called "demultiplexer" separates different wavelengths to different outputs. The multiplexers and de-multiplexers are basic components for WDM transmitters , WDM receivers, and optical crossconnect (OXC), which could separate wavelength channels from the incoming waveguide or fiber and redistribute them to outgoing waveguides or fibers. Another important device for WDM system is called optical add-drop multiplexer (OADM) which is a combination of filters and maybe a wavelength converter. The working principle of a OADM is shown in Fig. 2.2 (c), where a particular wavelength channel is added to and another wavelength channel is deducted from the WDM spectrum.
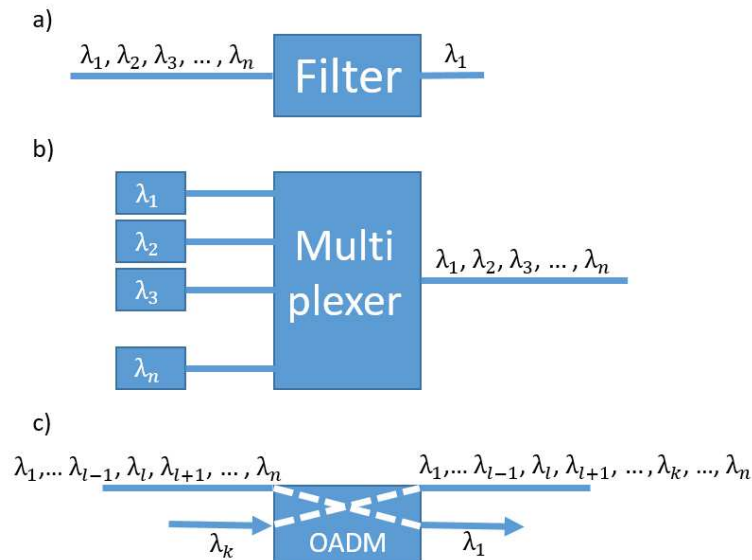
Figure 2.2: (a) bandpass filter (b) multiplexer which combines different wavelengths into single output (c) optical add-drop multiplexer where channel λ_k is added to and channel λ_i is dropped from the WDM spectrum

2.3.2 Specifications of wavelength filters

In general, the design parameters for a bandpass filter shown in Fig. 2.3 are passband width, stopband rejection, and the transition width between passband and stopband. The dispersion characteristics must also been engineered or controlled well.

For different systems, the specifications of filter design is different, below is a list of specifications for a WDM filters.

1. Insertion loss. Insertion loss is the loss from the input to the output of a filter. It should be low.

2. Polarisation-dependent loss (PDL). This kind of loss is independent of the state of polarisation of the incoming signals.

3. Temperature drift. The temperature drift is the wavelength drift when the temperature is changed. The temperature drift should be low, there is also research to make temperature tolerant or fabrication tolerant filter design.

4. Passband width. The passband width is usually defined by the 3dB bandwidth.
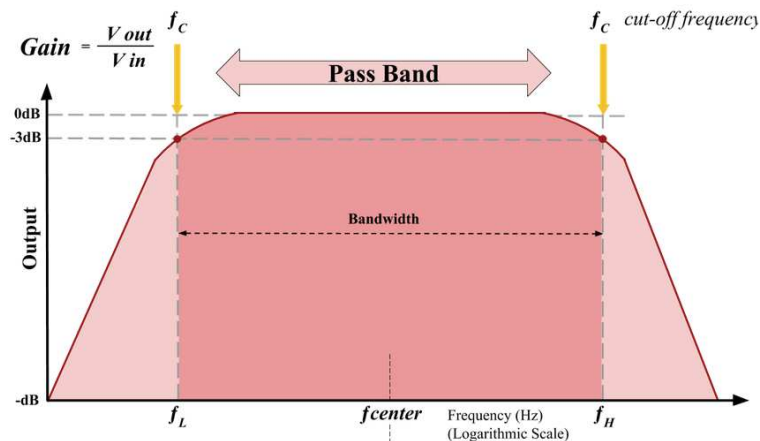
Figure 2.3: A bandpass filter with low cutoff frequency (fL), center frequency (fC), and high cutoff frequency (fH) shown in relationship to bandwidth and pass band.The gain for the optical filter is normally 1 when no amplifier is included in the filter.

5. Crosstalk. Crosstalk is defined as the light transmitted to the adjacent channels.

6. Group delay. Group delay is the time delay of the amplitude envelopes of the various sinusoidal components of a signal through a device under test, and is a function of frequency for each component. Phase delay, in contrast, is the time delay of the phase as opposed to the time delay of the amplitude envelope.

7. Free spectral range (FSR). The FSR describes the spectral periodicity of the filter transmission function.

8. Intra-band ripple and out-of-band ripple. It is defined by ripples inside the passband and ripples outside the passband.

9. Finesse. The finesse is defined as the FSR divided by the 3dB width of the filter.

10. Tuneability. Tuneability is defined as the ability to reconfigure the filter function or tuning the centre wavelength of the filter response.

However in most of the cases, we are designing filters with the help of some specific filter synthesis functions such as Butterworth filter, elliptical filter, chebyshev type I and type II filters. Given specifications for the filter, we could choose certain type of filter of the desired order that best mimics the response of the targeted filter. This procedure could also be helped with the vector fitting method [2].

2.3.3 Digital Filter Concepts for Optical Filters

Optical filters are normally modeled as digital filters. In this section, some basics of the digital filter concepts are being presented.

2.3.3.1 Discrete Signals

A discrete signal [3] is obtained by sampling a continuous time signal $x(t)$ at $t = nT$, where T is the sampling interval and n is the sample number. T is the unit delay. The Fourier transform [4] of such a sequence has a sum instead of an integral and it is given in Eq. 2.1.

$$X(f) = \sum_{n=-\infty}^{+\infty} x(nT)e^{-j2\pi f nT} \tag{2.1}$$

where f denotes the absolute frequency. The normalized frequency is denoted as $\nu = fT = f/FSR$, where the FSR is the period of the signal. The normalized angular frequency is $\omega = 2\pi\nu$. A discrete signal is often represented by x[n]. The discrete-time Fourier transform (DTFT) of Eq. 2.1 is defined as

$$X(\nu) = \sum_{n=-\infty}^{+\infty} x[n]e^{-j2\pi\nu n} \tag{2.2}$$

The Z-transform of the DTFT for discrete signals is defined by substituting z for $e^{j\omega}$ in Eq. 2.2. The Z-transform is given as follows:

$$H(z) = \sum_{n=-\infty}^{+\infty} h(n)z^{-n} \tag{2.3}$$

where $h(n)$ is the impulse response of a filter and z is the complex number that may have any magnitude.

2.3.3.2 Mathematical representation of a array waveguide grating (AWG)

The AWG could be generalized into interferometers which split incoming light into many paths, in a wavelength independent way, delayed and recombined. The splitting and recombining ratios, as well as delays would determine the spectrum response.

As is shown in Fig. 2.4, the incoming light beam is separated into M+1 parts, the splitting ratio is defined by the b_i coefficients. The split light is transmitted through different delay lines. The combination of different delay lines would undergo interference depending on the relative phase shifts. The time domain equation for such AWG system is given in Eq. 2.4.
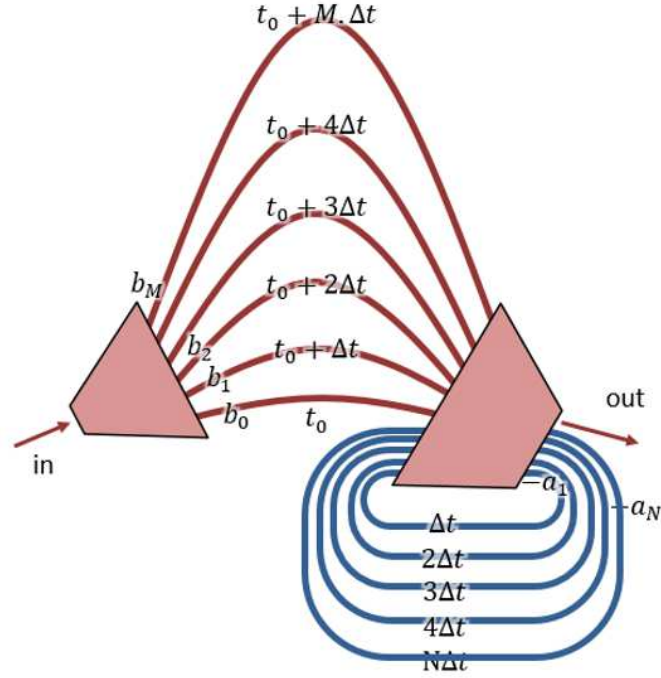
Input signal is fed back with a delay

Figure 2.4: light is distributed into M+1 beams and each beam is delayed for a certain time constant, the input signal is also feedback with delay lines.

$$y(t) = b_0 x(t) + b_1 x(t - \Delta t) + ... + b_N x(t - N\Delta t) \tag{2.4}$$

In some cases, a ring resonator or a feedback delay lines are introduced into the system. Similar as the feedforward delay line, the splitting coefficients of the feedback delays are denoted as a_1-a_N.

The discrete linear system with both feedback and feedforward delay lines with a discrete input signal has the following relationship:

$$\begin{aligned} y(n) = b_0 x(n) + b_1 x(n-1) + ... + b_M x(n-M) \\ -a_1 y(n-1) - ... - a_N y(n-N) \end{aligned} \tag{2.5}$$

The weights are given by the a and b coefficients, and they are corresponding to the splitting ratio of the input and output star coupler of the AWG.

The z-transformation of Eq. 2.5 is denoted as H(z).

$$H(z) = \frac{\sum_{m=0}^{M} b_m z^{-m}}{1 + \sum_{n=1}^{N} a_n z^{-n}} = \frac{B(z)}{A(z)} \tag{2.6}$$

A(z) and B(z) are N_{th} and M_{th} order polynomials, respectively. The roots of the numerator polynomial of H(z) are called zeros, and the roots of the denominator are called poles of the system. H(z) can be further written in terms of the roots of the polynomials in Eq. 2.7.

$$H(z) = \frac{\Gamma_z^{N-M} \prod_{m=1}^{M}(z - z_m)}{\prod_{n=1}^{N}(z - p_n)} \tag{2.7}$$

The zeros are represented by z_m. A zero that appears on the unit circle, $|z_m| = 1$, results in zero transmission corresponding to normalized frequency. This corresponds to a comb of frequencies. The poles are represented by p_n. And the gain for the system is set by Γ. For passive filters, the transmission can never exceeds 1. The gain can be added by incorporating SOA in the system.

Normally the matlab toolbox will give the pole zero plot for a filter when the a_i and b_i are given. The pole-zero plot is equivalent to its spectrum response, the zeros are designated by o's and poles by x's. For example, if we would like to design a Chebyshev type II low pass filter, with a stop band of 10-dB of magnitude response (20 dB for power response) and a normalized edge frequency of 0.5 π rad/sample. The transfer function given in Eq. 2.8.

$$H_z = \frac{1 - 0.29z^{-1} + 0.27z^{-2}}{0.37 + 0.25z^{-1} + 0.37z^{-2}} \tag{2.8}$$

The pole-zero plot for the given Chebyshev type II filter and its corresponding spectrum response is given in Fig. 2.5.
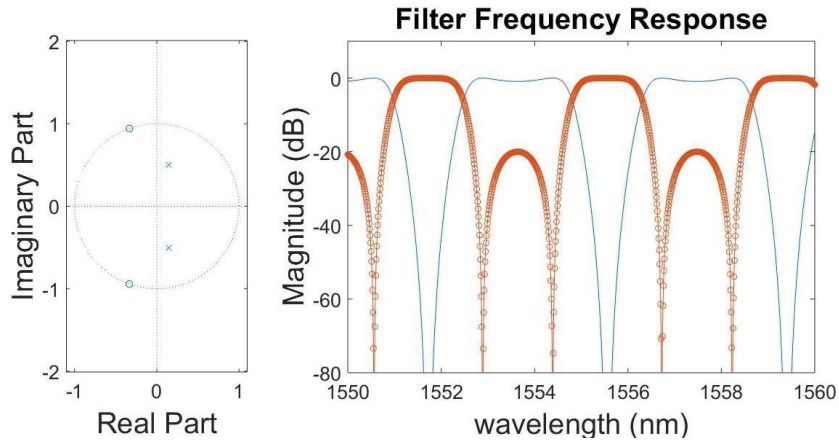
Figure 2.5: (a) pole zero plot (b) filter frequency response

The whole description for a filter with forward and feedback delay lines could be generalized to other filters as well.

2.3.4   Classification of different types of filters

When implemented as a waveguide circuit, optical filters are composed of couplers, delay lines, phase shifters, or ring resonators. These components are used to manipulate light to have constructive or destructive interference at certain wavelengths, such that a filter passband is generated. We can identify two basic classes of filters, i.e. finite impulse response (FIR) filter and infinite impulse response (IIR) filter. A FIR filter is usually composed by forward delays such as MZIs or arrayed waveguide gratings, and these are also called moving average (MA) filters. The IIR filter is composed by feedback loops such as ring resonators, and are also called autoregression (AR) filters. The Autoregressive (AR) filter has only poles and is composed by multiple feedback delay lines. Filters with both poles and zeros are thus called Autoregressive Moving Average (ARMA) filters. An Infinite Impulse Response (IIR) filter has at least one pole.

2.4   Different filter implementations

There are different optical filter implementations.

2.4.1   Directional coupler

The Z-transform relationships of basic optical circuit elements were first developed for fiber optic filters by Moslehi and co-workers []. The waveguide delay and directional coupler are first described using their Z-transforms.
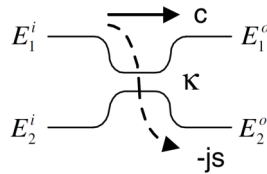
Figure 2.6: Transmission coefficients for the through- and cross-ports of an optical directional coupler [5]

A power coupling ratio,κ, is associated with each directional coupler. The coupling ratio is determined by the length of region where the two waveguides are coupled. The relationship between the input electric fields and output electric fields are expressed as a 2×2 transfer matrix in Eq.

$$\begin{bmatrix} E_{out1} \\ E_{out2} \end{bmatrix} = \begin{bmatrix} c & -js \\ -js & c \end{bmatrix} \begin{bmatrix} E_{in1} \\ E_{in2} \end{bmatrix} \tag{2.9}$$

2.4.2 A single-stage MA filter

A fundamental building block of photonic integrated circuits is the Mach-Zehnder interferometer (MZI). It is a four port device and consists of two couplers and a delay section composed by two waveguides with length L_1 and L_2. This device could be made tunable with a phase shifter on one waveguide of it, inducing a ϕ phase shift. The unit delay is defined by the length difference between the two waveguides. The transfer function of the unit delay is z^{-1}. The schematic of a single MZI is given in Fig. 2.7. A 2×2 delay matrix is written for both arms as follows:

$$\Phi_{delay} = \gamma e^{-j\beta L_2} \begin{bmatrix} z^{-1} & 0 \\ 0 & 1 \end{bmatrix} \tag{2.10}$$

The transfer matrix for a single phase shifter is given as :

$$\Phi_{ps} = \begin{bmatrix} e^{-j\phi} & 0 \\ 0 & 1 \end{bmatrix} \tag{2.11}$$
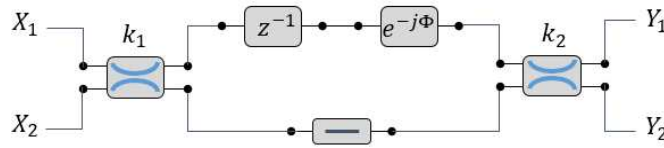
Figure 2.7: A single-stage MZI schematic [6]

where -20$\log_{10} \gamma = \alpha L_2$ is the loss in dB for propagation through the common path length of both arms. The overall transfer matrix for the MZI is the product of the transfer matrix of each component of the MZI in Eq. 2.12:

$$
\begin{aligned}
\Phi_{MZI} &= \Phi_{cplr}(\kappa_2)\Phi_{delay}\Phi_{ps}\Phi_{cplr}(\kappa_1) \\
&= \gamma \begin{bmatrix} c_2 & -js_2 \\ -js_2 & c_2 \end{bmatrix} \begin{bmatrix} e^{-j\phi} & 0 \\ 0 & 1 \end{bmatrix} \begin{bmatrix} z^{-1} & 0 \\ 0 & 1 \end{bmatrix} \begin{bmatrix} c_1 & -js_1 \\ -js_1 & c_1 \end{bmatrix} \\
&= \begin{bmatrix} c_1 c_2 e^{-j\phi} z^{-1} - s_1 s_2 & -j(s_1 c_2 e^{-j\phi} z^{-1} + c_1 s_2) \\ -j(c_1 s_2 e^{-j\phi} z^{-1} + s_1 c_2) & -s_1 s_2 e^{-j\phi} z^{-1} + c_1 c_2 \end{bmatrix}
\end{aligned}
\tag{2.12}
$$

where $s_n = \sqrt{\kappa_n}$ and $c_n = \sqrt{1 - \kappa_n}$.

2.4.2.1 Multi-stage filter

A multi-stage filter can be realized by concatenating MZIs in a lattice architecture as shown in Fig. 2.8. Only N+1 couplers are required for an N-stage filter. The applications include bandpass filters , gain equalization, and dispersion compensation.
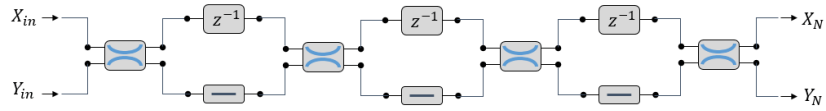
Figure 2.8: multistage lattice filter [6]

2.4.3 A Single-Stage AR Filter

A ring resonator is the simplest optical waveguide filter with a single-pole response.
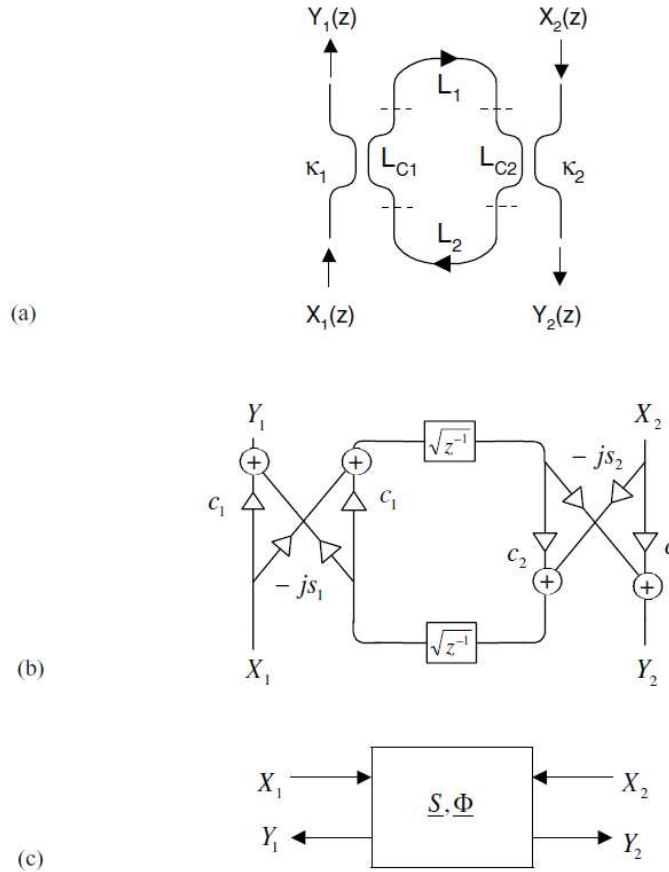
Figure 2.9: Ring resonator with two couplers (a) waveguide layout, (b) Z transform schematic, and (c) matrix representation [6]

$$H_{21}z = \frac{Y_2(z)}{X_1(z)} = \frac{-\sqrt{(\kappa_1 \kappa_2 \gamma z^{-1})}}{1 - c_1 c_2 \gamma z^{-1}} \qquad (2.13)$$

The FSR of the ring resonator is proportional to the round trip length of the ring resonator, which is $L_{c1} + L_{c2} + L_1 + L_2$ shown in Fig. 2.9(a).

2.4.3.1 Coupled ring resonator
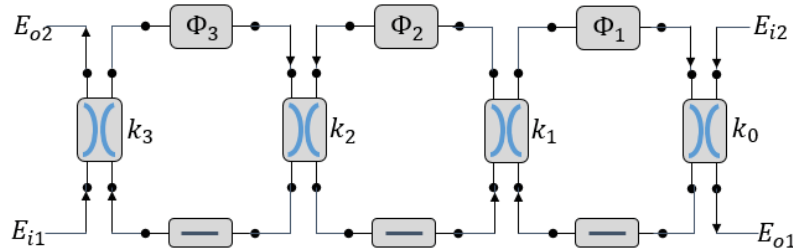
Figure 2.10: AR lattice filter architecture: (a) multi-stage waveguide schematic [6]

The echelle grating and arrayed waveguide grating (AWGs) are essential components in wavelength division multiplexed (WDM) communication networks.

2.4.4 AWGs

The arrayed waveguide gratings (AWG) are widely used in WDM systems, they are used to multiplex wavelengths from a port to multiple ports, thereby the capacity of optical networks is increased considerably.

The light that comes from an input fiber first enters a multimode waveguide section, then the split light propagates through several single-mode waveguides to a second multimode section, and finally into the output ports. The schematic drawing of it is given in Fig. 2.11.

2.4.5 Echelles

The schematic of an echelle grating is given in Fig. 2.12. The light diverges and illuminates the concave grating after entering the slab region of the input waveguide. The diffracted light from the grating is focused into the output waveguides with the help of the concave surface.
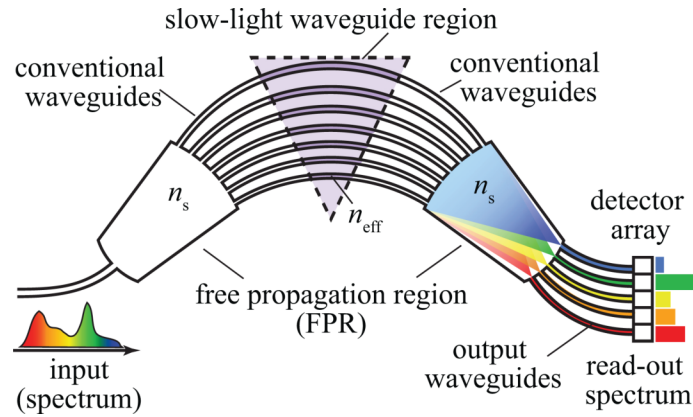
Figure 2.11: Schematic diagram of a slow-light arrayed-waveguide-grating spectrometer [7]
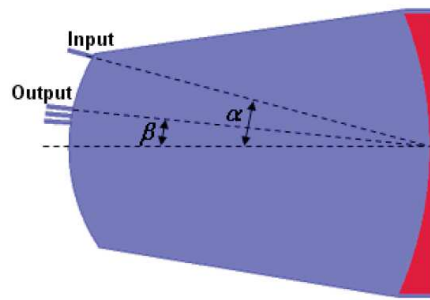
Figure 2.12: Schematic of echelle grating [8]

2.4.6 Other types

Except the above widely used filter designs, there are also other designs proposed by researchers, including nested ring Mach-Zehnder interferometers [9], re-configurable silicon processors based on resonant self-coupled optical waveguides (SCOW) [10], response shaping with a silicon ring resonator via double injection [11], and the cross-ring resonator MZI interleavers [12].

2.4.7 Application of filters

Microwave notch filters with high peak rejection have been widely studied. These microwave notch filters are crucial for removing interference in dynamic, wideband radio systems, such as cognitive or ultrawideband (UWB) radios. The specs for such applications are demanding, including high resolution filtering (3-dB

width of a few tens of MHz) with a very high notch peak rejection (>50 dB) [13]. For a ring notch filter, the critical coupling is achieved when the coupling is equal to the loss (r = a).

Integrated quantum photonics have attracted much attention in recent years for its potential to implement large-scale quantum information processing circuits on the mature platforms of photonic integrated circuits, including programmable quantum chip in Xanadu, which severs as online 8 or 12 qubits quantum cloud sever. The practical realization of a quantum system would require generation, manipulation and detection of the correlated single photons on a single chip. The entangled photon pairs are generated by the spontaneous four-wave mixing (SFWM) process, which uses the x^3 nonlinearity of the silicon excited by a strong pump field. A high extinction ratio or suppression ratio filter of 100 dB while no additional loss is needed as pump rejection filter to the biphoton quantum states generated by the SFWM. Several solutions have been proposed to solve this problem, including cascaded Bragg waveguide grating filters and cascaded second-order coupled-resonator optical waveguide (CROW) [14]. The design for the cascaded crow filter is quite simple, the heaters on the rings are used to calibrate the resonance shift induced by fabrication variation. The performance of such filter is quite good, the extinction ratio of a single stage is around 50 dB, the two stage combined could reach an extinction ratio of 96 dB. The reported insertion loss is 0.8 dB , which is the lower-est one compared with former filter demonstration.

2.5   Conclusion

In this chapter, the mathematical representation of a digital filter and its physical meaning is introduced to the reader through the example of a AWG. Some basics of digital filter design and three filter types have also been introduced.

References

[1]

[2] Bjorn Gustavsen and Adam Semlyen. *Rational approximation of frequency domain responses by vector fitting*. IEEE Transactions on power delivery, 14(3):1052–1061, 1999.

[3] Alan V Oppenheim and Ronald W Schafer. *Digital signal processing(Book)*. Research supported by the Massachusetts Institute of Technology, Bell Telephone Laboratories, and Guggenheim Foundation. Englewood Cliffs, N. J., Prentice-Hall, Inc., 1975. 598 p, 1975.

[4] Ronald Newbold Bracewell and Ronald N Bracewell. *The Fourier transform and its applications*, volume 31999. McGraw-Hill New York, 1986.

[5] *Introduction*, chapter 1, pages 1–17. John Wiley Sons, Ltd, 1999.

[6] Christi K Madsen and Jian H Zhao. *Optical filter design and analysis*. 1999.

[7] Zhimin Shi and Robert W. Boyd. *Fundamental limits to slow-light arrayed-waveguide-grating spectrometers*. Opt. Express, 21(6):7793–7798, Mar 2013.

[8] Dazeng Feng, Ning-Ning Feng, Cheng-Chih Kung, Hong Liang, Wei Qian, Joan Fong, B. Jonathan Luff, and Mehdi Asghari. *Compact single-chip VMUX/DEMUX on the silicon-on-insulator platform*. Opt. Express, 19(7):6125–6130, Mar 2011.

[9] S. Darmawan, Y. M. Landobasa, and M. K. Chin. *Nested ring Mach-Zehnder interferometer*. Opt. Express, 15(2):437–448, Jan 2007.

[10] Liangjun Lu, Lin Shen, Wei Gao, Linjie Zhou, and Jianping Chen. *Reconfigurable Silicon Photonic Processor Based on SCOW Resonant Structures*. IEEE Photonics Journal, 11(6):1–12, 2019.

[11] Amrani O. Ruschin S. Cohen, R.A. *Response shaping with a silicon ring resonator via double injection*. Nature Photon, 12:706–712, 2018.

[12] Junfeng Song, H. Zhao, Q. Fang, S. H. Tao, T. Y. Liow, M. B. Yu, G. Q. Lo, and D. L. Kwong. *Effective thermo-optical enhanced cross-ring resonator MZI interleavers on SOI*. Opt. Express, 16(26):21476–21482, Dec 2008.

[13] David Marpaung, Blair Morrison, Ravi Pant, Chris Roeloffzen, Arne Leinse, Marcel Hoekman, Rene Heideman, and Benjamin J. Eggleton. *Si3N4 ring resonator-based microwave photonic notch filter with an ultrahigh peak rejection*. Opt. Express, 21(20):23286–23294, Oct 2013.

[14] Rakesh Ranjan Kumar and Hon Ki Tsang. *High-extinction CROW filters for scalable quantum photonics*. Opt. Lett., 46(1):134–137, Jan 2021.

3

A 2×2 broadband waveguide coupler

In wavelength circuits, there are many points where the light needs to be split, often with well controlled fractions that are constant over a wide wavelength range. The most common case is a 50:50 couplers, where the imbalance is the most critical parameter.

Such coupler acts as a poser distribution, but also as an optical beam 2×2 beam coupler [1] [2] for interference-based devices, both for splitting, mixing and combining.

3.1 State of the art

The 2×2 broadband waveguide coupler can be made by several approaches.

The directional coupler is the most common way to implement a waveguide coupler due to the ease of fabrication. The coupling of it could be easily controlled through the engineering of the lupmped part and dependent part, however it is very dispersive in high-contrast materials like silicon [3]. Also the directional coupler is quite sensitive to fabrication variations due to the narrow coupling gap. The working principle of the directional coupler is based on the interference effect of two modes, which means no fundamental loss in the coupler apart from scattering and absorption losses. Directional couplers which have been engineered to have a broadband response are usually designed for a fixed splitting ratio (e.g. 50:50) [2].

Multimode interference (MMI) couplers, with their relatively large bandwidth and relaxed fabrication tolerances [4] [5], have been widely used as splitters, but

it is hard to engineer for arbitrary coupling ratios, and it is not easily tunable. The working principle of a MMI is self-imaging: the light from the input port is coupled to multiple modes, and then interferenced and coupled back to the two waveguides. It is more broadband however it is limited by the coupling ratios that can be achieved since coupling to multiple modes also makes it hard to get all the light back into the two waveguide modes.

One implementation of such broadband coupler is by using use asymmetric-waveguide based phase control sections [2]. It is a Mach-Zehender interferometer (MZI) based couplers which integrate an MZI structure into either DCs or multimode-interferometers, which exhibits broadband performance but with a large footprint on the scale of hundreds of micrometers,

Adiabatic couplers are often implemented as a broadband splitter. They are not able to function in two directions, besides, they are also very long [6]. The coupling region of an adiabatic 3 dB coupler typically needed to be a few hundred micrometers long.

Sub-wavelength grating (SWG) structures offer the flexibility to tailor the refractive index and the dispersion properties of SOI photonic devices and, thus, provide a means to reduce the device footprint. SOI sub-wavelength grating (SWG) structures can be used to further reduce the footprints of adiabatic 3 dB couplers [7].

There is also generalized directional coupler, where the cross section of the design is varying.

The broadband coupler is widely used in applications in communication system such as switches [8] and interleaver [9]. Tne method of realizing a broadband coupler in this thesis is by using a Mach-Zehnder interferometer (MZI) type coupler. Part of this work was performed in the context of the Master thesis of Xuhao Wu, which I supervised. The theoretical analysis of it is performed with a model built with EME (Eigen mode expension) method in FIMMPROP [10]. The design was further optimized with the Kriging method.

3.2   Component model for broadband coupler

The optical model for the broadband coupler is built with the FIMMPROP with the EME method. One implementation of such broadband coupler is by using the MZI shown in Fig. 3.1. It is composed of 3 sub-components, symmetrical coupler, taper and phase compensation section [2]. In theory, the modes in the two waveguides of the phase compensation section do not couple with each other. However, such design has been investigated in simulation, and the weak coupling in the taper and phase compensation section is not negligible. Thus, we will choose a variation design shown in Fig. 3.2. Our design separates the two waveguides used in the phase compensation section by a s-bend.
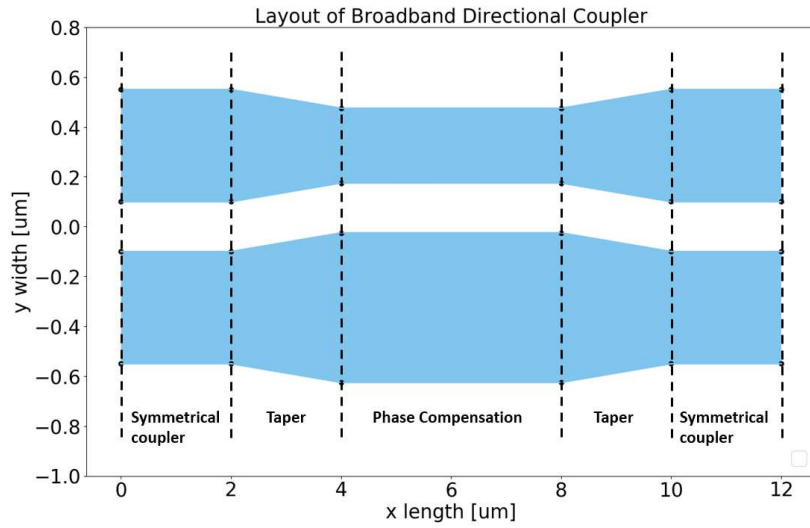
Figure 3.1: The layout of the broadband directional coupler implemented by a MZI
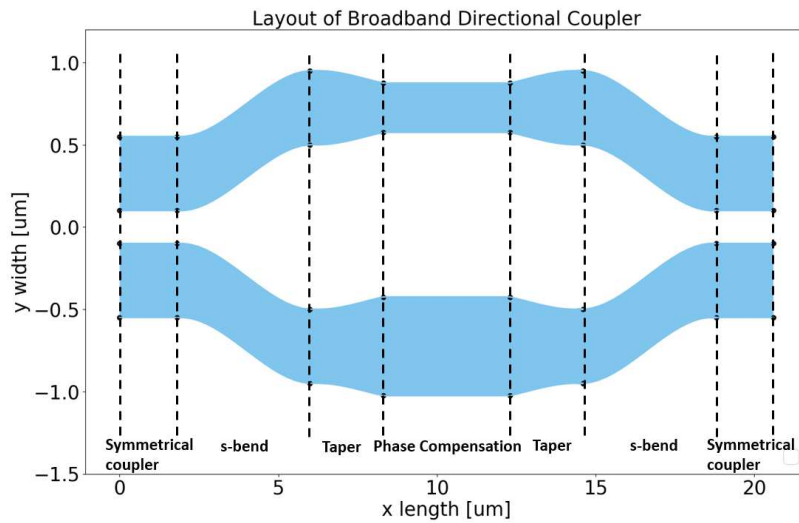
Figure 3.2: The variation design of the broadband directional coupler, the s-bend separates the two waveguides of the phase compensation section apart.

3.2.1 Model building

In this section, we will build the model in FIMMPROP step by step.

First, the layout of the broadband coupler is defined with few control points shown in Fig. 3.3. The width of the waveguide in the input and output coupler is defined to be 0.5 um, the gap of the input and output coupler is defined as 0.2 um. The S-bend is first defined as straight section, however in the real fabrication, a smooth shape is more favorable because the abrupt change in the s-bend or taper-like sections would induce reflections. Thus, in the next step, we will interpolate the s-bend and taper section into more smooth curve. The interpolation method is called scipy.interpolate.CubicSpline [11].The bend shape is defined according to the length and height of the bend. The coupling of the bend can not be ignored, besides the shape of bend could also cause loss to the whole design, thus, the height of the bend could be set as a parameter to be optimized. The widths for the phase compensation sections are 0.3 um and 0.6 um separately. The length of the taper is set to be 1.5 um, the length of the bend is set to be 4 um at the moment. For simplicity, our first optimization only takes the length of the input and output directional coupler and the phase compensation section as two variables to be optimized. The layout before interpolation could be plotted in Fig. 3.3.
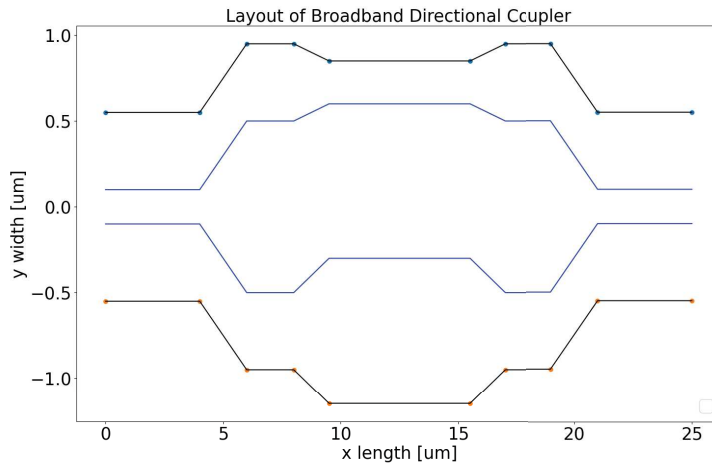
Figure 3.3: The layout of the broadband directional coupler

The layout of the directional coupler after interpolation is shown in Fig. 3.4. The number of slices used in the s-bend and taper section is currently defined to be 20, the convergence test needs to be done in order to determine the proper number of slices for the bend and taper section.

The FIMMPROP is controlled by pyFimm [12], which is an open-source python interface of Photon Design's FIMMWAVE/FIMMPROP. In the next step, we will use pyFimm to construct the same design as shown in Fig. 3.4. The design is
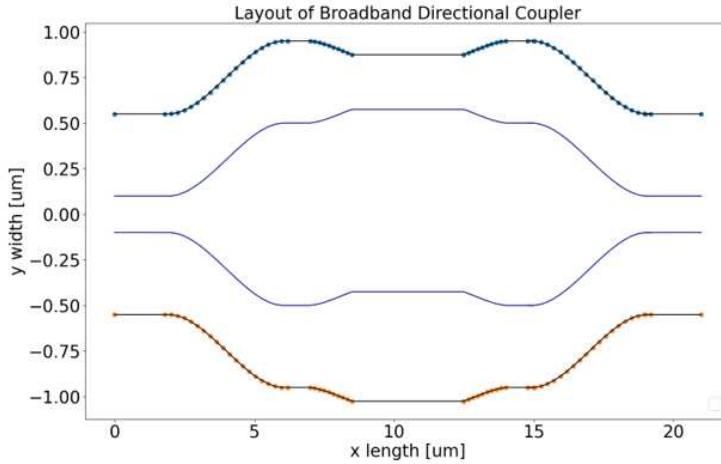
Figure 3.4: The layout of the broadband directional coupler, it is obtained by interpolating the initial design in Fig. 3.3

calculated with the EME method, for which the geometry is discretized into sections. For each individual section, FMM or FDM is used to calculate the supported modes. The taper and S-bend contain 20 sections to be calculated. In this model, the bend and taper section are fixed, thus it needs to be calculated only once. So the coupler length and phase section length can be very efficiently swept. The directional model generated by FIMMPROP is shown in Fig. 3.5. The model built by FIMMPROP would be rigorous, thus, we could also capture the coupling and phase induced in the s-bend and taper section. In the next section, we will use the Kriging algorithm to optimize our design.

3.3   Component optimization with Kriging

As we have discussed before, the broadband directional coupler is a Mach-Zehnder shaped design. It is composed of two input and output directional coupler sections, two s-bends, two taper sections and a phase compensation section. The phase compensation is composed by two waveguides of different width, so that the propagation constant for the light in these two waveguides is different, thus a phase difference between light in the upper and lower arms is induced. If the input and output coupler are 50/50 direcitonal couplers, then the phase difference in the upper and lower arm of such design would determine the splitting ratio in the output ports.

If we make the design shown in Fig. 3.2 symmetric along the propagation
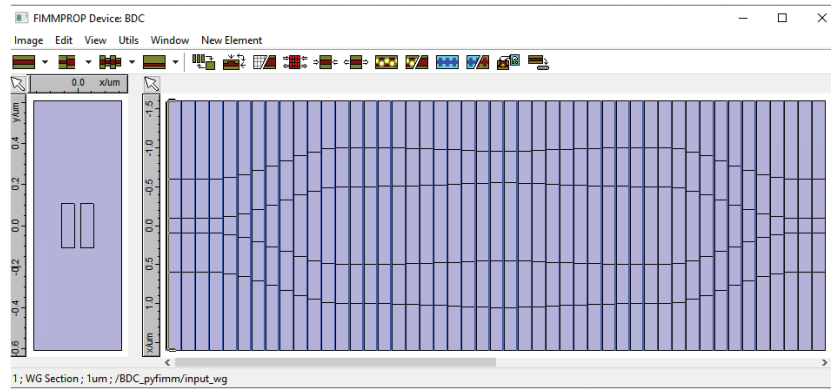
Figure 3.5: The directional coupler generated by FIMMPROP

direction (i.e. input section and output section are identical), then only two parameters need to be changed in the optimization process, which is the length of the input and output directional coupler and the length of the phase compensation section. The other parameters such as the length of the s-bend and the taper section are fixed in each simulation. In FIMMPROP model, the input and output coupler section is modeled as one slice, the phase compensation section is modeled as another slice, while the s-bend and taper section is modeled as many slices, the width in sub-slice is the same, and the height of each sub-slice is determined by the interpolation function.

Before the optimization, parameter sweeping is needed to be able to define the reasonable range for optimization. We could plot the output coupling as a function of the length of coupler and phase compensation section, this serves as a look-up table for the next optimization step.

Normally the only reliable simulation technique to a fully vectorial, 3D solution of Mxwell's equations is EME or FDTD. The optimization process for a photonic component can be very expensive, thus it is important to keep the number of these 'expensive' simulation as small as possible.

The Kriging method is developed by Daniel G. Krige for the distribution of gold mines. Kriging is a surrogate model based on Gaussian process regression. Its capability to predict multidimensional and nonlinear responses from scattered data gives it growing popularity.

Kriging could be used to reduce the number of simulations by adaptively selecting the simulation point with the largest likelyhood of producing a better component. However, individual simulations are still expensive. Thus, a combination of expensive, high-precision 3D FDTD simulations with much cheaper, lower-precision 2D EME simulations can accelerate the optimization. Such technique is called Co-Kriging, it uses the cheap simulations to learn the trends of the compo-
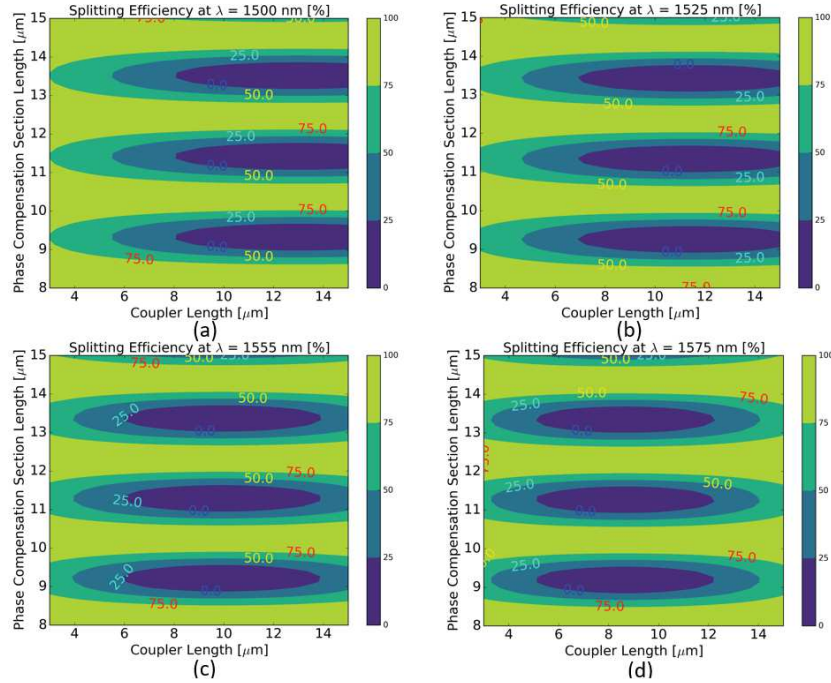
Figure 3.6: The length of the coupler and phase compensation section are swept for wavelengths at 1500, 1525, 1555, and 1575 nm. The contour plot of the coupling values are plotted.

nent behavior, which are calibrated with expensive simulations. The cheap simulations allow a quick building of the landscape of multi-dimensional parameter space, which minimized the need of the expensive simulations. The Co-Kriging has been used to optimize the $1 \times 2 splitter design 1001$[13].

In the optimization of broadband directional coupler in this thesis, Kriging has been used as the optimization algorithm and the 3D FDTD is only used in the final verification step.

The overall procedure for Kriging optimization could be described as:

1. The target function is defined. In the BDC design, the coupling power ratio $P_{coupling-ratio}$ defined in Equation (3.1) is used as the target function for the broadband operation.

2. The initial status has been provided. In the BDC optimization, we could get the initial status by a parameter sweep.

3. In our simulation, the model built with Fimmprop could be called as cheap model, and the FDTD model built with Lumerical FDTD could be called

expensive model. The definition of cheap and expensive model is based on the simulation time it used. The Kriging simulation could be based on pure cheap model, Co-Kriging is used to combine cheap and expensive model in one single optimization. In this particular case for broadband directional coupler optimization, we only use the cheap model built with EME for component optimization.

$$P_{\text{coupling-ratio}} = \frac{P_{o1}}{P_{o1} + P_{o2}} \tag{3.1}$$

where P_{o1} is the output power of the upper port and P_{o2} is that of the lower port. Note that both P_{o1} and P_{o2} should be normalized.

In this thesis, the ooDACE [14] toolbox developed by the SUMO group of IDlab at Ghent University - IMEC is used for the Kriging optimization. The algorithm will first sample the parameter space based on the initial condition and boundary conditions. After the initial sampling process, the data points will be collected. The Kriging optimization then uses the collected data points to predict or calculate the rest optimization. The Kriging optimization is time consuming because it builds a model where it has to calculate the uncertainties.

3.4 Results after Optimization

By using the optimization method Kriging, we have optimized the following coupling values. The detailed design information for optimized designs are given in Table 3.1:

We have found the design parameters for the coupling values of 0.2, 0.3, 0.4, 0.5, 0.6, 0.7, 0.8 and 0.9. The dispersion is larger in the broadband design with small coupling values. As we could see from Table A.3, the length of the input and output coupler changes quite a lot for different designs, however the length of the phase compensation section kept similar. The optimized data as a function of coupling is plotted in Fig. **??**.The optimized parameter of coupling 0.8 is an outlier, the rest of the data falls on a smooth curve, which can be interpolated for intermediate coupling values.

The corresponding spectrum response for selected designs in Table 3.1is plotted Fig. 3.8. We are optimizing for 100 nm wavelength range.

The result from the FIMMPROP is then verified with the FDTD simulation. After verification, We could then use e-beam to fabricate this device and compare the measurement result with simulation.

The design workflow is given in Fig. 3.9.

target coupling value	simulation result	deviation	design parameters
$k = 0.2$	$k = 0.1930$	$\delta = 0.0630$	$L_1 = 14.2um$
			$L_2 = 8.33um$
$k = 0.3$	$k = 0.302$	$\delta = 0.04$	$L_1 = 12.5787um$
			$L_2 = 8.470um$
$k = 0.4$	$k = 0.3910$	$\delta = 0.0456$	$L_1 = 11.6205um$
			$L_2 = 8.575um$
$k = 0.5$	$k = 0.508$	$\delta = 0.0363$	$L_1 = 9.905um$
			$L_2 = 8.646um$
$k = 0.6$	$k = 0.598$	$\delta = 0.02193$	$L_1 = 8.789um$
			$L_2 = 8.734um$
$k = 0.7$	$k = 0.724$	$\delta = 0.0162$	$L_1 = 7.234um$
			$L_2 = 8.793um$
$k = 0.8$	$k = 0.793$	$\delta = 0.028$	$L_1 = 7.590um$
			$L_2 = 8.81um$
$k = 0.9$	$k = 0.9$	$\delta = 0.0173$	$L_1 = 3.079um$
			$L_2 = 8.958um$

Table 3.1: design info of the optimized design
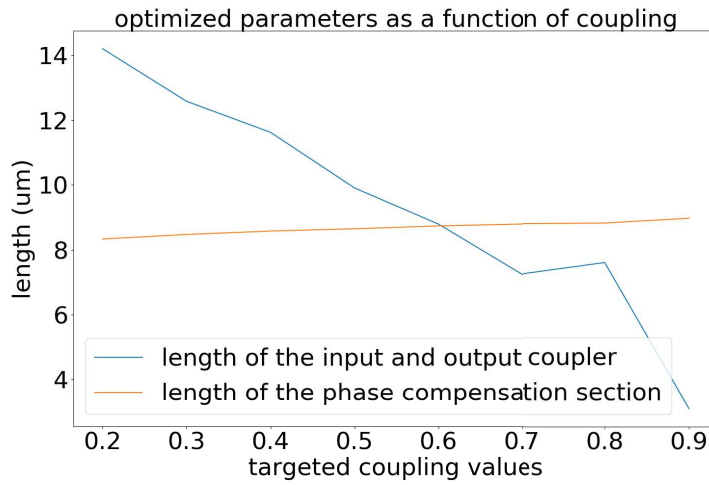
Figure 3.7: This figure is plotted based on Table 3.1. The optimized parameters are plotted as a function of coupling. The optimized parameter of coupling 0.8 is an outlier, the rest of the data falls on smooth curve, which can be interpolated for intermediate coupling values.

3.5   Discussion

The optimized result in Fig. 3.8 showed that designs of larger coupling values are less dispersive than designs with smaller coupling values. Besides, the variation
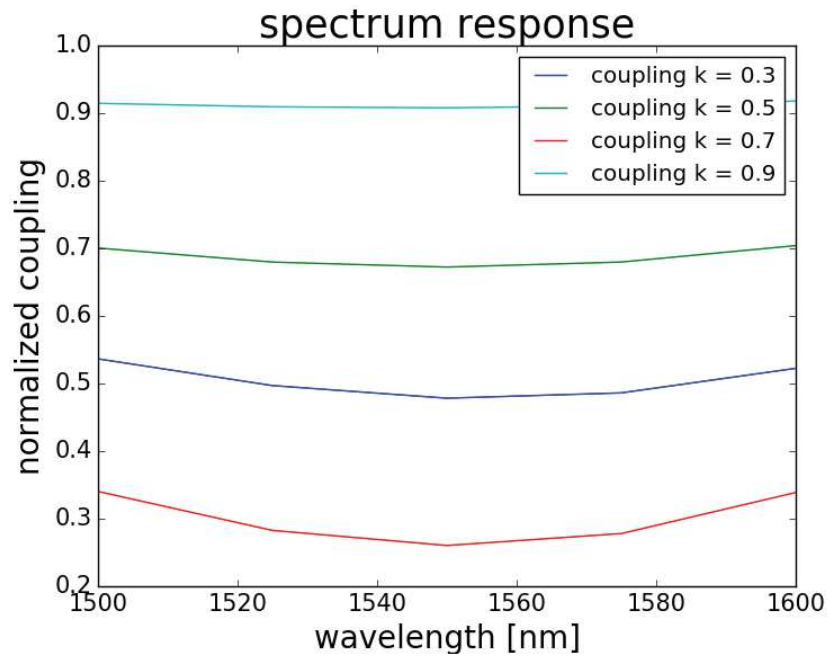
Figure 3.8: broadband spectrum response for selected designs
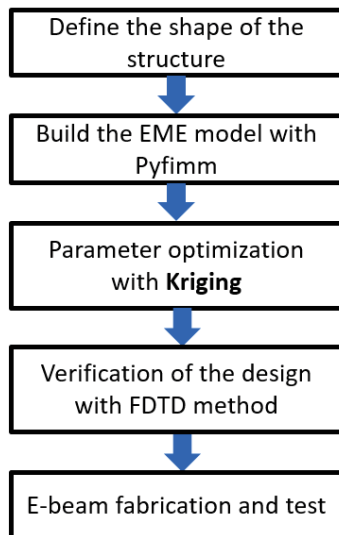
Figure 3.9: design workflow of a broadband directional coupler

of coupling values for a certain design in 100 nm wavelength range is more than 3%.

In order to improve the broadband design, we have the following potential directions to work with.

a. The optimized result shown in Fig. 3.8 is our initial optimization result given only two parameters (length of the coupler and length of the phase compensation section) are optimized. The structure for optimization is limited to a symmetrical shape. We could use a asymmetric structure and the optimization parameters would be increased to three (the length of the input coupler, the length of the output coupler and the length of the phase compensation section), which would provide more freedom for the optimization. b. Other parameters such as gap of input and output coupler, the height of the s-bend, and the widths of the waveguides in the phase compensation section could be varied and also these parameters could be optimized.

c. We could choose a cascaded MZI design for our broadband coupler design. Research has been done on such a cascaded MZI [2] [15]. The device would be bit longer than single-stage MZI design, however the spectrum response would be more broadband. The schematic drawing of such a cascaded MZI is given in Fig. 3.10. Maximum power deviation between theoretical and simulation results for 30%/70% coupler is less than 2%, and FDTD simulated ±2% bandwidth over 1275–1570 nm, in reasonable agreement with the TMM calculation [15].
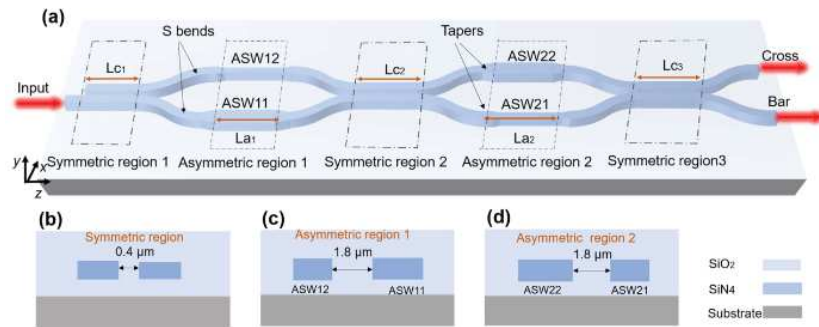
Figure 3.10: Structure of the multi-segment directional coupler. (a) Schematic. (b) Cross section of the symmetric regions. (c) Cross section of the asymmetric region 1. (d) Cross section of the asymmetric region 2 [15]

3.6 Conclusion

In this section, we have shown the whole work flow of a device optimization and fabrication. We have investigated the design and optimization of the broadband di-

rectional coupler (BDC) by Eigenmode expansion method. The proposed structure realized broadband response of coupling values from 0.2 to 0.8, and we have interpolated the result so that we could have design for arbitrary values. The proposed design could be further optimized by using double stage MZI design.

References

[1] DanXia Xu, Adam Densmore, Philip Waldron, Jean Lapointe, Edith Post, André Delâge, S. Janz, Pavel Cheben, Jens Schmid, and Boris Lamontagne. *High bandwidth SOI photonic wire ring resonators using MMI couplers*. Optics express, 15:3149–55, 04 2007.

[2] Zeqin Lu, Han Yun, Yun Wang, Zhitian Chen, Fan Zhang, Nicolas A. F. Jaeger, and Lukas Chrostowski. *Broadband silicon photonic directional coupler using asymmetric-waveguide based phase control*. Opt. Express, 23(3):3795–3808, Feb 2015.

[3] Zeqin Lu, Jaspreet Jhoja, Jackson Klein, Xu Wang, Amy Liu, Jonas Flueckiger, James Pond, and Lukas Chrostowski. *Performance prediction for silicon photonics integrated circuits with layout-dependent correlated manufacturing variability*. Optics express, 25(9):9712–9733, 2017.

[4] Dan-Xia Xu, Adam Densmore, Philip Waldron, Jean Lapointe, Edith Post, André Delâge, Siegfried Janz, Pavel Cheben, Jens H. Schmid, and Boris Lamontagne. *High bandwidth SOI photonic wire ring resonators using MMI couplers*. Opt. Express, 15(6):3149–3155, Mar 2007.

[5] Álvaro Rosa, Ana Gutiérrez, Antoine Brimont, Amadeu Griol, and Pablo Sanchis. *High performace silicon 2x2 optical switch based on a thermo-optically tunable multimode interference coupler and efficient electrodes*. Opt. Express, 24(1):191–198, Jan 2016.

[6] Jiejiang Xing, Kang Xiong, Hao Xu, Zhiyong Li, Xi Xiao, Jinzhong Yu, and Yude Yu. *Silicon-on-insulator-based adiabatic splitter with simultaneous tapering of velocity and coupling*. Opt. Lett., 38(13):2221–2223, Jul 2013.

[7] Han Yun, Lukas Chrostowski, and Nicolas A. F. Jaeger. *Ultra-broadband 2×2 adiabatic 3dB coupler using subwavelength-grating-assisted silicon-on-insulator strip waveguides*. Opt. Lett., 43(8):1935–1938, Apr 2018.

[8] Rubana Bahar Priti, Fei Lou, and Odile Liboiron-Ladouceur. *A high extinction ratio broadband 1310nm MZI switch*. In 2015 IEEE 12th International Conference on Group IV Photonics (GFP), pages 114–115, 2015.

[9] Anthony Rizzo, Qixiang Cheng, Stuart Daudlin, and Keren Bergman. *Ultra-Broadband Interleaver for Extreme Wavelength Scaling in Silicon Photonic Links*. IEEE Photonics Technology Letters, 33(1):55–58, 2021.

[10] Photon Design. *FIMMPROP*. 2018. User manual for program FIMMPROP.

[11] Scipy Org. *scipy.interpolate.CubicSpline*.

[12] Demis D. John. *PyFIMM: Python Interface to PhotonDesign's FimmWave/-FimmProp software*.

[13] P Wahl, Ivo Couckuyt, Christian Kremers, Frank Demming, Tom Dhaene, and Wim Bogaerts. *Optimization of silicon photonic components using multi-fidelity simulations and co-kriging*. In 24th International Workshop on Optical Wave & Waveguide Theory and Numerical Modelling (OWTNM 2016), 2016.

[14] Ivo Couckuyt, Tom Dhaene, and Piet Demeester. *ooDACE toolbox, a Matlab Kriging toolbox: Getting started*. 2013. User manual for program ooDACE toolbox.

[15] Lemeng Leng, Minfeng Jin, Zhongzhi Lin, Chenbin Zhang, Ding Ding, and Wei Jiang. *Ultra-Broadband, Fabrication Tolerant Optical Coupler for Arbitrary Splitting Ratio Using Particle Swarm Optimization Algorithm*. IEEE Photonics Journal, 12(5):1–12, 2020.

4

Broadband Coupler Circuit Design

Programmable / configurable circuits need a broadband 2x2 coupler that can be adjusted at run time, to tune between 0% and 100%. So the static component from the previous chapter needs to be made electrically tunable while at the same time main the broadband response. This work was collaborated with a former colleague Antonio Ribeiro.

We propose a circuit design for a broadband tunable 2×2 waveguide coupler, consisting of a two-stage Mach-Zehnder interferometer with electro-optic phase shifters in each stage. We demonstrate that such design can be configured as a tunable coupler with arbitrary coupling ratio and with a uniform response over 50-nm spectral range around 1550 nm. The design is also tolerant to fabrication variations that affect the coupling ratios of the directional couplers.

4.1   State of the art

One of the essential building blocks for these optical circuits is a 2×2 waveguide coupler, the integrated equivalent of an optical beam splitter. Such component is essential for power distribution as well as the construction of interferometric wavelength filters [1].

It is preferable that these couplers have a broadband response, especially for applications such as linear transformations, switch fabrics or bandpass filters. Also, tunability is another property that is highly desireable, as it can make photonic circuits more flexible, up to the point where we can make programmable photonic

circuits where many waveguides are connected in a mesh with tunable 2×2 couplers [2].

Normally, a tunable coupler made with single-stage Mach-Zehnder interferometer (MZI) would require an ideal 50:50 splitters/combiners to achieve 0-100% splitting ratio [3]. However, due to fabrication variation, the fabricated device (e.g. 50:50 splitters/combiners) will deviate from the designed value, and this will limit the coupling range that can be addressed with the MZI circuit. Also, as the directional couplers are wavelength dependent, the coupling of the MZI circuit will also be wavelength dependent.

Therefore, a fabrication-tolerant 2×2 coupler circuit, that can be tuned from 0 to 100% coupling, and this over a wide wavelength range, is a highly needed building block to construct complex circuits.

In order to address this issue, Miller has proposed a three-stage MZI circuit, which we could also call a $2 \times 2 \times 2 \times 2$ MZI design [3]. This can be seen as a regular single-stage 2×2 MZI where the two directional couplers (splitter and combiner) have been replaced by a tunable 2×2 MZI circuit, thereby guaranteeing that a 50:50 coupling can be obtained in both the splitter and combiner. Suzuki has also proposed a reduced two-stage design (a $2 \times 2 \times 2$ MZI) [4], however neither of these designs address the issue of wavelength dependence.

The dual-drive directional coupler proposed by Daniel [5] has lower insertion loss. However the power consumption of the design is still significantly high. And the optimization of the thermally tuned dual-drive DC is constrained by fabrication limitations that set minimum distances between metal layers and waveguide layers, among waveguide layers and safety distances for isolation trenches. It is not very clear whether or how this device could reduce its power consumption. Besides, the reported operation bandwidth of the dual-drive DC is just around 12 nm.

4.2   Tolerant tunable 2×2 coupler

In this chapter, we are building on the two-stage $2 \times 2 \times 2$ MZI design and explore its use and configuration for a broadband coupling response. As we will show, optimizing the device performance is as much about the control as well as about the device design itself. This chapter is organized as follows. Section 4.2 explains the basic principle and tolerance of the design, while section 4.3 presents an underlying theoretical description. Section 4.4 and section 4.5 present the simulation and experimental results. The real-time optimization algorithm is explained in section 4.6. Section 4.7 concludes the chapter. Most of this chapter is based on the results published in [6].

Due to fabrication variations, a fabricated device will always deviate from its designed performance. For example, a 50:50 2×2 coupler, either implemented as a directional coupler or a multimode interferometer, can easily suffer from a few

percent points of coupling variation from the ideal 50:50 splitting ratio at 1550 nm. Thus, tolerant designs that compensate for these variations in the optical circuits are very much desired, but not easily implemented.

The typical implementation for a tunable coupler is a balanced MZI. The MZI is constructed with two static 50:50 couplers such as directional couplers (DCs), connected with two waveguides with integrated phase shifters (e.g. heaters). The power transmissions in both outputs ('bar' and 'cross') cover the whole range of 0% to 100% only when the splitter and combiner have a perfect 3dB (50:50) splitting ratio. When the coupling ratio of the directional couplers deviates from its designed value, the power coupling range in 'cross' will not go all the way to 100%, and the bar transmission can not be suppressed all the way down to 0%.

And as already mentioned, even if the directional couplers have a perfect 50:50 splitting ratio, this is usually only the case for a narrow wavelength range, as the directional couplers are wavelength dependent. Alternative couplers, such as MMIs [7] and phase-compensated directional couplers [8] offer a more broadband 50:50 coupler, but these can also suffer from deviations due to fabrication variability.
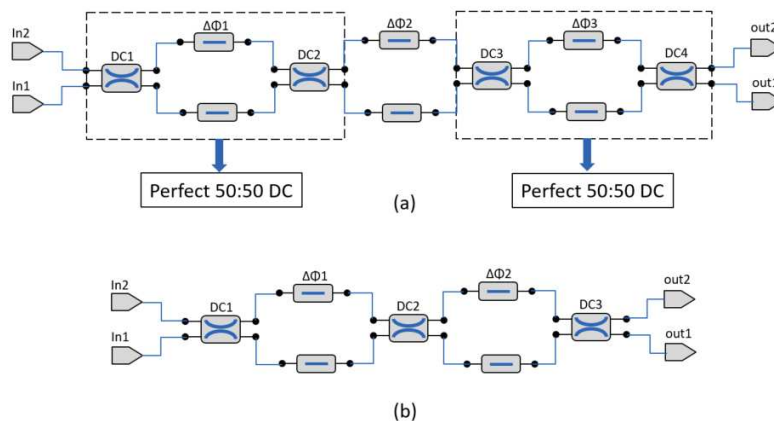
Figure 4.1: (a) Three-stage design for the tolerant tunable coupler, as proposed by Miller [3]. (b) Circuit schematic of the two-stage broadband tunable coupler [4]. The directional couplers (DCs) are connected with two waveguides with integrated phase shifters (e.g. heaters), which correspond to the phase compensation section $\Delta\phi_1$ and $\Delta\phi_2$.

The accumulation of imperfections caused by fabrication variation would have huge impact on large programmable circuits with hundreds or thousands of tunable couplers, especially on functions that rely on 'cross' coupling with a very high rejection ratio in the 'bar' port. In order to solve this issue, Miller [3] has proposed the following structure as the tolerant design for the tunable coupler. Basically, each directional coupler in the single stage MZI has been replaced with a balanced

MZI, as illustrated in Fig. 4.1a. This results in a circuit with 3 concatenated MZI stages, each with tunable phase delay in the arms. As long as the directional couplers in the design have a coupling ratio between 85:15 to 15:85, the circuit can be tuned to achieve transmission from 0 to 100%. However, such design would require control electronics for at least 3 heaters.

To reduce the control complexity, we propose a similar circuit with only two tunable MZI stages (three directional couplers with two thermal tuners), similar to what has been proposed in [4], as shown in Fig. 4.1b. The coupler circuit can be tuned from 0% to 100% as long as the three directional couplers have a balance that is better than 25:75, which is shown in Fig. 4.2. Compared to the three-stage design, the tuning algorithm becomes simpler while it is still tolerant to fabrication imperfections and even local variability.
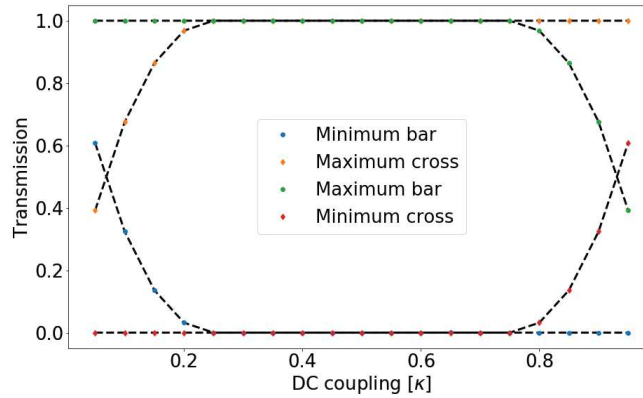
Figure 4.2: Addressable range of the transmission curve for Fig. 4.1b for different values of the DC coupling k. We set the coupling of all DCs k_i to be same, and calculated the minimum and maximum transmission in both bar and cross coupling. We see that, as long as the DCs have coupling values between 0.25 to 0.75, we are able to achieve transmission between 0% and 100%.

4.3 Theoretical analysis

To understand how we can turn the two-stage $2 \times 2 \times 2$ MZI in Fig. 4.1b into a tolerant, but also a broadband tunable coupler, we built a simple analytical model of this circuit, using the transfer matrix method (TMM). The complex amplitudes of the input and output electromagnetic waves have the following relationship between each other:

$$\begin{bmatrix} E_{out1} \\ E_{out2} \end{bmatrix} = C_3 \times P_2 \times C_2 \times P_1 \times C_1 \times \begin{bmatrix} E_{in1} \\ E_{in2} \end{bmatrix} \quad (4.1)$$

where E_{in1} and E_{in2} are the complex amplitudes of the light in the fundamental waveguide modes at the inputs and E_{out1} and E_{out2} represent the same quantities at the outputs for the 2×2 device. Matrix C_i is the coupling matrix of each directional coupler and Matrix P_i is the propagation matrix of a phase delay section (consisting of two parallel waveguides or phase shifters) for the single stage MZI. The coupling matrix, C_i, is given by:

$$C_i = \begin{bmatrix} \sqrt{1 - k_i} & -j\sqrt{k_i} \\ -j\sqrt{k_i} & \sqrt{1 - k_i} \end{bmatrix} \tag{4.2}$$

where k_i is the power cross-coupling coefficient, and $1 - k_i$ is the straight-through coefficient for the directional coupler. Note that the value of k_i can be different for each directional coupler, and it is also wavelength dependent, and sensitive to fabrication variations. For the rest of the derivation, we assume that $k_1 = k_2 = k_3 = k$, but this does not affect the general conclusions.

The propagation matrix P_i of each phase delay section is given by:

$$P_i = \begin{bmatrix} e^{-j\phi_i} & 0 \\ 0 & 1 \end{bmatrix}, \tag{4.3}$$

where we assume no loss, and equal length for waveguide propagation, so the common propagation terms can be ignored.

The final transfer matrix can then be derived as:

$$T_{11} = \sqrt{1 - k}(-k(e^{j\phi_1} + 1)e^{j(\phi_1 + \phi_2)} + (-ke^{j\phi_1} - k + 1)e^{j\phi_1})e^{-j(2\phi_1 + \phi_2)}$$
$$T_{21} = j\sqrt{k}(k - 1)(e^{j\phi_1} + 1)e^{j\phi_1} + (k + (k - 1)e^{j\phi_1})e^{j(\phi_1 + \phi_2)})e^{-j(2\phi_1 + \phi_2)}$$
$$\tag{4.4}$$

T_{11} is the transfer function of the bar port of the $2 \times 2 \times 2$ MZI, while T_{21} is the cross transmission. In order to have the broadband response of the device for a certain coupling ratio k of the tunable couplers, two conditions need to be satisfied:

- The dispersion of the power transmission $\int_{\lambda_1}^{\lambda_2} \dfrac{\partial |T_{11}(\lambda)|^2}{\partial \lambda} d\lambda \to 0$

- $|T_{11}|^2 =$ desired coupling ratio K

We can rewrite the dispersion for the bar port $\dfrac{\partial |T_{11}(\lambda)|^2}{\partial \lambda}$ as:

$$\frac{\partial |T_{11}(\lambda)|^2}{\partial \lambda} = \frac{\partial |T_{11}(k)|^2}{\partial k} \cdot \frac{\partial k(\lambda)}{\partial \lambda} \tag{4.5}$$

We can describe the wavelength dependence of the directional coupler as a Taylor polynomial expansion around the center wavelength λ_0:

$$k(\lambda) = k_0 + k' \cdot (\lambda - \lambda_0) + \frac{k''}{2} \cdot (\lambda - \lambda_0)^2 + ... \tag{4.6}$$

Now the first-order derivative at λ_0 becomes

$$\frac{\partial k(\lambda)}{\partial \lambda} = k' \tag{4.7}$$

k' is the first order derivative of k, and in order to make the tunable coupler as broadband as possible, we could try to reduce k' by engineering the directional coupler to make it less wavelength dependent according to equation 4.5. This requires a physical optimization. Instead, we can choose not to engineer k', but use the phases ϕ_1 and ϕ_2 to compensate for k'. Squaring and deriving (5.12) gives us:

$$
\begin{aligned}
\frac{\partial |T_{11}(k)|^2}{\partial k} = &(1 - 3k^2 + 4k)e^{j\phi_1 + j\phi_2} + (1 - 3k^2 + 4k)e^{-j\phi_1 - j\phi_2} + \\
&(2k - 3k^2)e^{-j\phi_1 + j\phi_2} + (2k - 3k^2)e^{j\phi_1 - j\phi_2} + \\
&(1 - 6k^2 + 6k)e^{j\phi_1} + (1 - 6k^2 + 6k)e^{j\phi_2} + \\
&(1 - 6k^2 + 6k)e^{-j\phi_1} + (1 - 6k^2 + 6k)e^{-j\phi_2}
\end{aligned}
\tag{4.8}
$$

If we use second order polynomials and neglect higher-order terms, the 3dB directional coupler given by Fig. 4.3c could be simplified as $k = k_0 + k' \cdot (\lambda - \lambda_0)$, where the desired power coupling $K = 0.5$ for $\lambda_0 = 1550\ nm$. We find that $k(\lambda_1) = 0.75$ and $k(\lambda_2) = 0.15$ are corresponding coupling ratios of the DC at wavelengths $\lambda_1 = 1525\ nm$ and $\lambda_2 = 1575\ nm$. For the $2 \times 2 \times 2$ MZI with a dispersive 3dB directional coupler in wavelength range $[\lambda_1, \lambda_2]$, the dispersion $\int_{\lambda_1}^{\lambda_2} \frac{\partial |T_{11}(\lambda)|^2}{\partial \lambda} d\lambda$ could be simplified to:

$$
\begin{aligned}
\int_{\lambda_1}^{\lambda_2} \frac{\partial T_{11}(\lambda)^2}{\partial \lambda} d\lambda = &\int_{\lambda_1}^{\lambda_2} \frac{\partial |T_{11}(k)|^2}{\partial k} \cdot \frac{\partial k(\lambda)}{\partial \lambda} d\lambda = \int_{k(\lambda_1)}^{k(\lambda_2)} \frac{\partial |T_{11}(k)|^2}{\partial k} \cdot dk \\
= &((k - k^3 + 2k^2)(e^{j\phi_1 + j\phi_2} + e^{-j\phi_1 - j\phi_2}) + (k^2 - k^3)(e^{-j\phi_1 + j\phi_2} + e^{j\phi_1 - j\phi_2}) + \\
&(k - 2k^3 + 3k^2)(e^{j\phi_1} + e^{j\phi_2} + e^{-j\phi_1} + e^{-j\phi_2}))\big|_{k(\lambda_1)}^{k(\lambda_2)} \\
= &-0.0615(e^{j\phi_1 + j\phi_2} + e^{-j\phi_1 - j\phi_2}) - 0.1215(e^{-j\phi_1 + j\phi_2} + e^{j\phi_1 - j\phi_2}) - \\
&0.183(e^{j\phi_1} + e^{j\phi_2} + e^{-j\phi_1} + e^{-j\phi_2})
\end{aligned}
\tag{4.9}
$$

The basic principle of configuring a two-stage MZI as a broadband coupler is explained in Fig. 4.3. The grey region in Fig. 4.3a is the region with less than 5% dispersion over 50 nm wavelength range in central wavelength 1550 nm according to equation (4.9).

Fig. 4.3b is the coupling plot for the central wavelength $\lambda_0 = 1550\ nm$. The broadband response for different coupling ratios lies in the region which is the combination of grey region in Fig. 4.3a and contour lines of Fig. 4.3b in the 2D
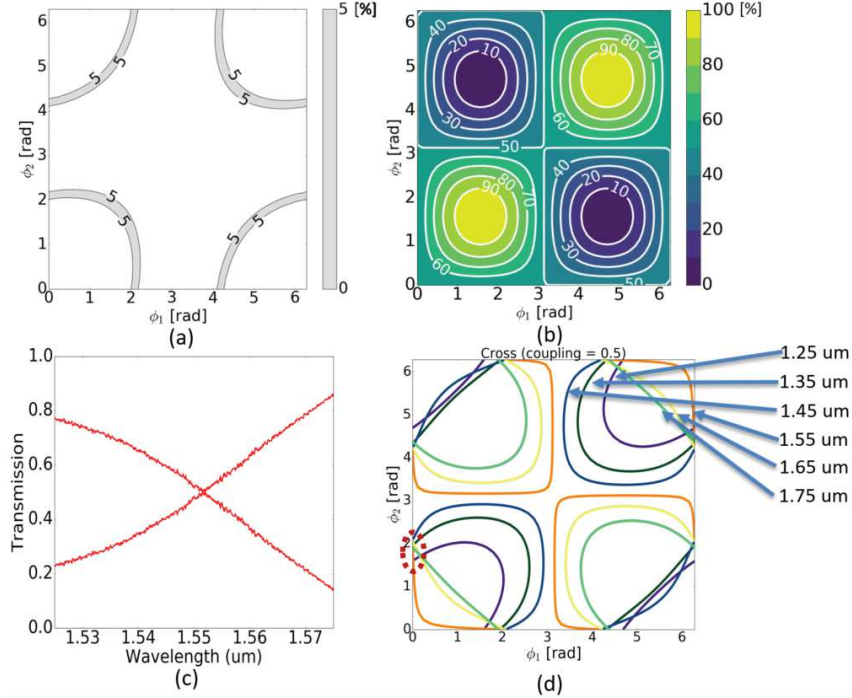
Figure 4.3: (a) Iso-contours for the wavelength dispersion given by equation (4.9), where λ_1 is 1525 nm, λ_2 is 1575 nm. We normalize the absolute value of the dispersion; the grey region indicates settings with less than 5% dispersion. (b) plots the cross transmission at 1550 nm. (c) The spectrum response of a single 50:50 DC used in our fabricated device. (d) The (ϕ_1, ϕ_2) contour to obtain a coupling ratio of 0.5 for different wavelengths has been plotted based on equation (4.8). The region in the 2D phase space indicated by the red dotted line, where the contours for different wavelengths are intersecting, is indicative of a broadband operating regime over a wavelength range of 50 nm.

phase space (ϕ_1 and ϕ_2).Fig. 4.3c is the spectrum response of the 50:50 DC used in our fabricated device. It is clear that the DC only has good 50:50 coupling around $\lambda_0 = 1550\ nm$.The DC is wavelength dependent, and the measured coupling values for different wavelengths are used in the simulation of Fig. 4.3d.

Fig. 4.3d is the simulation result for the same cross coupling points in the 2D phase space of (ϕ_1, ϕ_2). For any coupling ratio, there are a number of phase combinations that will give the correct coupling, which corresponds to the contour lines in Fig. 4.3d. However for different wavelengths, these contours become distorted, because the directional couplers have different coupling strength at other wavelengths. The change in coupling strength can be compensated by the control of the constructive/destructive interference through the two phase shifters.The region in the 2D phase space indicated by the red dotted line, where the contours for dif-
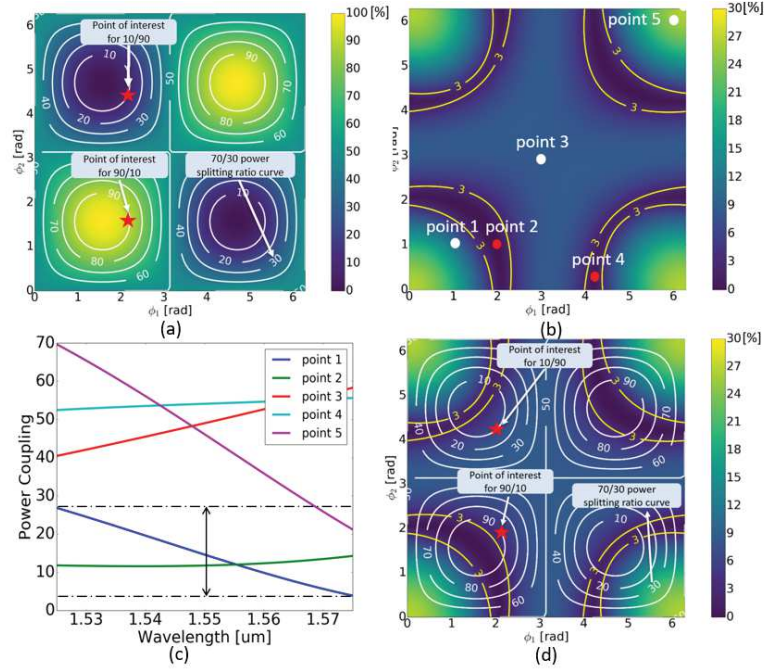
Figure 4.4: Simulations of a two-stage MZI tunable coupler with a directional coupler with a perfect 50:50 splitting ratio at 1550 nm. (a) Cross transmission at a wavelength of 1550 nm, (b) Maximum deviation of the cross coupling between 1525 nm and 1575 nm for the two-stage tunable coupler.(c) Transmission spectra of the corresponding points in (b).(d) Combination of (a) and (b).

ferent wavelengths are intersecting, is indicative of a broadband operating regime over a wavelength range of 50 nm.Essentially, this configuration of (ϕ_1, ϕ_2) results in an region where the contours of different wavelengths intersect or come very close together.

4.4 Tuning for broadband operation

Based on this model, we understand that we can configure the $2 \times 2 \times 2$ MZI as a wavelength-independent tunable coupler, which is very useful for many applications such as wavelength-division multiplexing and signal switching in data communication. However, the coupling ratios of conventional directional couplers are highly sensitive to their operating wavelengths, especially in high-contrast waveguide materials such as silicon. A broadband 2×2 coupler would have the desired response that the coupling ratio remains the same in a larger bandwidth.

Figure 4.4 presents the simulation of a two-stage tunable coupler with direc-

tional couplers with a perfect 50:50 splitting ratio at 1550 nm, the model for 3dB directional coupler has been explained in section 3. Fig. 4.4(a) is the cross transmission at a wavelength of 1550 nm, Fig. 4.4(b) is the maximum deviation of the cross coupling between 1525 nm and 1575 nm for the two-stage tunable coupler. The dark regions bounded by the yellow contours in the graph indicate the region of 3% deviation from the desired coupling within a 50 nm wavelength range around 1550 nm. Fig. 4.4(c) is the transmission spectra of the corresponding points in Fig. 4.4(b): only point 2 and 4 have a flat spectral response, corresponding to the dark region in Fig. 4.4(b). Fig. 4.4(d) is the combination of Fig. 4.4(a) and Fig. 4.4(b): the dark region contains the entire 0-100% coupling range, so we can use the circuit as a 50 nm broadband tunable coupler with only 3% coupling tolerance.

Similarly, Fig. 4.5 shows the simulation result of the same two-stage tunable coupler, but with imperfect DCs of 40:60 coupling ratio at 1550 nm. The simulation result showed that such design could also work as a tunable coupler with any coupling ratio in 50 nm wavelength range of central wavelength 1550 nm, which means that the two stage tunable coupler design is tolerant to fabrication variations according to simulation. In Fig. 4.5(b), within the working region between 1525 nm and 1575 nm indicated by the dashed line, the device works as a broadband coupler with a deviation less than 3%. Outside this working region, the coupler suffers more wavelength dispersion. The dispersive response of a single DC with 40:60 coupling ratio at 1550nm is also shown by black bold line.Such design also works when the three directional couplers have different coupling values, as long as they are within the safe zone of 25:75 as illustrated in Fig. 4.2.
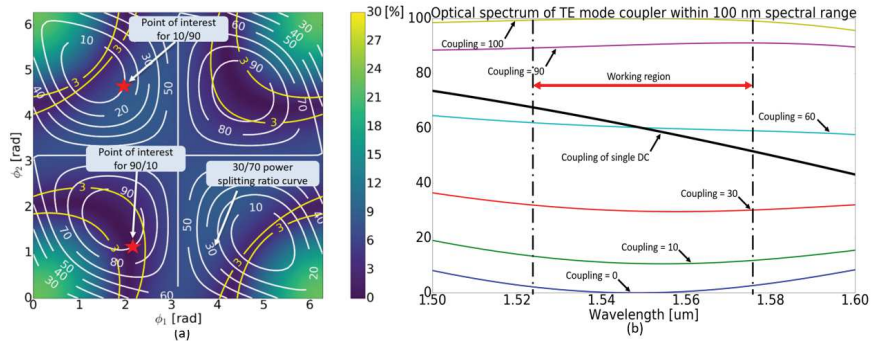
Figure 4.5: Simulation result of a two-stage tunable coupler with imperfect DCs with a 40:60 coupling ratio at wavelength 1550 nm. (a) corresponds to Fig. 4.4d, (b) is the simulated cross power transmission for 0%,10%,40%,70%,90% and 100% coupling ratio.
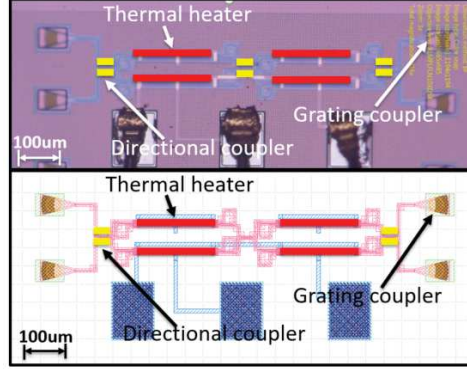
Figure 4.6: Fabricated chip on the IMEC ISiPP50G platform. (a) microscopic image of the fabricated chip and (b) the corresponding GDS layout of the design.

4.5   Experimental results

We had this circuit fabricated on IMEC's standard iSiPP50G silicon photonics platform, which we accessed through the Europractice multi-project wafer service. In total 3 different designs for the two-stage MZI tunable coupler have been fabricated, with different nominal design values for the directional couplers. Device A has a DC designed with a designed 60:40 split ratio for the DCs at wavelength 1550 nm, device B with a 65:35 DC, and device C with a 70:30 DC.

The experimental result is compared with simulation. Fig. 4.7 shows both the simulated and experimental transmission for the bar port of device A. The data was measured by sweeping the voltage applied to the thermo-optic phase shifters, which are implemented with a diode in series, as presented in [9]. The sweeping resolution has been chosen to be 0.1 V, and we measured the transmission for 10 wavelength points in the 50 nm wavelength range. Such resolution should be sufficient to see the trend of the spectral response and allows for a good qualitative match between the simulation and experimental results shown in Fig. 4.7. Fig. 4.7(a-b) show the simulation results of the coupling at 1550 nm and the variation over a 50-nm range (both in dB scale). The dark blue region in Fig. 4.7(b) surrounded by the yellow lines have <1 dB variation, (For a 3 dB coupler, the 1 dB variation region would span from -2 dB to -4 dB. For a -20 dB coupling ratio, the 1 dB region spans from -19 dB to -21 dB.) Fig. 4.7(c-d) is the corresponding experimental result, and we can see a good qualitative agreement. The black rectangles in Fig. 4.7(c-d) correspond to the phase space plotted in Fig. 4.7(a-b).

We can now use the obtained 2-D transmission maps as a look-up table (LUT) for configuring the tunable coupler to search for a desired coupling ratio. This gives us the transmission curves plotted in Fig. 4.8. We see that the variation for
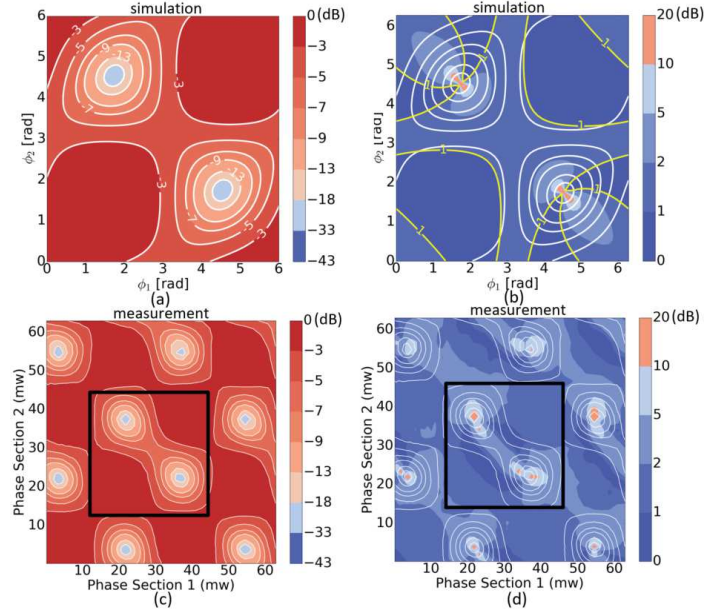
Figure 4.7: Comparison between simulation and experiment for device A (50:50). (a) Simulation result of the coupling at a wavelength of 1550 nm on a logarithmic (dB) scale. (b) Variation plot on a logarithmic (dB) scale.(c,d) Corresponding experimental results for (a,b).
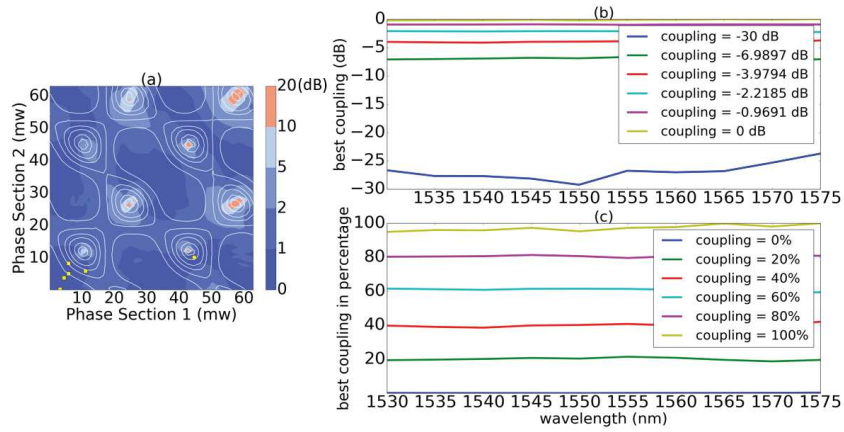
Figure 4.8: Similar to Fig. 4.7(d), the experimental result for the cross port of device B (65:35) is shown in Fig. 4.8a, the yellow dots corresponds to coupling values in (b) Coupling values of 0-100% in steps of 20% are plotted using the LUT of Fig. 4.8(a) in linear scale in Fig. 4.8(b) and in logarithmic scale in Fig. 4.8(c).

larger coupling ratios are significantly higher than that of smaller coupling ratios.

4.6   Optimization algorithm

As we can see from the previous section, the performance of the device is also limited by the measurement resolution used to compose the LUT. As the landscape of the LUT is quite smooth, this resolution can be improved through interpolation. As an alternative, we introduce optimization algorithms with control loops to configure the couplers, which enables us to obtain more accurate coupling values in a shorter time. Control loops can be used for all kinds of purposes [9], such as power control, crosstalk minimization [10] and real-time monitoring [11].

As already demonstrated, the LUT provides but a coarse estimation of the driving voltage of the heaters for the desired coupling value. This can be used as a starting point for an optimization algorithm. For coupling optimization at single wavelength, the gradient-descent algorithm [12] is used. For broadband optimisation, we use the Nelder-Mead method [13]. In the following, we will illustrate how these two algorithms work.

4.6.1   Gradient descent algorithm

The gradient descent algorithm is a first-order iterative optimization algorithm for finding the minimum of a function. In Fig. 4.9, the gradient descent algorithm is applied in the real-time measurement and the trajectory to get to the maximum and minimum output value is plotted out. The output power measured with power meter is used as input value (x) , the model targets to get the best-fit regression to predict the value of y based on x. While training the model, the model calculates the cost function which defined by the Root Mean Squared error between the predicted value $(pred)$ and true value (y). The model targets to minimize this cost function [14].

4.6.2   Nelder-Mead method

The Nelder-Mead method is a commonly applied numerical method used to find the minimum or maximum of an objective function in a multidimensional space [15]. In real time measurement, the voltages applied to the two phase shifters are used as parameters for optimization. For broadband operation, we try to minimize the difference between the targeted output spectrum and the real-time measured value. The targeted spectra are the ideal broadband responses of our coupler. By minimizing the cost function similar in Gradient descent method, we could find the best broadband coupling points in the 2-D phase space. In Fig. 4.8, we already demonstrated the possibility of the device to be configured into a broadband tunable coupler, however in Fig. 4.10, the broadband coupling response of 40% and
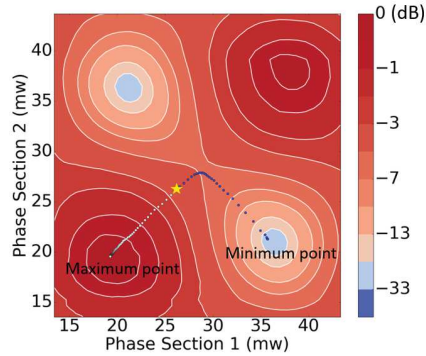
Figure 4.9: Experimental result of searching for the maximum and minimum coupling points with gradient descent method.

50% have been obtained with the Nelder-Mead method as an example. The transfer spectrum is plotted with 0.1 nm resolution. The oscillations are caused by the resonances of the Fabry-Pérot cavities which are formed by the input and output grating couplers.
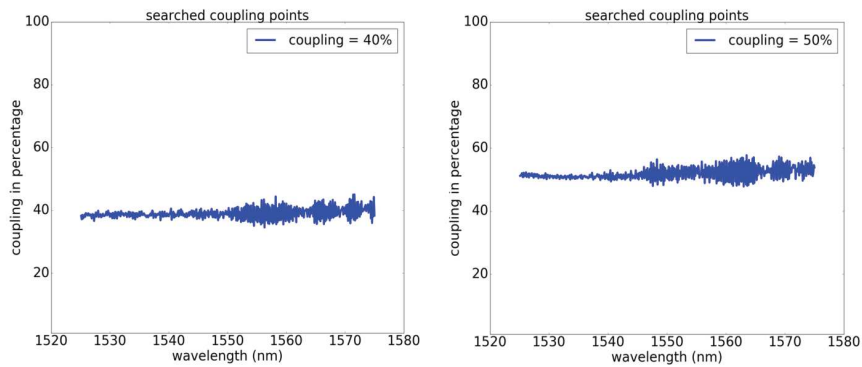
Figure 4.10: Experimental result of searching for the broadband coupling value of 40% and 50% using the Nelder-Mead method.

The ripple we observe on the spectrum originates from a cascade of small backreflections which can be attributed to the grating couplers as well as the interfaces of waveguides with the directional couplers and phase shifters. These can be further reduced by optimizing the individual building blocks.

4.7   Comparison between our design and state of the art

Most of the waveguide-mesh implementations rely on the tunable coupler by means of MZIs based on two 3-dB couplers, so is our proposed design. This tunable coupler offers a wideband tunable range, in the mean time, it is tolerant to fabrication. The power comsumption of such design could be reduced tremendously with the help of under-cut heaters. The power consumption of the undercut heater is around 1.5 mW/pi reported in literature [16]. However the scalability of the circuit is limited by the insertion loss (IL) resulting from the required pairs or 3 50:50 splitters.

The dual-drive directional coupler proposed by Daniel [5] has lower insertion loss. However the power consumption of the design is still significantly high. And the optimization of the thermally tuned dual-drive DC is constrained by fabrication limitations that set minimum distances between metal layers and waveguide layers, among waveguide layers and safety distances for isolation trenches. It is not very clear whether or how this device could reduce its power consumption. Besides, the reported operation bandwidth of the dual-drive DC is around 12 nm, lower than our proposed design.

Thus, the choice of tunable coupler should depends on specific applications. For switch fabric and large programmable circuits, the power consumption and the insertion loss are same important, it is hard to tell whether the tunable coupler based on MZI is better than the dual-drive DC or not. In optical filter and switch fabrics, the operational bandwidth is quite important, then our proposed design definitely is more favorable, besides it could compensate the fabrication variation.

4.8   Comparison between two stage and three stage tunable coupler design

The performance of the one stage MZI is not tolerant to fabrication variation, in order to solve this issue, 2 stage MZI [6] and 3 stage MZI [3] has been proposed. The two stage MZI and three stage MZI is given in Fig. 4.11. In this section, we will analyze the tolerance to fabrication variation for these three designs by monte carlo simulation, the simulation result is shown in Fig. 4.12.

4.9   Conclusion

We have demonstrated a tolerant design for a broadband tunable coupler, consisting of a two-stage MZI. The coupler can be controlled in a two-dimensional space by adjusting the phase delays in both stages of the MZI. The device is tolerant against variations of the directional couplers, as long as their coupling falls within
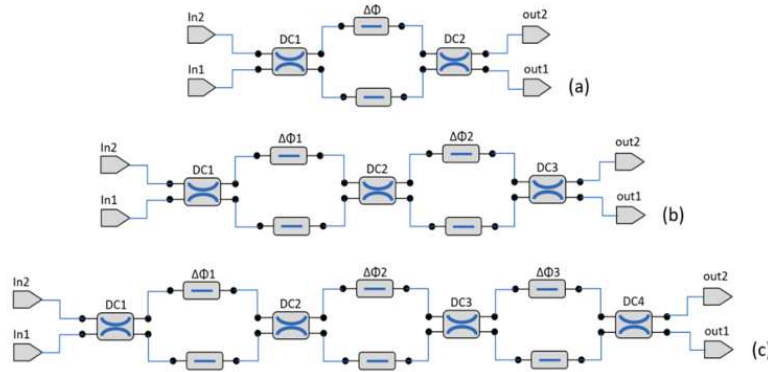
Figure 4.11: (a) is the one stage MZI composed by 2 perfect 3 dB couplers connected with 2 phase shifters. (b) is the two stage MZI design and (c) is the three stage MZI design.
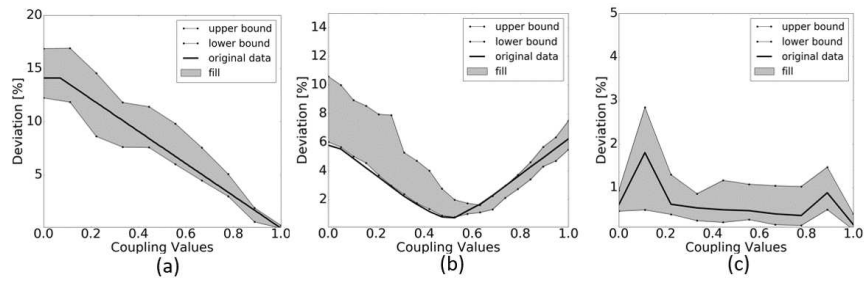
Figure 4.12: Figure (a), (b) and (c) are deviation simulation result for one stage, two stage and three stage MZI designs within 100 nm wavelength range for central wavelength 1550nm, the deviation is plotted as the original data. Later Monte-Carlo simulation is performed to mimic the fabrication variation in the DC. 5% variation of the coupling ratio is chosen and the 100 times Monte-Carlo simulation is applied. For a certain coupling value, the maximum deviation calculated by the Monte-Carlo simulation corresponds to the upper bound and the minimum deviation corresponds to the lower bound, between the upper bound and lower bound is the fill region indicated as grey color.

the range of 25-75%. In addition, we show that, even when the DCs are highly wavelength dependent, the coupler can be configured for wavelength-independent coupling over a wavelength range of 50 nm, and this for all power coupling values from 0% to 100%. The measurement data on the fabricated devices match well with the simulation results. The spectrum variation is demonstrated to be within 5% both in simulation and measurement for the 50 nm wavelength range around 1550 nm for different tunable couplers with intentional variations in the directional couplers. An adaptive tuning algorithm based on the Nelder-Mead method has been tested in real time measurement for configuring the tunable coupler into a

broadband coupler. We also compared two stage MZI design with three stage MZI, the simulation result shows that the three stage MZI design works in a broader wavelength range.

References

[1] Wim Bogaerts, Shankar Kumar Selvaraja, Pieter Dumon, Joost Brouckaert, Katrien De Vos, Dries Van Thourhout, and Roel Baets. *Silicon-on-insulator spectral filters fabricated with CMOS technology*. IEEE journal of selected topics in quantum electronics, 16(1):33–44, 2010.

[2] Daniel Pérez, Ivana Gasulla, and José Capmany. *Programmable multifunctional integrated nanophotonics*. Nanophotonics, 7(8):1351–1371, 2018.

[3] David A. B. Miller. *Perfect optics with imperfect components*. Optica, 2(8):747–750, Aug 2015.

[4] Keijiro Suzuki, Guangwei Cong, Ken Tanizawa, Sang-Hun Kim, Kazuhiro Ikeda, Shu Namiki, and Hitoshi Kawashima. *Ultra-high-extinction-ratio 2 × 2 silicon optical switch with variable splitter*. Opt. Express, 23(7):9086–9092, Apr 2015.

[5] Daniel Pérez-López, Ana M. Gutierrez, Erica Sánchez, Prometheus DasMahapatra, and José Capmany. *Integrated photonic tunable basic units using dual-drive directional couplers*. Opt. Express, 27(26):38071–38086, Dec 2019.

[6] Mi Wang, Antonio Ribero, Yufei Xing, and Wim Bogaerts. *Tolerant, broadband tunable 2× 2 coupler circuit*. Optics express, 28(4):5555–5566, 2020.

[7] Pierre A Besse, Maurus Bachmann, Hans Melchior, Lucas B Soldano, and Meint K Smit. *Optical bandwidth and fabrication tolerances of multimode interference couplers*. Journal of Lightwave Technology, 12(6):1004–1009, 1994.

[8] Zeqin Lu, Han Yun, Yun Wang, Zhitian Chen, Fan Zhang, Nicolas A. F. Jaeger, and Lukas Chrostowski. *Broadband silicon photonic directional coupler using asymmetric-waveguide based phase control*. Opt. Express, 23(3):3795–3808, Feb 2015.

[9] Antonio Ribeiro, Alfonso Ruocco, Laurent Vanacker, and Wim Bogaerts. *Demonstration of a 4×4 port universal linear circuit*. Optica, 3(12):1348–1357, Dec 2016.

[10] Jun Zeng, Donglei Sun, Xiaoming Liu, Xiangyang Cao, Bin Yang, Nan Wang, Dong Liu, and Ying Mu. *Strategy Design for Controlling On-Chip Photonic Circuits*. In 2018 IEEE Student Conference on Electric Machines and Systems, pages 1–6. IEEE, 2018.

[11] Yishen Huang, Qixiang Cheng, and Keren Bergman. *Advanced Control for Crosstalk Minimization in MZI-based Silicon Photonic Switches*. In 2018 IEEE Optical Interconnects Conference (OI), pages 17–18. IEEE, 2018.

[12] Jan A Snyman and Daniel N Wilke. *Practical Mathematical Optimization: Basic Optimization Theory and Gradient-based Algorithms*, volume 133. Springer, 2018.

[13] John A Nelder and Roger Mead. *A simplex method for function minimization*. The computer journal, 7(4):308–313, 1965.

[14] Sebastian Ruder. *An overview of gradient descent optimization algorithms*. arXiv preprint arXiv:1609.04747, 2016.

[15] Marco A Luersen and Rodolphe Le Riche. *Globalized Nelder–Mead method for engineering optimization*. Computers & structures, 82(23-26):2251–2260, 2004.

[16] Adil Masood, Marianna Pantouvaki, Guy Lepage, Peter Verheyen, Joris Van Campenhout, Philippe Absil, Dries Van Thourhout, and Wim Bogaerts. *Comparison of heater architectures for thermal control of silicon photonic circuits*. In 10th International Conference on Group IV Photonics, pages 83–84, 2013.

5

Programmable filter with double ring loaded MZI

Programmable photonic circuits have been well studied in recent years [1], and there have been several demonstrations to achieve a programmable optical filter [2]. The reconfigurability is desired in many applications such as optical interleavers, spectral slicers, or filtering and equalization circuits for microwave photonics [3]. The ability to change its response according to the requirements would on one hand lower the price of the communication channel, on the other hand, it would allow the software to correct or adjust itself with feedback , which is beneficial to the signal performance.

We propose a novel filter circuit that incorporates a double ring resonator with a balanced Mach-Zehnder interferometer (MZI).The circuit has a response equivalent to a conventional ring loaded MZI filter, but with added flexibility in terms of configurability. The second-order filter can also be cascaded to realize higher-order filters. The circuit incorporates a two-stage input and output coupler to further reduce the effect of dispersion. A combination of local and global optimization strategies to program the filter, using tailored objective functions, have been tested in simulation and experiments. We further extend the optimization strategy into experiments and demonstrated its use in practical case for programmable filter circuits.

5.1   Technical challenges

There are few technical challenges for making a programmable filter. Currently, most of the tunable filter has limited tunabilties, such as the higher order CROWs in [4] only have the phase shifters inside the rings tunable. The increasing freedom of tunabilities requires more sophisticated monitoring process [2] or optimization algorithm. The thermal crosstalk and dispersion also degrades the performance of the filter, which has been mainly solved with optimization algorithm [4] [2], the thermal crosstalk could also be reduced with the help of under-cut heater or a thin substrate [2].

5.2   State of the art

Wavelength filters are used to separate two wavelength bands into different output waveguides. They are basic building blocks for optical systems and have a great many applications in communication (wavelength division multiplexing), sensing or spectrometry [5] [6] [7] [1]. When implemented as a waveguide circuit, optical filters are composed of couplers, delay lines, phase shifters, or ring resonators. These components are used to manipulate light to have constructive or destructive interference at certain wavelengths, such that a filter passband is generated. We can identify two basic classes of filters, i.e. finite impulse response (FIR) filter and infinite impulse response (IIR) filter. A FIR filter is composed by forward delays such as MZIs or arrayed waveguide gratings, and these are also called moving average (MA) filters. The IIR filter is composed by feedback loops such as ring resonators, and are also called autoregression (AR) filters. A single ring resonator has its limitations for constructing pass-band filters with a box-like pass band. For that, more complex filter circuits are needed. Double ring resonators can provide a box-like passband with a limited bandwidth, and have been widely used in optical switches. Serially and parallel coupled ring resonator configurations have been described in detail in [8].We hereby present a filter circuit which incorporates both MZI and double ring resonators, which has features from both IIR filter and FIR filter. Such filters, which combine both characteristics, are therefore called auto-regression/moving average (ARMA) filters. A typical example of such an ARMA filter is a so-called ring-loaded MZI, i.e. an MZI with a ring resonator in one or both arms [9], which has been theoretically demonstrated for realizing optical filters with optimum bandpass designs.

The filter circuit developed during this PhD extends the traditional ring loaded MZI by using a double (coupled) ring resonator that links the two arms of the MZI. This circuit has similar functionality as a ring loaded MZI with a single ring in each arm, but the additional coupling facilitates the configuration and even allows for some configurations which are hard to achieve in a traditional RLMZI.

We demonstrated this filter concepts both in simulation and experimentally, and developed optimization algorithms to configure the response of the filter.

The conventional ring loaded MZI filter was proposed by Madson [9] more than 20 years ago. This design was theoretically demonstrated its capability to realize high-quality bandpass filters, and can theoretically fit certain exact bandpass profiles. Even though other types of structures have also been proposed to realize filters, such as nested ring Mach-Zehnder interferometers [10], re-configurable silicon processors based on resonant self-coupled optical waveguides (SCOW) [11], response shaping with a silicon ring resonator via double injection [12], and the cross-ring resonator MZI interleavers [13], none of them has demonstrated their structure to be able to exactly fit to the proposed bandpass filters of the same order.

Ideally, the tunable filter should be able to tune the bandwidth and central wavelength at the same time. The common implementation of the tunable filter is based on either coupled resonator optical waveguide (CROWs) or the double ring or four ring loaded MZI. The CROWs are only able to make butterworth filters, and the structure's flexibility is limited due to the dependency of the filter's bandwidth and out-of-band rejection [4] [14]. The ring loaded MZI, which is demonstrated to be able to implement butterworth, chebyshev and elliptical filter, is theoretically proven to be tunable in bandwidth and shape. The recent experimental results of ARMA filters using a ring-loaded MZI by Sun [15] demonstrated the tunability of such device, but the high in-band ripple and low roll-off make it hard to evaluate whether the device is configured to an elliptical filter or not , which is desired for many applications. The automatic configured ring-loaded MZI by Choo [2] successfully demonstrates that their configuration method could be used to configure the ring-loaded MZI to a elliptical filter with a bandwidth of 3-5 Ghz with a small tunability range, but it lacks experimental results to demonstrate its performance as an interleaver or general-purpose optical filter, or its potential as a universal programmable filter. Besides, such tuning procedure on one hand requires no expensive lab equipment, on the other hand, the additional ring resonator and PDs would introduce additional loss to the whole system. The experimental studies of programmable filter by Pérez [3] also only demonstrated some simple shapes such as single or coupled ring, and FIR filters such as MZIs with delay lines.

In conclusion, some experimental demonstration for a universal programmable filter with tunable bandwidth and shape are missing in the past studies. In this chapter, we not only demonstrate the bandwidth tunability of our proposed ARMA filter (for both Chebyshev and elliptical filter spectra), but also demonstrate that our design can be tuned to a perfect elliptical filter both in simulation and experiments with a maximum 2 dB in-band ripple (which could be further optimized) and an overall 20 dB extinction ratio (and in few cases even 30 dB extinction ratio) for only a single-stage filter design. We also showed that our optimization algorithm helps to tune the parameters of the device accurately into elliptical and Chebyshev

	tunability	simulation	demonstration	optimization
[4]	partially	5th butterworth	butterworth	local
[14]	fully	2th butterworth	butterworth	local
[2]	fully	butterworth chebyshev, elliptical	2th,4th elliptical	assisted with additional ring
[16]	fully	butterworth chebyshev, elliptical	FIR butterworth	local
our design	fully	butterworth chebyshev, elliptical	2th elliptical chebyshev	local global

Table 5.1: integrated silicon photonic tunable filter performance summary and comparison

filters and our structure is a potential candidate for a universal programmable filter.

The chapter is structured as follows: In section 5.3, we describe the architecture of this filter circuit, and the effect of the tunable couplers. Section 5.4 discusses the analytical transfer function and synthesis of the filter, and section 5.5 shows how multiple filters can be cascaded into a higher-order filter. Section 5.6 shows how to transform a filter design to a programmable one. The numerical optimization algorithms to configure the filter are discussed in section 5.7. The experimental results on the fabricated chip are presented in section 5.8. For the fabricated circuit, we extend the filter to use two-stage broadband tunable couplers [17] at the input and output , to improve the dispersion effect of all output channels. Finally, we discuss the benefits and limitations of our filter circuit in section 5.9.

The Appendix A contains the full mathematical derivation of the filter response, and a detailed comparison with the conventional ring-loaded MZI. We also present a tolerance analysis.

5.3   Filter Circuit

The optical filter circuit we propose here incorporates a double ring and a Mach-Zehnder interferometer. The schematic is presented in Fig. 5.1:

In the Appendix A, the z domain pole/zero diagram of the conventional ring loaded MZI and our design have been analyzed. We used a Latin Hypercube sampling method to explore the pole-zero relationship with the design parameters (the coupling coefficients and the phase shifts). Both designs can cover the available space in the z domain, which indicates their capability of exactly realizing optical filters with optimum band-pass designs.
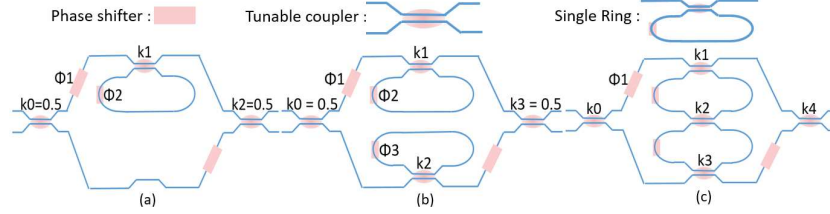
Figure 5.1: Schematic drawing of the single ring loaded MZI is shown in (a), schematic drawing of double ring loaded MZI is shown in (b), schematic drawing of coupled ring loaded MZI is shown in (c). The main difference between our design given in (c) and the ring loaded MZI given in (b) is that the two rings are connected with a tunable coupler, it is obvious that the design in (c) could be configured to a MZI with delay length of twice the ring circumference, which is not straightforward with the design in (b). The phase shifter is shown as a pink box, the tunable coupler is shown as a normal directional coupler with a pink dot in the middle, the single add drop ring is constructed by connecting the input and output port of the tunable coupler on the same side.

5.4 Filter synthesis of an MZI loaded with serially coupled double ring

We can describe the transmission of the filter from the input ports to the output ports using a 2×2 transfer matrix. The transfer matrix can be calculated by multiplying the transfer matrices of each segment in the circuit: the input coupler, the double ring, and the output coupler. Because we choose to use ring resonators with a fixed length L_{ring}, we can apply the transfer matrix method (TMM) in the z domain, with $z = e^{j2.n_{eff}(\lambda).L_{ring}/\lambda}$. The complex amplitudes of the input and output electromagnetic waves in the z domain have the following relationship between each other:

$$\begin{bmatrix} E_{out1} \\ E_{out2} \end{bmatrix} = C_1 \times P_1 \times D_0 \times P_0 \times C_0 \times \begin{bmatrix} E_{in1} \\ E_{in2} \end{bmatrix} \tag{5.1}$$

where E_{in1} and E_{in2} are the complex amplitudes of the light in the fundamental waveguide modes at the inputs, E_{out1} and E_{out2} represent the same quantities at the outputs for the presented device. Matrix C_i is the coupling matrix of each directional coupler, Matrix P_i is the propagation matrix of a phase delay section (consisting of two parallel waveguides or phase shifters) and Matrix D_i is the propagation matrix of the serially coupled double ring. The final transfer function in z notation can be written as the generic transfer function of a second-order filter:

$$H_1 z = \frac{b_0 + b_1 \cdot z^{-1} + b_2 \cdot z^{-2}}{a_0 + a_1 \cdot z^{-1} + a_2 \cdot z^{-2}} \tag{5.2}$$

where a_i and b_i are a function of the coupling ratios and phase shifts of the composition elements. In Appendix A, we show that the a_i and b_i coefficients for the design in Fig. 5.1(b) are usually complex numbers while for the design in Fig. 5.1(c) these coefficients are real numbers. This circuit transfer function is then matched with the expression of a desired second-order filter with coefficients $a_0', a_1', ...b_2'$, using least square fitting, where the error function for complex filer with a_i and b_i to be complex numbers is defined as following:

$$T = ((a_0 \cdot a_0^* - a_0'^2)^2 + (a_1 \cdot a_1^* - a_1'^2)^2 + (a_2 \cdot a_2^* - a_2'^2)^2 +$$
$$(b_0 \cdot b_0^* - b_0'^2)^2 + (b_1 \cdot b_1^* - b_1'^2)^2 + (b_2 \cdot b_2^* - b_2'^2)^2)^{1/2} \qquad (5.3)$$

Likewise, the target function for real filter is:

$$T = ((a_0^2 - a_0'^2)^2 + (a_1^2 - a_1'^2)^2 + (a_2^2 - a_2'^2)^2 +$$
$$(b_0^2 - b_0'^2)^2 + (b_1^2 - b_1'^2)^2 + (b_2^2 - b_2'^2)^2)^{1/2} \qquad (5.4)$$

The full mathematical description of the fitting method has been provided in Appendix A. Here, we will just explain how this fitting method works with the following example. A second-order Chebyshev type II filter is synthesized for the circuit in Fig. 5.1(c). For a second-order low-pass Chebyshev type II filter with a stopband of 10 dB of magnitude response (20 dB for power response) and a normalized edge frequencies of 0.5 π rad/sample , its transfer function is expressed as following:

$$H_z = \frac{1 - 0.29 \cdot z^{-1} + 0.27 \cdot z^{-2}}{0.37 + 0.25 \cdot z^{-1} + 0.37 \cdot z^{-2}} \qquad (5.5)$$

Now we equate the two transfer functions (A.8) and (5.5) together, and solve for the phase shifts and coupling values. The target function is given in Eq. 5.16. The minimization method in the Python package *scipy* is used to numerically solve the equations, which results in the following values:

$$\phi_1 = \pi, k_2 = 0.925, k_0 = k_4 = 0.146, k_1 = k_3 = 0.726 \qquad (5.6)$$

We can see that no phase change in the ring is required in order to configure a second order filter. Such filter therefore has a different tuning strategy than the conventional ring loaded MZI where the phase offset of the two rings determines the frequency response. For these values, we find that the error function is zero, meaning we can obtain a perfect fit. The larger the error function, the worse the circuit performance would be compared to an ideal filter response. In section 5.7 we will go through more details of how to tailor this error function. We have tested that the numerically solved equations have an error function of almost zero for the tested filters such as elliptical filter, Chebyshev type I and type

II filters. The solved phase and coupling values were assigned to a circuit model built with the Caphe circuit simulator by Luceda Photonics [18], the simulation result from Caphe are compared to the desired Chebyshev filter in Fig. 5.2, and we can see that the two spectrum responses overlap very well. The proposed circuit
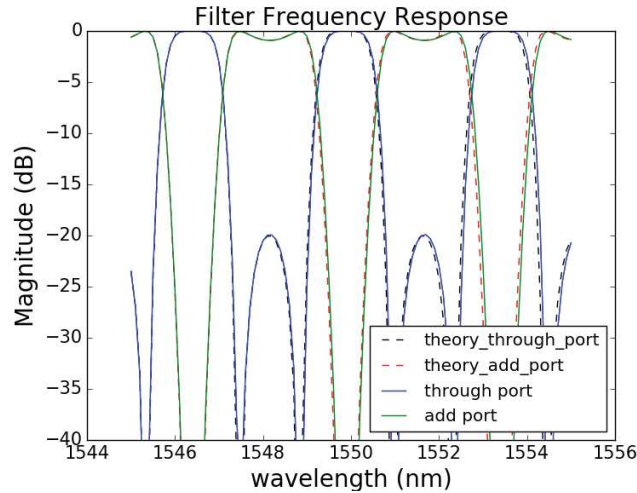
Figure 5.2: A comparison between the theoretical and Caphe simulated spectra for the through and add ports for an ideal Chebyshev type II filter.

in Fig. 5.1 has the following advantages: first, compared with the cascaded ring loaded MZI structure [19], all the rings can be in resonance with each other, so ,it would be more easy to tune the circuit in real-time experiments. Second, for microwave photonics, the proposed structure can realize more filter implementations, such as the coupled-resonator optical waveguide (CROW) [8], the side-coupled integrated spaced sequences of optical resonators (SCISSOR) as well as ring loaded MZI [19] and etc [13], which makes the presented circuit a good candidate for a universal microwave programmable filter in a specialized microwave processor [20]. Finally, the proposed circuit can actually realize some pass band shapes that are not possible with a conventional ring loaded MZI design, which makes the proposed circuit more flexible in arbitrary waveform generation. The details are also discussed in the supplementary materials.

5.5   Cascade for higher order filter

Higher-order filters provide more control over the frequency response with increasing order. The enhancement in roll-off with the higher order filters enables faster transition between the passband and stopband.

The roll-off (measured in dB/decade) reduces by 20 dB/decade per filter order increment. Thus, if a second-order filter function has a roll-off of 20 dB/decade, the fourth-order filter would have a roll-off of 60 dB/decade. This results in a more ideal amplitude frequency response. On the other hand, higher-order filters are complex to configure and design, and they are used only when a sharp transition between the passband and stopband is required.

The order of a high-order filter can be either even or odd. For the synthesis of an n th even-order filter, $n/2$ second order filter can be cascaded to achieve the desired order. In the case for n th order odd filter, one biquadratic sections is replaced by one first-order section, if the general transfer function of a high order filter is given by:

$$H_z = \frac{b_m z^{-m} + b_{m-1} z^{-(m-1)} + ... + b_1 z + b_0}{z^{-n} + a_{n-1} z_{-(n-1)} + ... + a_1 z + b_0} \tag{5.7}$$

Where m is the order of enumerator and n is the order of the denominator, the even n th order filter can be expressed as following:

$$H(z) = \prod_{i=1}^{n/2} A_{\alpha_j} = \frac{b_{2i} z^{-2} + b_{1i} z^{-1} + b_{0i}}{z^{-2} + a_{1i} z^{-1} + a_{0i}} = \prod_{i=1}^{n/2} H_i(z) \tag{5.8}$$

The odd $n + 1$ th order filter will be expressed as following:

$$H(z) = \frac{b_{11} z^{-1} + b_{01}}{z^{-1} + a_{01}} \prod_{i=1}^{n/2} \frac{b_{2i} z^{-2} + b_{1i} z^{-1} + b_{0i}}{z^- 2 + a_{1i} z^{-1} + a_{0i}} = H_1(z) \prod_{i=1}^{n/2} H_i(z) \tag{5.9}$$

Each first and second order equation can be designed independently and individually. The main drawback in this method is the difficulty in tuning the component variation without assistance of a feedback loop.

In this section, we will generate a fourth-order filter with the proposed optical circuit using this cascade technique. The workflow of the synthesis method for a higher-order filter is presented in Fig. 5.3.

We now show an example for the filter synthesis with a fourth-order elliptical low-pass filter with normalized edge frequencies of 0.5π rad/sample, 2 dB pass band ripple and 40 dB attenuation [21]. The transfer function for such a filter is written as:

$$H_z = \frac{0.2318 + 0.3378 \cdot z^{-1} + 0.5297 \cdot z^{-2} + 0.3378 \cdot z^{-3} + 0.2318 \cdot z^{-4}}{1 - 0.3396 z^{-1} + 1.2275 \cdot z^{-2} - 0.3118 z^{-3} + 0.2964} \tag{5.10}$$

$H(z)$ can be decomposed into two second-order filters, $H_1(z)$ and $H_2(z)$, such filter decomposition is done easily in Matlab using the function *zp2tf*, and the corresponding transfer functions are:
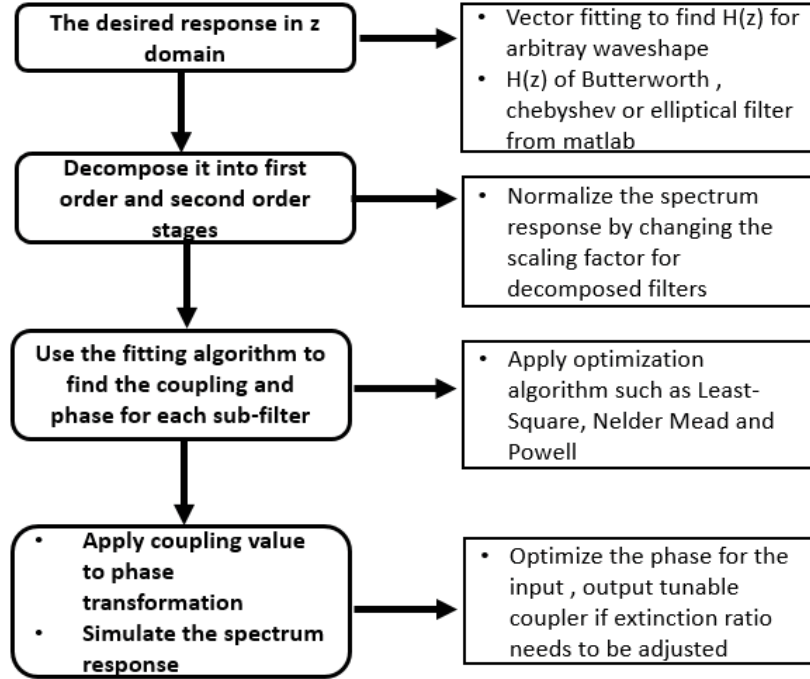
Figure 5.3: Workflow for arbitrary shape or higher order filter synthesis

$$H_1(z) = \frac{0.39 + 0.0910 \cdot z^{-1} + 0.39 \cdot z^{-2}}{1 + 0.0.0094 \cdot z^{-1} + 0.9023 \cdot z^{-2}} \qquad (5.11)$$

$$H_2(z) = \frac{0.3 + 0.3673 \cdot z^{-1} + 0.3 \cdot z^{-2}}{1 - 0.3490 \cdot z^{-1} + 0.0785 \cdot z^{-2}} \qquad (5.12)$$

After executing our before mentioned fitting algorithm for each stage, we get the desired coupling value for the cascaded filter design in Fig. 5.4.

We then generate the corresponding Caphe model for the circuit in Fig. 5.4 and we can see the corresponding spectrum response in Fig. 5.5. The resulting filter has around 34 dB extinction ratio as shown in Fig. 5.5, which is slightly lower than the targeted 40 dB response. The difference between the resulting filter and the targeted design is because of the loss in the waveguide, which was taken into account in the Caphe model.

We take a fourth-order Chebyshev type II filter with 30 dB stop band and 0.5π rad/dB as another example. The power response of the Chebyshev filter will have a 60 dB extinction ratio. The transfer function of such a filter is given by:
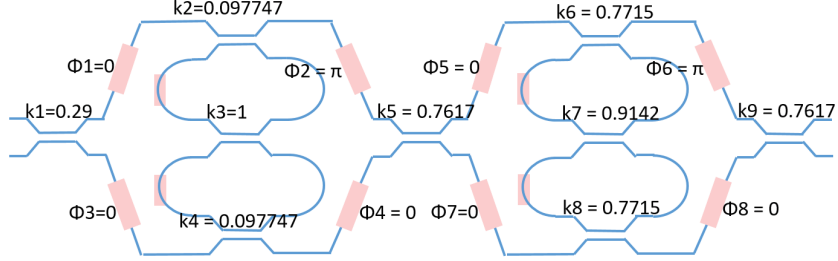
Figure 5.4: Schematic drawing of the programmable filter and the corresponding coupling and phase values to realize the designed elliptical filter.
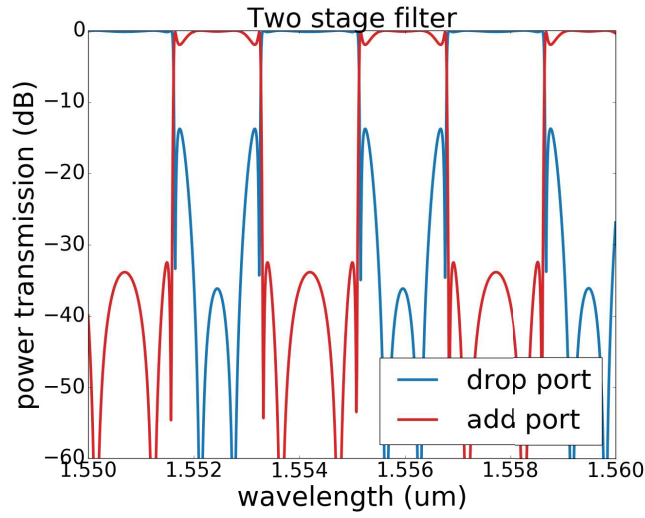
Figure 5.5: Spectrum response of the elliptical filter generated with corresponding Caphe model for the circuit in Fig. 5.4

$$H_z = \frac{0.0996 + 0.164 \cdot z^{-1} + 0.2226 \cdot z^{-2} + 0.164z^{-3} + 0.0996 \cdot z^{-4}}{1 - 0.9055z^{-1} + 0.8128 \cdot z^{-2} - 0.2016 \cdot z^{-3} + 0.0442 \cdot z^{-4}}$$

(5.13)

Eq. 5.13 can be decomposed to two second-order filters, $H_1(z)$ and $H_2(z)$. The corresponding second-order transfer functions are:

$$H_1(z) = \frac{0.35 + 0.0553 \cdot z^{-1} + 0.35 \cdot z^{-2}}{1 + 0.6362 \cdot z^{-1} + 0.5629 \cdot z^{-2}}$$

(5.14)

$$H_2(z) = \frac{0.25 + 0.3723 \cdot z^{-1} + 0.25 \cdot z^{-2}}{1 - 0.2694 \cdot z^{-1} + 0.0785 \cdot z^{-2}}$$

(5.15)
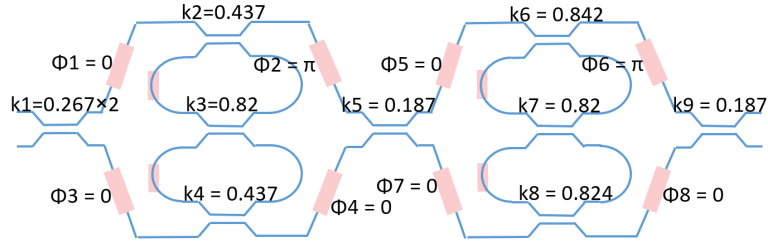
Figure 5.6: Schematic of a two stage filter and the corresponding coupling values and phase response for a fourth-order Chebyshev type II filter with 30 dB stop band and 0.5π rad/dB.

Then we use least-square fitting to find the corresponding coupling value for the each subcircuit. Fig. 5.6 is the schematic drawing of a two-stage filter and the corresponding coupling values and phase response from the least square fitting.
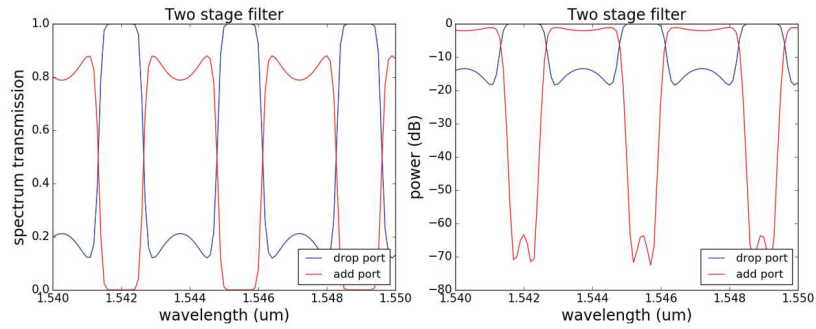
Figure 5.7: Spectrum response for two-stage filter configured for Chebyshev type II response

We then build the Caphe circuit model for the circuit in Fig. 5.6 and we can see the corresponding spectrum response in Fig. 5.7. This shows that the designed filter can reach an extinction ratio of around 60 dB, which meets our requirement.

We have demonstrated that our double ring loaded MZI can implement an elliptical filter and a Chebyshev type II filter with the given filter synthesis and optimization method. The circuit is also capable of implementing filter architectures as shown in [2, 13, 19].

5.6 Programmable filter design

For a programmable filter, we need to be able to adjust the different phases and coupling ratios in our filter circuit. Instead of passive directional couplers, we can

use a tunable coupler, as shown in Fig. 5.8(a). In this work, the tunable coupler is composed of a balanced Mach-Zehnder interferometer, but other types of tunable coupler designs have also been proposed to compensate for fabrication variation or dispersion [17] [22].
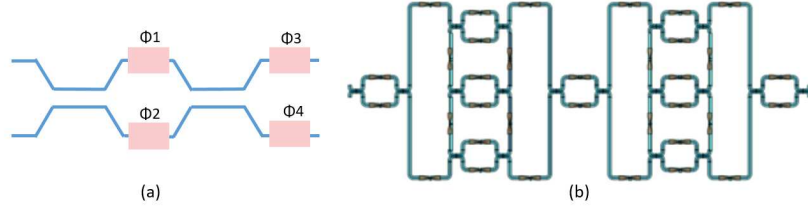
Figure 5.8: (a) is the schematic drawing of a tunable coupler, the pink box denotes the phase shifter, the input and output coupler are 50/50 directional coupler. (b) is the schematic drawing of a programmable two stage filter. The couplers in Fig. 5.6 have been replaced by tunable coupler shown in (a).
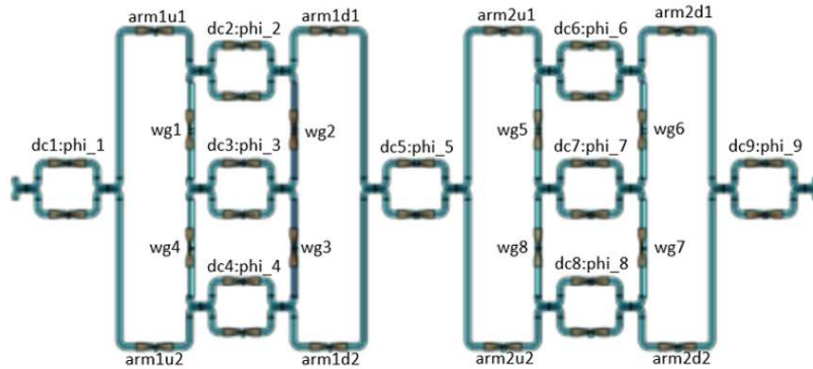
Figure 5.9: Schematic drawing of the implementation of a two-stage programmable filter based on the coupled ring-loaded MZI.

The phases ϕ_1 or ϕ_2 are used to adjust the power coupling. This also introduces a phase shift $(\phi_1 + \phi_2)/2$ at the outputs. So in order to maintain the same phase response as a static directional coupler, we need to use ϕ_3 and ϕ_4 to compensate this additional phase change induced by ϕ_1 and/or ϕ_2. This need for compensation complicates the control of the entire circuit somewhat. If we set the phase shifter of the upper arm of the MZI to be $\phi_1 = x$, and lower arm of the phase shifter to be zero, in order to induce no phase change compared to a passive coupler, then, ϕ_3 and ϕ_4 should have the following value, $\phi_3 = \phi_4 = 2m\pi - x/2$, with m an integer number. For phase shifters that can induce both a positive and negative

dc:phase	Phase	wg:phase		Arm:phase	
dc1: ϕ_1	$\phi_1 = 0.5275\pi$	wg1:ϕ_1	0	Arm1u1:ϕ_1	$-\phi_1/2$
dc2: ϕ_2	$\phi_2 = 0.5402\pi$	wg2:ϕ_2	$-(\phi_2 + \phi_3)/2$	Arm1u2:ϕ_2	$-\phi_1/2$
dc3: ϕ_3	$\phi_3 = 0.279\pi$	wg3:ϕ_3	0	Arm1u2:ϕ_2	$-\phi_2/2 + \pi$
dc4: ϕ_4	$\phi_4 = \phi_2$	wg4:ϕ_4	$-(\phi_4 + \phi_3)/2$	Arm1d2:ϕ_4	$-\phi_4/2$
dc5: ϕ_5	$\phi_5 = 0.5\pi$	wg5:ϕ_5	0	Arm2u1:ϕ_5	$-\phi_5/2$
dc6: ϕ_6	$\phi_6 = 0.26\pi$	wg6:ϕ_6	$-(\phi_6 + \phi_7)/2$	Arm2u2:ϕ_6	$-\phi_5/2$
dc7: ϕ_7	$\phi_7 = 0.279\pi$	wg7:ϕ_7	0	Arm2d1:ϕ_7	$-\phi_6/2 + \pi$
dc8: ϕ_8	$\phi_8 = 0.2755\pi$	wg8:ϕ_8	$-(\phi_8 + \phi_7)/2$	Arm2d2:ϕ_8	$-\phi_8/2$
dc9: ϕ_9	$\phi_9 = \phi_5$				

Table 5.2: Parameters For Fig. 5.9

phase shift, m is preferably zero, but for phase shifters that can only operate in a single direction, such as heater-based phase shifters, $m = 1$.

We replaced all the couplers in Fig. 5.6 with the tunable coupler in Fig. 5.8(a), and built a circuit model for the two-stage filter in Fig. 5.9(b). We then translated the desired coupling in Fig. 5.6(b) to the corresponding phase values in Fig. 5.9(a), including the compensation phases. These parameters of phases are shown in Table 5.2. The spectrum response simulated with the Caphe model of Fig. 5.9(a) is then shown in Fig. 5.10.
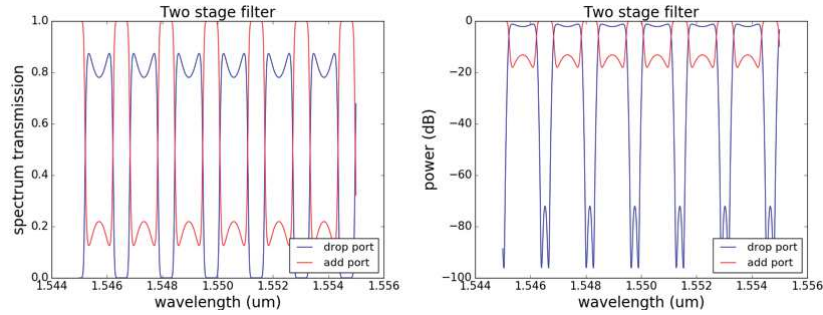
Figure 5.10: Simulation result for the Butterworth filter using the two-stage design with the corresponding caphe model

5.7 Optimization algorithm

There are still several challenges related to our synthesis and optimization procedure. As a starting point, the coupling coefficients corresponding to elliptical filters have been calculated for the lossless case. However, if we want to include the actual waveguide and coupler losses in our model, we could either insert a

loss factor in our analytical derivation, or we could solve the problem by treating the loss as a perturbation in our optimization algorithm. When we take the actual behaviour of the components into account, the spectral dispersion induced by the wavelength dependence of the couplers, fabrication variations, and thermal and electronic cross talk, could all be compensated when the optimization algorithm is applied [23] [24].

The quality of the optimization depends on the target function, and which features of the filter transmission spectrum are the most relevant. We define the target function as follows: The error (difference) between the optimization result and the desired filter response is denoted as x_{lin}, and the difference on a dB scale is denoted as x_{dB}. The first emphasises deviations in the pass band, while the second emphasises the rejection band. The target function is a weighted combination of both:

$$T = w_1 \cdot x_{lin} + w_2 \cdot x_{dB} \tag{5.16}$$

As wavelength filters are phase-sensitive interference-based circuits, we expect that the optimization space has many local optima. It is therefore useful to look into various classes of optimization algorithms that could be helpful for our problem. In this section we focus on two kinds of algorithms, and we show that these algorithms are sufficiently robust to solve our problem in simulation and eventually can be incorporated to optimize and tune the experimental filter circuits in in real time.

5.7.1   Local optimization: Nelder-Mead and Powell

Nelder-Mead [25] and *Powell* [26] are two free-derivative optimization methods. Both methods work well for local optimization starting from a good initial estimate. The *Nelder-Mead* is slow and has a convergence order of 1, which means that large termination errors may occur due to limited iteration steps. It has been tested that the *Powell* method converges much faster than *Nelder-Mead* method in our experiments. The *Nelder-Mead* is often used when the number of optimizable parameters is very large.

Case one: The elliptical filter design in Fig. 5.4 has an extinction ratio of around 34 dB. We could use the Nelder-Mead method to further optimize the spectral response. In this optimization problem, the target function is defined as the error between the spectrum response of the Caphe model on a dB scale and the 40 dB elliptical filter response. The circuit simulation in Caphe [18] of initial 34 dB extinction ratio is optimized to the desired 40 dB elliptical filter response and the result is shown in in Fig. 5.11.

Case two: This second example illustrates more clearly how to define the target function. This time, we start from the 40 dB elliptical filter with 2 dB in-
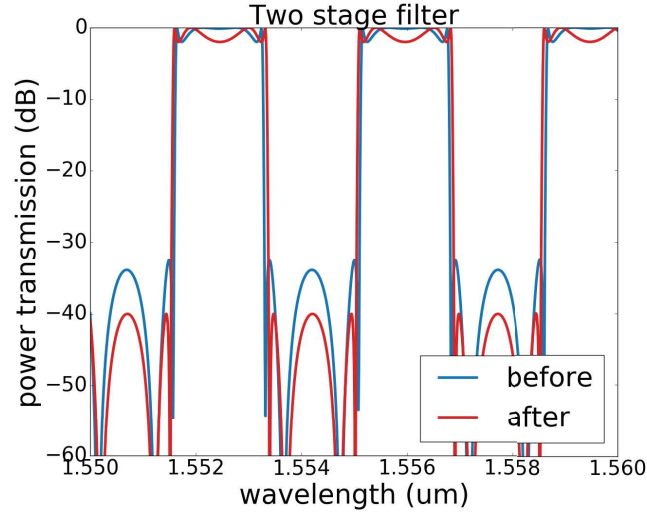
Figure 5.11: Spectrum response of an optimized elliptical filter targeting 40 dB extinction ratio.

band ripple and try to optimize it further to a 60 dB filter with 1 dB in-band ripple. We use multiple optimization steps this time. In the first optimization step, the target function is the error between the 60 dB elliptical function with 1 dB in-band ripple and our original circuit response (the 38 dB elliptical filter with 2 dB in-band ripple). After optimization, we clearly see that the optimized result now has a extinction ratio of 60 dB, but the in-band ripple is larger than expected. In the next optimization steps, we focus on reducing the in-band ripple by assigning a larger weight w_1 to x_1. The final optimization result is shown in Fig. 5.12.

5.7.2   Global optimization: Basin hopping

As an alternative optimization method, we utilized a global optimization algorithm - *Basin hopping* [27]. Basin hopping is a two-phase method that combines a global stepping algorithm with local minimization. We still use the Nelder-Mead method for the local minimization phase. The number of basin-hopping iterations is set according to the difficulty of the problem.

In our experiment of starting from a random position and optimizing it to an elliptical filter, 10 basin-hopping iterations and 100 Nelder-Mead evaluations for each local optimization is used. If we already have a good guess about the coupling values for the filter design (for example, we set $k3 = 1, k2 = k4$ and $k6 = k8$ for the elliptical filter design in Fig. 5.4,) the optimization went very smoothly. However, if we do not have any constraint on the initial coupling values for the
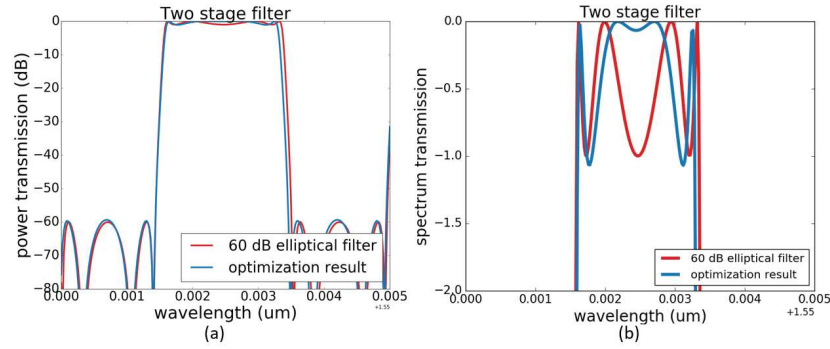
Figure 5.12: Spectrum response of the optimized elliptical filter for an elliptical filter with 1 dB in band ripple and 60 dB extinction ratio.(a) is the final optimization result, which has the desired 60 dB extinction ratio. (b) is a zoom-in on the pass band ripple.The second optimization step successfully lowered this in-band ripple.
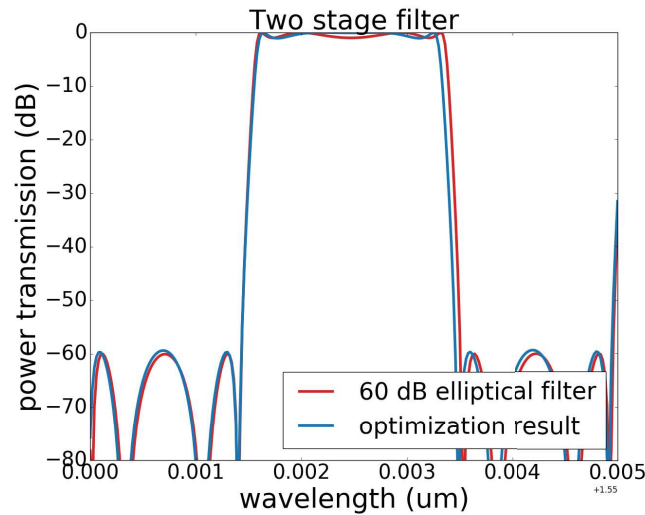
Figure 5.13: Spectrum response of the optimized elliptical filter pass band with Basin-hopping optimization. A 60 dB elliptical filter is the targeted filter response, and the optimization starts from a random position. The final optimized result overlaps very well with the targeted filter response.

design in Fig. 5.4, we need more optimization steps and even need to adjust the target function to get the best optimization result. One typical target function in our experiments is defined as $T = 1.x_1 + 100.x_2$. The final optimized result is shown in Fig. 5.13.:

5.7.3   Packaging of the chip

The packaging of the chip is done in house. The PCB was designed by the lab technician Jasper Jans, then the chip is wire bonded in clean room by technician Steven. After wire-bonding, we shall be able to use current source 64 channel DAC or voltage source Chasis to control the heaters.

Ideally the designs is measured with fiber array since both cross and bar ports could be measured sequentially with the help of a switch. We could either glue the fiber array to the chip using the Hexapod setup or directly measure the chip with Hexapod setup.

Once the packaging of the chip is done, then we could automate the whole measurement procedure and remotely control our measurement.

5.8   Experimental result

In this section, the experimental results for the programmable filter are presented. The silicon photonics chip is fabricated using IMEC's iSiPP50G platform. The mask layout and the corresponding microscopic image are shown in Fig. 5.14. The MZI is loaded with two sets of double ring design with the input and output tunable coupler designed as a two-stage cascaded MZI, as such a design has been proven to have more broadband response [17]. We expect that this will help us to improve the uniformity of the extinction ratio for different channels since the dispersion of the filter response is mainly caused by the dispersion of the tunable coupler.

The measurement setup is shown in Fig. 5.15. The measurement process contains the following steps: 1. the target analog or digital filter is chosen, for example a second-order low-pass Chebyshev type II filter with a stopband of 10 dB of magnitude response (20 dB for power response) and a normalized edge frequencies of 0.5 π rad/sample is chosen as the target filter. Then the filter synthesis procedure is implemented in order to calculate the phase responses of the phase shifters for our filter design. 2. We then map the phase responses of the phase shifters to the voltage or current that we want to apply. This step is called calibration of the phase shifter. Normally we have a asymmetrical MZI as our test design for the calibration. 3. If the thermal crosstalk or electrical crosstalk is insignificant, then the initial spectrum response is similar to the targeted filter response. However, the electric crosstalk is high in our digital-to-analog converters (DAC), thus the initial result is severely disturbed compared to the ideal response, however the initial voltage values are still a good starting point for our optimization process. 4. The optimization algorithm is chosen, the voltage of the heaters are set as the parameters for optimization, the target function defined as the difference between the target filter response and the measured response is being minimized in this
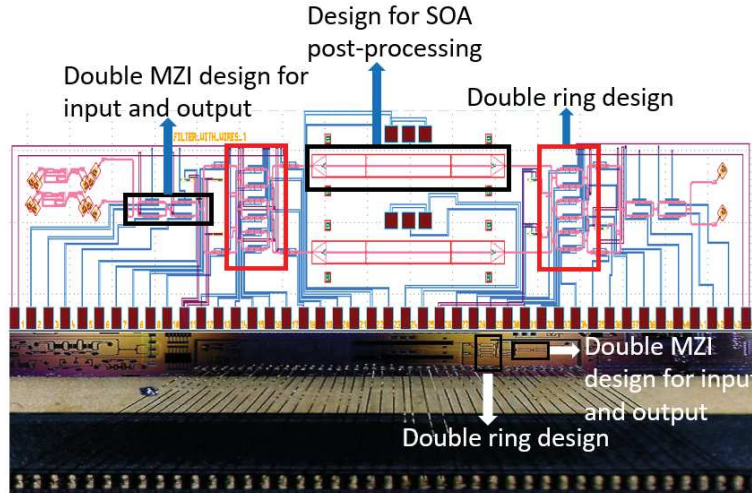
Figure 5.14: The upper figure is the mask layout of the fabricated chip. The basic design is a MZI loaded with two sets of double rings, where the input and output coupler for the MZI are a double-stage balanced MZI [17]. This design also incorporates a placeholder for later semiconductor optical amplifier(SOA) post-processing using transfer printing [28]. Without SOA, the placeholder introduces additional insertion losses., Monitor photodiodes are connected to the inside of the ring resonators and in the arms of the MZIs. The lower image is a microscopic image of the chip, the chip is wire-bonded to a PCB board for electronic control.

process.

The experimental result is obtained first by assigning the phase shifters with the calculated phase values (see the supplementary material for the programmable filter design), however the crosstalk of different electronic channels of the digital-to-analog convector and thermal crosstalk of the phase shifters degrades the spectrum responses severely compared to the original prediction. Therefore the optimization algorithm is needed to finetune the device. The *Powell* method is chosen for this step since it converges faster than the *Nelder-Mead Method* in experimental settings.

Fig. 5.16 shows that the measured transmission matches well with the targeted simulation curve, the extinction ratio of 20 dB is achieved by all the filter types, some even have an extinction ratio of 30 dB. The spectrum response in a larger wavelength range is also measured in Fig. 5.17 , and we see (as expected) that the dispersion of the building blocks starts to have a strong effect on the extinction ratio. Fig. 5.17(a) is filter response in a small wavelength range, while Fig. 5.17 (b) is the same filter response measured over a larger wavelength range, among the measured 5 channels, only 2 channels have an extinction ratio over 30 dB, however all the channels have an extinction ratio over 20 dB. Fig. 5.17 (c) and (d) show the
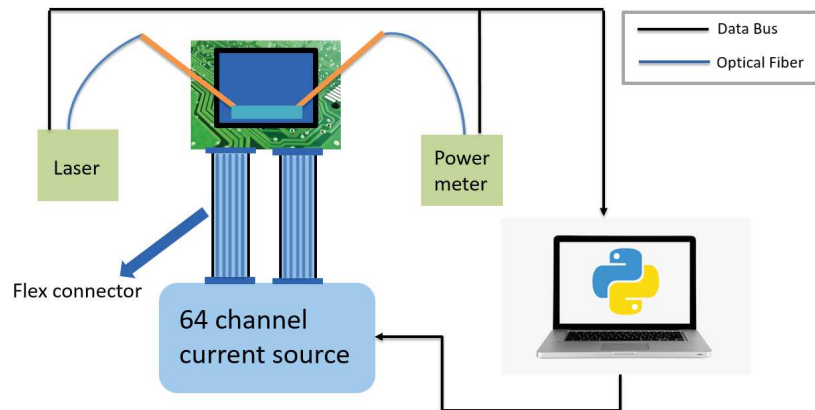
Figure 5.15: The measurement setup is composed of a tunable laser as input light source, a power meter to measure the spectrum response for the drop and through port and a 64 channel current source to control the heaters. All these measurement instruments are controlled by the computer, and the optimization algorithm takes the real-time measured power values as input and controls the current source.

filter response over 10 channels, where the dispersion effect is even more obvious.

5.9 Tolerance analysis

In experiments, the dispersion of the building blocks, as well as the fabrication variation and thermal cross-talk need to be considered, as they move the filter away from its nominal operating point and complicate the configuration and control. Fig. 5.18 is a Monte-Carlo simulation performed for two filter designs in Fig. 5.6 for a given filter response, and it is hard to tell which filter is better in terms of fabrication variation. It is certain, however, that the phase shifters inside the ring contribute the most significantly to the deformation of the spectrum response.

Discussion

In this manuscript, we propose a novel architecture of a programmable ring loaded MZI filter to implement a programmable filter. The FSR of the measured filter is 0.785nm, and it is designed for 100 GHz channel spacing. Such filter has the potential to be used as optical interleaver.With the accompanying optimization strategy we have shown that we can configure different ARMA filter transmission spectra. We did this by only tuning the coupling coefficients of the tunable couplers in the filter, without tuning the phase shifters.The tuning strategy proposed
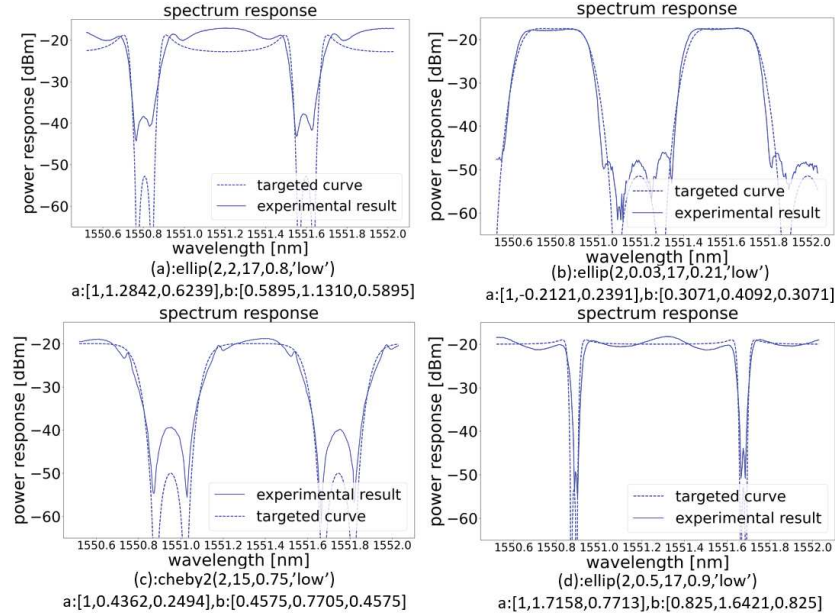
Figure 5.16: Experimental transmission spectra of the double ring-loaded MZI filter. Each plot shows the target design (with the a_i and b_i coefficients listed below the plot). The experimental results are obtained by optimizing the spectral response from the chip outputs by driving the on-chip actuators in real time. From the measurement we can see, the experimental results matches the simulation quite well, and the overall extinction ratio exceeds 20 dB for all designs.

by Gihoon [2] for the conventional ring-loaded MZI is enabled by one additional ring with photodiode and by characterizing each individual tunable coupler. Such an algorithm would work if the thermal and electric crosstalk between heaters is sufficiently small. However, due to the large thermal and electric crosstalk in our system, the initial calibration did not yield a good performance. Thus another optimization step for multiple heaters together is necessary.

In our design, the photodiode inside the ring could be used to actually calibrate the coupler values and also to align the two rings. It can be used in the coarse tuning step, and then the optimization algorithm could be applied in a second step for fine tuning. One important factor why such tuning algorithm would work in our filter is because of the design itself - the rings are initially zero-phase and in phase with each other (see supplementary material), and drift during operation could therefore be easily calibrated with the help of an integrated photo-diode. The optimization algorithm thus only deals with the coupler values, which made the whole tuning process much faster. The temperature change of the phase shifters over time can also be compensated with the photodiodes once the initial calibration
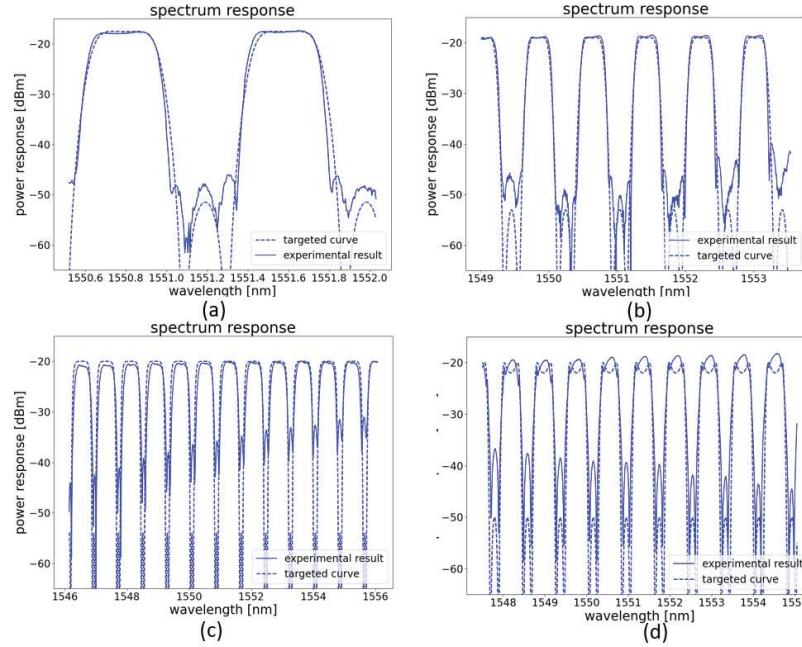
Figure 5.17: Effect of dispersion effect for different filter configurations. (a) is a re-plot of Fig. 5.16(b), the wavelength range is from 1550.6 nm to 1552.0 nm. (b) is the same filter measured in a larger wavelength range of 1549 nm to 1554 nm. (c) and (d) are two examples with more than 10 channels in 10 nm wavelength range. The dispersion effect has a strong impact on the extinction ratio between different channels.

has been performed. The drawback of including monitor diodes in the filter circuit is that these induce losses. Especially when monitor diodes are introduced in the rings, this limits the quality factor, and therefore the promixity of the poles to unit circle in the z plane. Indeed, in our circuit the losses are mainly induced by the monitors, the monitors tap off 1% of the light in the waveguide. Some losses of the filter could be compensated by integrating amplifiers inside or outside the filter (which was foreseen in the design, as shown in Fig. 5.14(a). Configuration difficulties due to thermal crosstalk could be reduced by using heaters with better insulation [29], or use a non-dissipative tuning mechanism such as MEMS [30].

In our experiment, we still see that the default cross state for the second set of two coupled ring (three couplers of the second set of double ring structures) does not impact the performance of the first set of coupled rings. Besides tuning the device with the real time optimization strategy, an alternative way of using such a filter circuit would be to build a look-up table for the filter, and once the filter is calibrated for a certain performance, the tuning parameters would be recorded. Such optimization works well even without monitors.
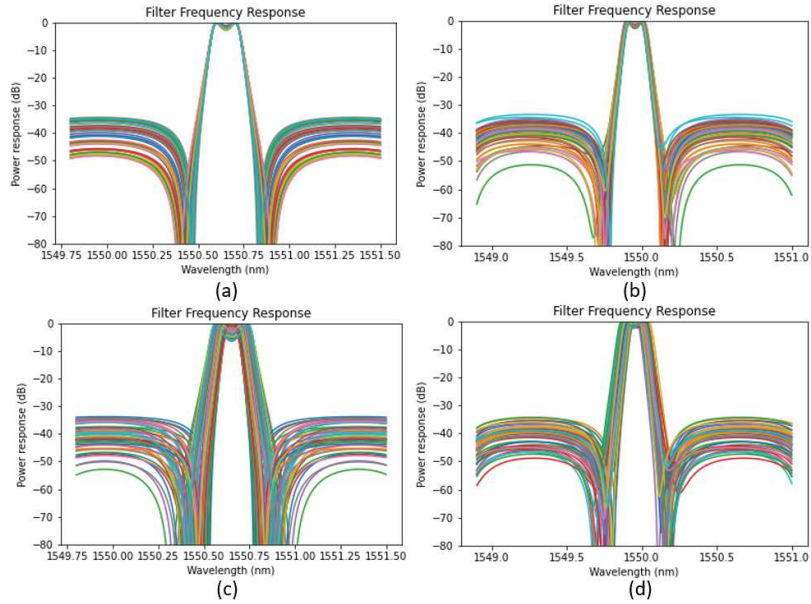
Figure 5.18: Monte-Carlo simulation for two filter configurations in Fig. 5.6, (a) and (c) are for the classical ring-loaded MZI design, (b) and (d) are for the coupled ring-loaded MZI design. For (a) and (b), 5% parameter variation is applied to all the parameters except for the phases in the rings. For (c) and (d), all the parameters including the ring phase shifters) have a 5% variation in the Monte-Carlo simulation.

The estimated Q factor of a single ring is 18184, the full calculation of it is in Appendix A. The main loss in our system is from the loss of the waveguide and the doped heater. If we change the platform to SiN platform, we could further improve the Q factor of our system, however at the cost of much more tuning power and potentially much worse thermal crosstalk.

The power consumption of the filter depends on the number of heaters used in the system. For a single stage of a coupled ring-loaded MZI we require 10 phase shifters, and we're not using the other actuators in the circuit in Fig. 5.14. For full tunability, we can assume that each phase shifter's average shift is π, with an averaged power consumption of 20 mW. Thus, the total power consumption in our current system is around 200 mW. We are considering to replace the doped heater with undercut heater in our future design, the power consumption of the undercut heater is around 1.5 mW/π reported in literature [29].

5.10   Application of the proposed filter

The application of such kinds of bandpass filters as interleaver would improve the signal to noise ratio and give a better eye-diagram in a communication link.

5.10.1   Optical interleaver

The operation principle of a interleaver is given in Fig. 5.19. It is a 3-port passive device that is used to combine two sets of dense wavelength-division multiplexing (DWDM) channels into a composite signal stream in an interleaving way. The device can also be used as an optical deinterleaver when operating in a reverse direction. Normally the interleaver is a half band filter, which means that the bandwidth of the stop band and pass band are equal to each other as it shown in Fig. 5.19.
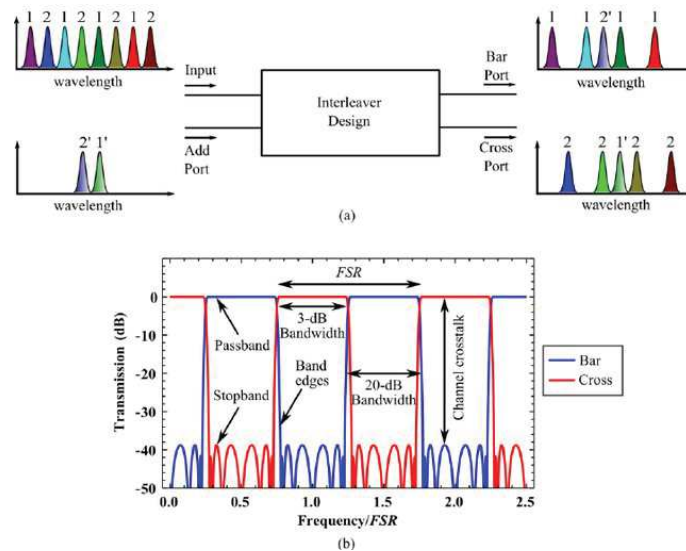
Figure 5.19: (a) shows the working principle of a interleaver design, it could used to separate the odd and even channels or it could used to add or drop signals in the bar and cross port. (b) is the a typical half band interleaver, the extinction ratio for the both bar and cross ports is 40 dB, which is also the crosstalk level for the interleaver.

There are certain specs needed to be fulfilled when using the design as an optical interleaver. It should be operated in C/O or C+O band, the extinction ratio for the drop and add ports should be larger than 10 dB at least.

We have demonstrated that our filter design is a good candidate as an optical interleaver for the C band, we also demonstrated that our design could be also used as a tunable interleaver with tunable bandwidth. The schematic of our design and

the GDS of it is shown in Fig. 5.20.
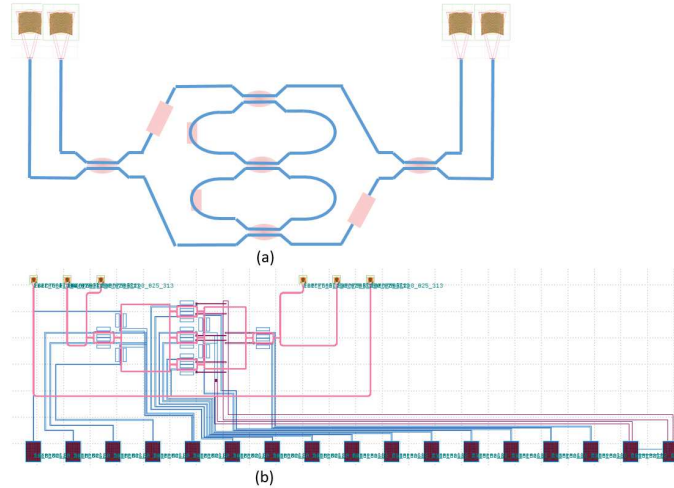
Figure 5.20: (a) is the schematic drawing of our interleaver, the fiber array enables the measurement of the add port and drop port sequentially by a switch, the optimization algorithm could also be applied to measurement of both ports at the same time in order to make sure the crosstalk is low for both ports.(b) is the GDS layout for such design.

The packaging of the chip is similar as before, we wire bond the chip and use the 64 channel DAC to control the heaters. This time the fiber array is glued to the chip and we are using switch to sequentially measure the cross and bar ports.The optimization algorithm is also used in this measurement, the target function is defined as sum of the error of the drop port and add port. In this way, we are co-optimizing the cross port and bar port at the same time.

Below is a detailed description of the measurement procedure. In order to perform the optimization, the target function needs to be defined accurately. We use the CMA algorithm to fit the FSR and phase of the target function to that of the measurement result first, then we use the fitted target function in our next optimization step. The error function is defined to be the sum of the error in the add port and drop port in dB scale. In other words, we are optimizing the add port and drop port at the same time.

The optimization result for the experimental measurement is shown in Fig. 5.21. The desired interleaver should work in C band (1530 nm-1565 nm), however the measurement result is centered at 1530 nm. The reason for it is that the directional coupler we use was designed for an older IMEC process, thus the center frequency of the directional coupler is shifted in the new IMEC process.

We also see that the measurement result suffers from severe dispersion, thus, replacing the directional coupler with broadband device such as an MMI or broad-

band directional coupler would solve this problem.

Some other interleaver designs based on ring loaded to a unbalanced MZI have also been proposed, The ring loaded to a unbalanced MZI has been widely used as optical interleaver [31]. The coupled ring loaded to a unbalanced MZI might help to improve the extinction ratio of the interleaver response.
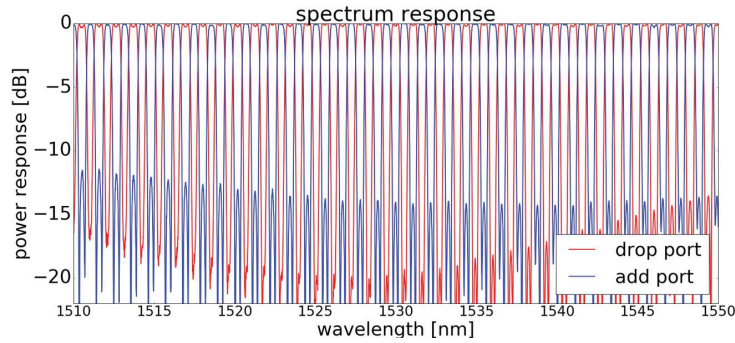
Figure 5.21: Optimization result in 40 nm wavelength range

We also demonstrated that the bandwidth of the interleaver is tunable by showing an experimental result of an interleaver in Fig. 5.22.The bandwidth of the interleaver is changed, so is the operation wavelength and crosstalk level.
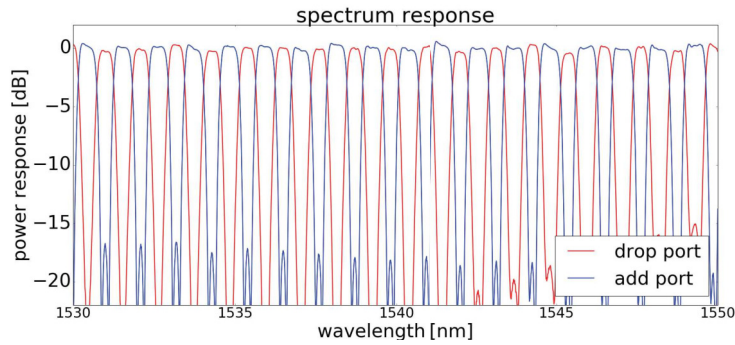
Figure 5.22: A spectrum response with 20 nm wavelength range for the optical interleaver. The extinction ratio exceeds 15 dB in both add and drop ports.

5.11   Conclusion

In this chapter, we have proposed a ring-resonator based circuit to realize a configurable second-order autoregressive–moving-average (ARMA) filter. We have

shown that such circuit can be cascaded to realize higher-order filters. We also demonstrated optimization of the tuning coefficients both in simulation and in experiments.

References

[1] Wim Bogaerts, Daniel Pérez, José Capmany, David A. B. Miller, Joyce Poon, Dirk Englund, Francesco Morichetti, and Andrea Melloni. *Programmable photonic circuits*. Nature, 586(4):1476–4687, 2020.

[2] Gihoon Choo, Shengchang Cai, Binhao Wang, Christi K Madsen, Kamran Entesari, and Samuel Palermo. *Automatic monitor-based tuning of reconfigurable silicon photonic APF-based pole/zero filters*. Journal of Lightwave Technology, 36(10):1899–1911, 2018.

[3] Daniel Pérez, Aitor López, Prometheus DasMahapatra, and José Capmany. *Multipurpose self-configuration of programmable photonic circuits*. Nature Communications, 6359(11):2041–1723, 2020.

[4] Jason C. C. Mak, Wesley D. Sacher, Tianyuan Xue, Jared C. Mikkelsen, Zheng Yong, and Joyce K. S. Poon. *Automatic Resonance Alignment of High-Order Microring Filters*. IEEE Journal of Quantum Electronics, 51(11):1–11, 2015.

[5] Roel Baets, Ananth Z. Subramanian, Ashim Dhakal, Shankar K. Selvaraja, Katarzyna Komorowska, Frédéric Peyskens, Eva Ryckeboer, Nebiyu Yebo, Gunther Roelkens, and Nicolas Le Thomas. *Spectroscopy-on-chip applications of silicon photonics*. In Jean Emmanuel Broquin and Gualtiero Nunzi Conti, editors, Integrated Optics: Devices, Materials, and Technologies XVII, volume 8627, pages 87 – 96. International Society for Optics and Photonics, SPIE, 2013.

[6] Wim Bogaerts, Shankar Kumar Selvaraja, Pieter Dumon, Joost Brouckaert, Katrien De Vos, Dries Van Thourhout, and Roel Baets. *Silicon-on-Insulator Spectral Filters Fabricated With CMOS Technology*. IEEE Journal of Selected Topics in Quantum Electronics, 16(1):33–44, 2010.

[7] *Introduction*, chapter 1, pages 1–17. John Wiley Sons, Ltd, 1999.

[8] Vien Van. *Synthesis of elliptic optical filters using mutually coupled microring resonators*. Journal of lightwave technology, 25(2):584–590, 2007.

[9] C.K. Madsen. *Efficient architectures for exactly realizing optical filters with optimum bandpass designs*. IEEE Photonics Technology Letters, 10(8):1136–1138, 1998.

[10] S. Darmawan, Y. M. Landobasa, and M. K. Chin. *Nested ring Mach-Zehnder interferometer*. Opt. Express, 15(2):437–448, Jan 2007.

[11] Liangjun Lu, Lin Shen, Wei Gao, Linjie Zhou, and Jianping Chen. *Reconfigurable Silicon Photonic Processor Based on SCOW Resonant Structures*. IEEE Photonics Journal, 11(6):1–12, 2019.

[12] Amrani O. Ruschin S. Cohen, R.A. *Response shaping with a silicon ring resonator via double injection*. Nature Photon, 12:706–712, 2018.

[13] Junfeng Song, H. Zhao, Q. Fang, S. H. Tao, T. Y. Liow, M. B. Yu, G. Q. Lo, and D. L. Kwong. *Effective thermo-optical enhanced cross-ring resonator MZI interleavers on SOI*. Opt. Express, 16(26):21476–21482, Dec 2008.

[14] Jason C. C. Mak, Antoine Bois, and Joyce K. S. Poon. *Programmable Multiring Butterworth Filters With Automated Resonance and Coupling Tuning*. IEEE Journal of Selected Topics in Quantum Electronics, 22(6):232–240, 2016.

[15] Qiankun Sun, Linjie Zhou, Liangjun Lu, Gangqiang Zhou, and Jianping Chen. *Reconfigurable High-Resolution Microwave Photonic Filter Based on Dual-Ring-Assisted MZIs on the Si3N4 Platform*. IEEE Photonics Journal, 10(6):1–12, 2018.

[16] Daniel Pérez, Aitor Lopez, DasMahapatra Prometheus, and Capmany José. *Multipurpose self-configuration of programmable photonic circuits*. Nature Communications, 6359(11), 2020.

[17] Mi Wang, Antonio Ribero, Yufei Xing, and Wim Bogaerts. *Tolerant, broadband tunable 2× 2 coupler circuit*. Optics express, 28(4):5555–5566, 2020.

[18] Martin Fiers, Thomas Van Vaerenbergh, Ken Caluwaerts, Dries Vande Ginste, Benjamin Schrauwen, Joni Dambre, and Peter Bienstman. *Time-domain and frequency-domain modeling of nonlinear optical components at the circuit-level using a node-based approach*. J. Opt. Soc. Am. B, 29(5):896–900, May 2012.

[19] K. Jinguji. *Synthesis of coherent two-port optical delay-line circuit with ring waveguides*. Journal of Lightwave Technology, 14(8):1882–1898, Aug 1996.

[20] Xin Guo, Y. Liu, Tangman Yin, B. Morrison, M. Pagani, Okky Daulay, W. Bogaerts, B. Eggleton, A. Casas-Bedoya, and D. Marpaung. *Universal Silicon Microwave Photonic Spectral Shaper*. 2020.

[21] Inc. The MathWorks. *Elliptical filter design*. `https://nl.mathworks.com/help/signal/ref/ellip.html`. Accessed: 2021-08-18.

[22] Daniel Pérez-López, Ana M. Gutierrez, Erica Sánchez, Prometheus DasMahapatra, and José Capmany. *Integrated photonic tunable basic units using*

dual-drive directional couplers. Opt. Express, 27(26):38071–38086, Dec 2019.

[23] J. C. C. Mak, W. D. Sacher, T. Xue, J. C. Mikkelsen, Z. Yong, and J. K. S. Poon. *Automatic Resonance Alignment of High-Order Microring Filters*. IEEE Journal of Quantum Electronics, 51(11):1–11, Nov 2015.

[24] Jason C. C. Mak, Tianyuan Xue, Zheng Yong, and Joyce K. S. Poon. *Wavelength Tunable Matched-Pair Vernier Multi-Ring Filters Using Derivative-Free Optimization Algorithms*. IEEE Journal of Selected Topics in Quantum Electronics, 26(5):1–12, 2020.

[25] Saša Singer and John Nelder. *Nelder-mead algorithm*. Scholarpedia, 4(7):2928, 2009.

[26] Roger Fletcher and Michael JD Powell. *A rapidly convergent descent method for minimization*. The computer journal, 6(2):163–168, 1963.

[27] David J Wales and Jonathan PK Doye. *Global optimization by basin-hopping and the lowest energy structures of Lennard-Jones clusters containing up to 110 atoms*. The Journal of Physical Chemistry A, 101(28):5111–5116, 1997.

[28] Bahawal Haq, Javad Rahimi Vaskasi, Jing Zhang, Agnieszka Gocalinska, Emanuele Pelucchi, Brian Corbett, and Gunther Roelkens. *Micro-transfer-printed III-V-on-silicon C-band distributed feedback lasers*. Opt. Express, 28(22):32793–32801, Oct 2020.

[29] Adil Masood, Marianna Pantouvaki, Guy Lepage, Peter Verheyen, Joris Van Campenhout, Philippe Absil, Dries Van Thourhout, and Wim Bogaerts. *Comparison of heater architectures for thermal control of silicon photonic circuits*. In 10th International Conference on Group IV Photonics, pages 83–84, 2013.

[30] Niels Quack, Hamed Sattari, Alain Yuji Takabayashi, Yu Zhang, Peter Verheyen, Wim Bogaerts, Pierre Edinger, Carlos Errando-Herranz, and Kristinn B. Gylfason. *MEMS-Enabled Silicon Photonic Integrated Devices and Circuits*. IEEE Journal of Quantum Electronics, 56(1):1–10, 2020.

[31] Anthony Rizzo, Qixiang Cheng, Stuart Daudlin, and Keren Bergman. *Ultra-Broadband Interleaver for Extreme Wavelength Scaling in Silicon Photonic Links*. IEEE Photonics Technology Letters, 33(1):55–58, 2021.

6

Conclusions

In this chapter, some past projects from the beginning of my PhD are discussed. Some directions to continue the research work have also been discussed in this chapter.

6.1 Generalized programmable filters

The generalized programmable filters are normally made with mesh circuits, there are in total 3 mesh circuits, triangular mesh, rectangular mesh and hexagonal mesh. The demonstration of triangular and rectangular mesh was implemented by . Prof. Vien Van did some work on the filter made with 2-D coupled rings, he developed the filter synthesis algorithm with 2D coupled ring resonator structure based on the book "optical mirroring resonators, theory, techniques, and applications". The 2D coupled ring filter could be realized with our Hexagonal mesh circuit as is shown in Fig. 6.1.

I have reproduced the filter synthesis algorithm, I have also implemented filter synthesis algorithm for cascaded ring loaded MZI structure. The filter configuration obtained by the synthesis algorithm could apply to our proposed filter design given in Chapter 5.

The experimental demonstration of hexagonal mesh was implemented by Perez at first. The mesh circuit showed its capability to be configured as feed-forward circuits, FIR filter, butterworth and chebyshev filters. The FSR of the ring resonator implemented by mesh circuits is relatively small compared to standard ring
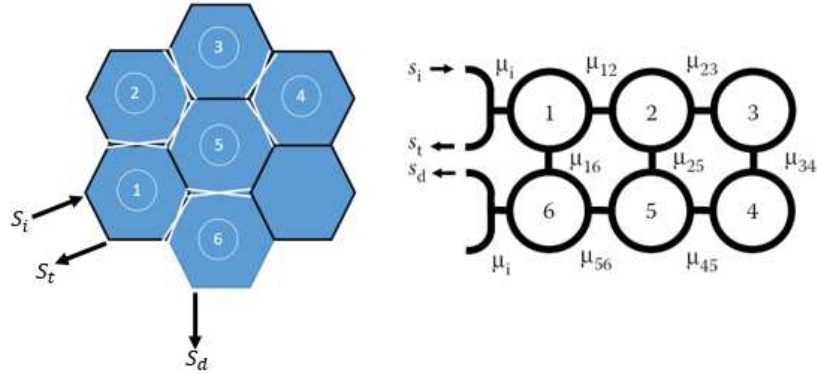
Figure 6.1: The left figure is the 7 cell hexagonal mesh circuit, the right figure is the 2D coupled ring filter. The left 7 cell hexagonal mesh circuit could be configured to the 2D coupled ring filter as shown in left figure

resonator.

In order to solve this issue, we have proposed to combine venier ring design and the rectangular mesh circuit. The advanced circuits are based on square meshes of coupled rings but using different ring lengths to increase the FSR.

Schematic of the venier ring assisted rectangular mesh circuit is shown below:

6.2   Summary

The main goal of this work was to investigate a programmable component - programmable filter design. In the meantime, we are also interested in the improvement for the basic component -tunable coupler.

This dissertation gave an overview into the novel programmable filter and its configuration and optimization strategies. The design methodology , optimization algorithm could also extended to the general purpose programmable mesh circuit. During this work,

We started off with the most basic component design - broadband coupler. Such design is widely used in the programmable circuit. We later proposed a tolerant , broadband tunable coupler circuit design. Such design is not only tolerant to fabrication variation, it also has a broadband spectrum response.

We then proposed a novel optical filter design. We have proved that the filter could be used to synthesis all kinds of filter, including butter-worth filter, elliptical filter, chebyshev type I and type II filter. We also show that the filter design could be cascaded to realize higher order filters.

In reality, the loss of the waveguide, thermal crosstalk, electrical crosstalk will

degrade the performance of the filter. On one hand, we could use monitor in the rings and MZIs to monitor the response of the phase shifter. The feedback circuit is needed to lock the response of the phase shifter. This method would work only if the thermal and electrical crosstalk is small, thus the tuning of a single phase shifter would not impact the response of another phase shifter. On the other hand, we could directly optimize the spectral response of the output port. Although the real-time optimization is bit time-consuming, we could build up the look-up table to facilitate the configuration later.

The local optimization algorithm Powell and Nelder Mead works both in simulation and experiments, it helps change the extinction ratio of the filter performance , it also works well in finding the optimized filter response starting from a good initial guess.

The global optimization algorithm Basin Hopping also shows excellent performance in simulation with a random starting point.

Finally we verified the simulation results with real experimental data.

References

A

Appendix A

A.1 Filter synthesis of an MZI loaded with serially coupled double ring

The transmission of the filter from the input ports to the output ports can be calculated by the following transfer matrix multiplication in the z domain. Because we choose to use ring resonators with a fixed length L_{ring}, we can apply the transfer matrix method (TMM) in the z domain, with $z = e^{j2.n_{eff}(\lambda).L_{ring}/\lambda}$.

The complex amplitude of the input and output electromagnetic waves in the z domain have the following relationship between each other:

$$\begin{bmatrix} E_{out1} \\ E_{out2} \end{bmatrix} = C_1 \times P_1 \times D_0 \times P_0 \times C_0 \times \begin{bmatrix} E_{in1} \\ E_{in2} \end{bmatrix} \tag{A.1}$$

The coupling matrix, C_i, is given by:

$$C_i = \begin{bmatrix} \sqrt{1 - k_i} & -j\sqrt{k_i} \\ -j\sqrt{k_i} & \sqrt{1 - k_i} \end{bmatrix} \tag{A.2}$$

where k_i is the power cross-coupling coefficient, and $1 - k_i$ is the straight-through coefficient for the directional coupler (assuming lossless operation). The propagation matrix P_i of each phase delay section is given by:

$$P_i = \begin{bmatrix} e^{-j\phi_i} & 0 \\ 0 & 1 \end{bmatrix}, \tag{A.3}$$

where we assume no loss, and equal length for waveguide propagation, so the common propagation terms can be ignored.

The propagation matrix D_i of serially coupled double ring section is given by:

$$D_i = \frac{1}{\delta} \begin{bmatrix} X_1 & -j \cdot e^{-1j(\phi_2+\phi_3)} \cdot S_1 \cdot S_2 \cdot S_3/z \\ -j \cdot e^{-1j(\phi_2+\phi_3)} \cdot S_1 \cdot S_2 \cdot S_3/z & X_2 \end{bmatrix},$$
$$(A.4)$$

where δ is written as:

$$\delta = 1 - e^{-2j \cdot \phi_2} \cdot C_1 \cdot C_2/z - e^{-2j \cdot \phi_3} \cdot C_2 \cdot C_3/z +$$
$$e^{-2j \cdot (\phi_2+\phi_3)} \cdot C_1 \cdot C_3 \cdot (1 - C_2^2)/z^2 + e^{-2j \cdot (\phi_2+\phi_3)} \cdot C_1 \cdot C_2^2 \cdot C_3/z^2$$
$$(A.5)$$

And X_1 and X_2 are written as:

$$X_1 = (C_1 \cdot z^2 + (-C_2 \cdot e^{-2j \cdot \phi_2} - C_1 \cdot C_2 \cdot C_3 \cdot e^{-2j \cdot \phi_3}) \cdot z + C_3 \cdot e^{-2j \cdot \phi_2 - 2j \cdot \phi_3} -$$
$$C_2^2 \cdot C_3 \cdot e^{-2j \cdot \phi_2 - 2j \cdot \phi_3} + C_1^2 \cdot C_2^2 \cdot C_3 \cdot e^{-2j \cdot \phi_2 - 2j \cdot \phi_3} +$$
$$C_2^2 \cdot C_3 \cdot e^{-2j \cdot \phi_2} \cdot e^{-2j \cdot \phi_3} - C_1^2 \cdot C_2^2 \cdot C_3 \cdot e^{-2j \cdot \phi_2} \cdot e^{-2j \cdot \phi_3})/z^2$$
$$(A.6)$$

$$X_2 = (C_3 \cdot z^2 + (-C_2 \cdot e^{-2j \cdot \phi_3} - C_1 \cdot C_2 \cdot C_3 \cdot e^{-2j \cdot \phi_2}) \cdot z + C_1 \cdot e^{-2j \cdot \phi_2 - 2j \cdot \phi_3} -$$
$$C_2^2 \cdot C_1 \cdot e^{-2j \cdot \phi_2 - 2j \cdot \phi_3} + C_1^2 \cdot C_2^2 \cdot C_3 \cdot e^{-2j \cdot \phi_2 - 2j \cdot \phi_3} +$$
$$C_2^2 \cdot C_1 \cdot e^{-2j \cdot \phi_2} \cdot e^{-2j \cdot \phi_3} - C_2^2 \cdot C_3^2 \cdot C_1 \cdot e^{-2j \cdot \phi_2} \cdot e^{-2j \cdot \phi_3})/z^2$$
$$(A.7)$$

The final transfer function in the z notation can be written as the generic transfer function of a second-order filter:

$$H_1 z = \frac{b_0 + b_1 \cdot z^{-1} + b_2 \cdot z^{-2}}{a_0 + a_1 \cdot z^{-1} + a_2 \cdot z^{-2}}$$
$$(A.8)$$

where a_i and b_i are a function of the coupling coefficients and phase shifts. The coefficients of the transfer function in Eq. A.8 are given by:

$$b_0 = C_0 C_1 C_4 e^{1j\phi_1 + 6j\phi_2 + 6j\phi_3} + C_3 S_0 S_4 e^{4j\phi_2 + 4j\phi_3}$$
$$(A.9)$$

$$b_1 = C_2 S_0 S_4 e^{2j\phi_2} \cdot e^{2j(\phi_2+\phi_3)} - C_0 C_2 C_4 e^{1j\phi_1} * e^{2j\phi_3} * e^{2j(\phi_2+\phi_3)} +$$
$$C_1 C_2 C_3 S_0 S_4 e^{2j\phi_3} e^{2j\phi_2 + 2j\phi_3} - C_0 C_1 C_2 C_3 C_4 e^{1j\phi_1} e^{2j\phi_2} e^{2j(\phi_2+\phi_3)} +$$
$$C_0 S_1 S_2 S_3 S_4 e^{2j(\phi_2+\phi_3)} e^{1j(\phi_2+\phi_3)} + C_4 S_0 S_1 S_2 S_3 e^{2j(\phi_2+\phi_3)} e^{1j(\phi_1+\phi_2+\phi_3)}$$
$$(A.10)$$

$$b_2 = C_1 C_2^2 S_0 S_4 e^{2j(\phi_2+\phi_3)} - C_1 S_0 S_4 e^{2j(\phi_2+\phi_3)} - C_1 C_2^2 S_0 S_4 e^{2j(\phi_2+\phi_3)} +$$
$$C_0 C_2^2 C_3 C_4 e^{1j\phi_1} e^{2j(\phi_2+\phi_3)} + C_0 C_3 C_4 e^{1j\phi_1} e^{2j(\phi_2+\phi_3)} +$$
$$C_1 C_2^2 C_3^2 S_0 S_4 e^{2j(\phi_2+\phi_3)} - \qquad C_0 C_1^2 C_2^2 C_3 C_4 e^{1j\phi_1} e^{2j(\phi_2+\phi_3)} -$$
$$C_0 C_2^2 C_3 C_4 e^{1j\phi_1} e^{2j(\phi_2+\phi_3)} - \qquad C_1 C_2^2 C_3^2 S_0 S_4 e^{2j(\phi_2+\phi_3)} +$$
$$C_0 C_1^2 C_2^2 C_3 C_4 e^{1j\phi_1} e^{2j(\phi_2+\phi_3)}$$

$$\text{(A.11)}$$

$$a_0 = e^{1j\phi_1} e^{2j(\phi_2+\phi_3)} e^{2j(\phi_2+\phi_3)} \tag{A.12}$$

$$a_1 = -C_1 C_2 e^{1j\phi_1} e^{2j\phi_3} e^{2j(\phi_2+\phi_3)} - C_2 C_3 e^{1j\phi_1} e^{2j\phi_2} e^{2j(\phi_2+\phi_3)} \tag{A.13}$$

$$a_2 = C_1 C_3 e^{1j\phi_1} e^{2j(\phi_2+\phi_3)} \tag{A.14}$$

A.2 Comparison with double ring loaded MZI without coupling between the rings
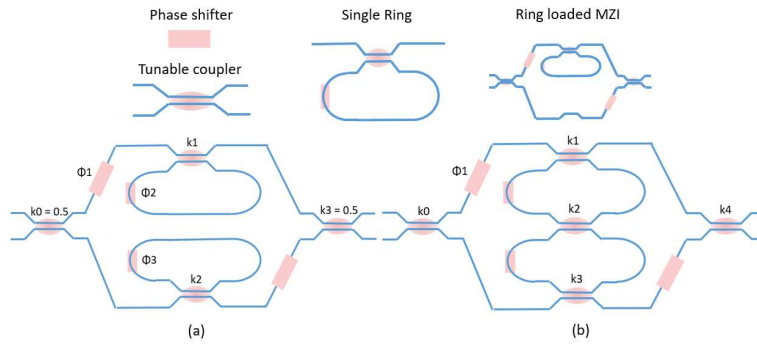
Figure A.1: Schematic drawing of the classical ring loaded MZI is shown in (a); the schematic drawing of coupled ring loaded MZI is shown in (b). The main difference between our design given in (b) and the classical double ring loaded MZI given in (a) is that the two rings are connected with a tunable coupler. It is obvious that the design in (b) could be configured to an MZI with delay length of twice the ring circumference, which is not possible with the design in (a). The phase shifters are shown as a pink box, and the tunable coupler is shown as a normal DC with a pink dot in the middle, the single add drop ring is constructed by connecting the input and output port of the tunable coupler on the same side. The input and output tunable coupler of the design in (b) is realized by a broadband balanced MZI [1] on the actual chip.

In this section, we will compare the pole-zero diagram of the classical ring loaded MZI and of our design. We demonstrate that with the same loss characteristics of the couplers, both design could cover the same area of the unit circle in the z-plane, and thus both have the potential to exactly realize second-order bandpass filter.

The ring loaded MZI in Fig. A.1(a) is a complex filter where its a_i and b_i coefficients are complex numbers, however the coupled ring loaded MZI in Fig. A.1(b) can be configured both as a real filter and as a complex filter.

In the following, we would configure our tunable filter design into the double ring loaded MZI as shown in Fig. A.1(b) and ring loaded MZI as shown in Fig. A.1(a) separately.

The coupled ring loaded MZI in Fig. A.1(b) has 6 free parameters, which are k_0, k_1, k_2, k_3, k_4 and ϕ_1. In simulation we directly modify k_i, but in the experiment the coupling factors k_i are realized using a balanced MZI with a phase shifter in each arm, and thus the tuning parameter becomes another phase shift. The coupled ring loaded MZI in Fig. A.1(b) can be configured to be a real filter where its coefficients are real numbers. In order to force the coefficients to be real, the phase shifters inside the rings need to be set to either zero (configuration I) or π (configuration II). These two situations are equivalent with each other in the spectrum response, we will discuss these two situations in Fig. A.2.

The ring loaded MZI in Fig. A.1(a) can also be a real filter, but then its configurability is limited. To implement a generic second-order bandpass filter, it needs to be configured as a complex filter where its a_i and b_i coefficients are complex numbers. The classical ring loaded MZI has 5 free parameters in simulation, which are k_1, k_2, ϕ_1, ϕ_2, ϕ_3, where the input and output couplers are set to $k_0 = k_3 = 0.5$.This architecture is proposed for realizing a bandpass filter with two all-pass filters in [2]. For most cases, a symmetric spectral response is desired, which requires $k_1 = k_2$ and $\phi_1 = -\phi_2$.

The filter synthesis equations have been accordingly rewritten for the ring loaded MZI in Fig. A.1(a), the equations (A.4) - (A.14) for the ring loaded MZI could be rewritten by setting the coupling k_2 to 0, thus $C_2 = 0$ and $S_2 = 1$. Then we compare the two types of filter in simulation. We will illustrate the programmability space of the two filter types using the Latin Hypercube sampling (LHS) method. LHS is a statistical method for generating a near-random sample of parameter values from a multidimensional distribution. In our following analysis, we use this method to explore the relationship between the parameter space and the distribution of the filter's poles and zeros in the z-plane.

For both cases, 500 sampling points are used. We plot the pole-zero map of both structures in Fig. A.2. From Fig. A.2, we can see that the poles of Fig. A.1(a) are homogeneously distributed in the z-plane. The poles within the same pair are not necessarily symmetrically positioned with respect to the Real (x) axis. The

zeros are mostly located in the unit circle. The poles for configuration I ($\phi_1 = 0$) of Fig. A.1(b) are homogeneously distributed in the right half-plane of the unit circle, while the zeros are scattered homogeneously, also in the right half of the z-plane. The poles of configuration II ($\phi_1 = \pi$) of Fig. A.1(b) are homogeneously distributed in the left half-plane of the unit circle, the zeros are scattered homogeneously also in the left-half of the z plane.

These two designs (coupled ring-loaded MZI and ring-loaded MZI) show full configurability. In the following, we would show how to get the desired coupling values for a certain filter with both complex and real filter coefficients. We will use three examples to show that these two designs are equivalent with each other, however one may perform better than the other in certain cases.
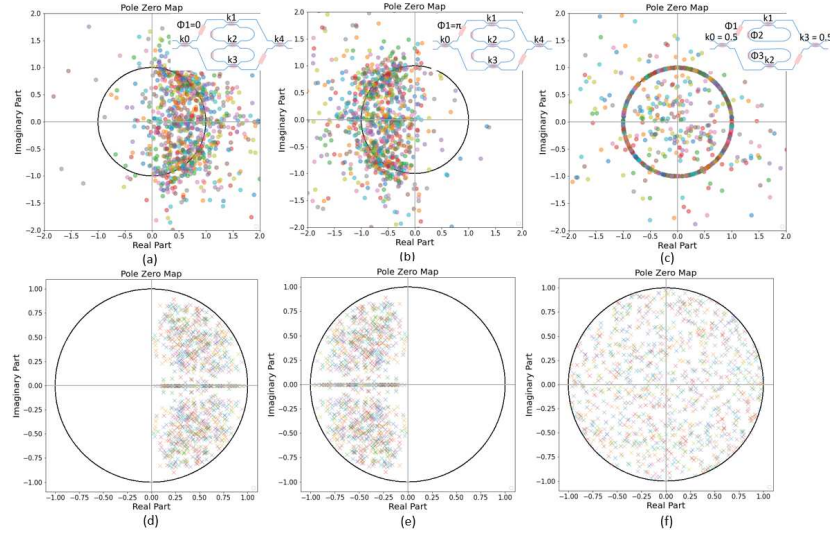
Figure A.2: Pole and zero distribution in the z-plane for a Latin Hypercube sampling of the tuning coefficients of both types of filters. The zeros of Fig. A.1(b) configuration I ($\phi_1 = 0$) are plotted in (a), the poles of Fig. A.1(b) configuration I are plotted in (e).The zeros of Fig. A.1(b) configuration II ($\phi_1 = \pi$) are plotted in (b), the poles of Fig. A.1(b) configuration II are plotted in (e).The zeros of Fig. A.1(a) are plotted in (c), the poles of Fig. A.1(a) are plotted in (f).

The following target function is used for optimizing a complex filter:

$$
\begin{aligned}
sum_{ab} = ((a_0 \cdot a_0^* - a_0'^2)^2 + (a_1 \cdot a_1^* - a_1'^2)^2 + (a_2 \cdot a_2^* - a_2'^2)^2 + \\
(b_0 \cdot b_0^* - b_0'^2)^2 + (b_1 \cdot b_1^* - b_1'^2)^2 + (b_2 \cdot b_2^* - b_2'^2)^2)^{1/2}
\end{aligned} \tag{A.15}
$$

Likewise, the target function for real filter is:

$$sum_{ab} = ((a_0^2 - a_0'^2)^2 + (a_1^2 - a_1'^2)^2 + (a_2^2 - a_2'^2)^2 +$$
$$(b_0^2 - b_0'^2)^2 + (b_1^2 - b_1'^2)^2 + (b_2^2 - b_2'^2)^2)^{1/2} \tag{A.16}$$

Let's build a first example filter with a second-order elliptical low-pass filter with 1 dB in-band ripple, 20 dB extinction ratio and the normalized edge frequencies of 0.1 π rad/sample. The a_i and b_i coefficients for such filter can be calculated with Matlab:

$$b_1 = [0.1055, -0.1245, 0.1055] a_1 = [1.0000, -1.6293, 0.7264] \tag{A.17}$$

ellip(2,1,20,0.1,'low')	b1=[1.055,-0.1245,0.1055] a1=[1,-1.6293,0.7264]
our design	ring loaded MZI
$k_0 = k_4 = 0.438, k_1 = k_3 = 0.2736$ $k_2 = 0.0869, phi_1 = 0$	$k_0 = k_3 = 0.5, k_1 = k_2 = 0.2736$ $phi_1 = -0.0790pi$ $phi_2 = -phi_3 = 0.4525pi$
$b = [(0.1055, -0.1245, 0.1013)]$	$b = [(-0.0131 + 0.1047j)$ $(-0.0153 - 0.1234j),$ $(-0.0131 - 0.1047j)]$
$a = [1, -1.6302, 0.7192]$	$a = [(0.9694 - 0.2456j)$ $(1.5794 - 0.4001j),$ $(0.7042 - 0.1784j)]$

Table A.1: Parameters For Fig. A.3

ellip(2,1,20,0.1,'low')	b1=[1.055,-0.1245,0.1055],a1=[1,-1.6293,0.7264]
solution 1	$k_0 = k_4 = 0.438, k_1 = k_3 = 0.2736$ $k_2 = 0.0869, phi_1 = 0$
solution 2	$k_0 = 0.9847, k_1 = k_3 = 0.2736, k_2 = 0.0864$ $k_4 = 0, phi_1 = 0$
solution 3	$k_0 = 0.6625, k_1 = k_3 = 0.2736, k_2 = 0.0869$ $k_4 = 0.2263, phi_1 = 0$
solution 4	$k_0 = 0.6625, k_1 = k_3 = 0.2736, k_2 = 0.0869$ $k_4 = 0.2263, phi_1 = 0$

Table A.2: 4 solutions for Fig. A.3(b)

We will now compare the filter responses of configuration I of Fig. A.1(b) and complex filter in Fig. A.1(a). After we apply the synthesis algorithm as described before, the pole-zero plot and the spectrum response are shown in Fig. A.3 for
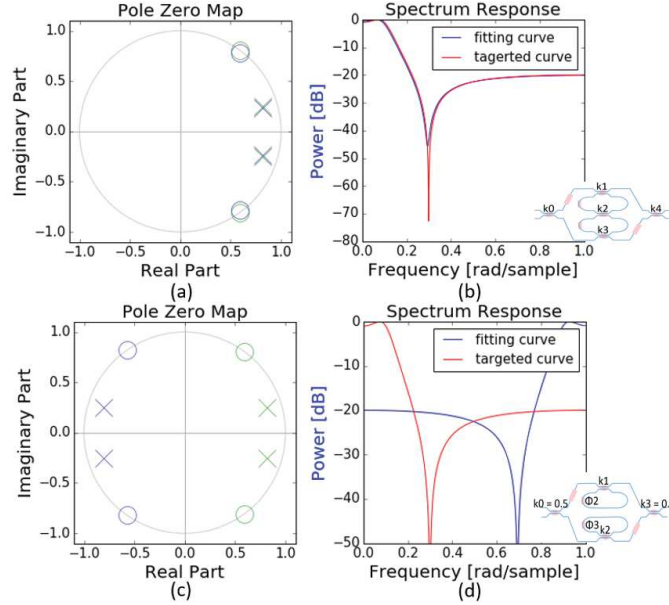
Figure A.3: The first example filter has been synthesized using both the classical and the coupled ring-loaded MZI. (a) and (c) are the pole-zero diagram of the synthesized filter, (b) and (d) are the spectrum responses of the synthesized filter compared to the targeted curve. (a) and (b) correspond to the coupled ring-loaded MZI of Fig. A.1(b), and (c) and (d) corresponds to the classical ring-loaded MZI of Fig. A.1(a).

both filter configurations.The fitting curve is the synthesized result and the targeted curve is the ideal elliptical filter response we would like to achieve.

The corresponding parameters for Fig. A.3 are given in Table A.1.According to our experiments, we found out that for normal filters such as elliptical filter, the structure is actually symmetrical, thus, certain constrains could be applied for the two designs when we try to solve for the couplings and phases. For our design shown in Fig. A.1(a), the constrains are $k_0 = k_4, k_1 = k_3 and phi_1 = 0$. For the ring loaded MZI, the constrains are $k_0 = k_3 = 0.5, k_1 = k_2 and phi_2 = -phi_3$. There are more solutions for our design when a given elliptical filter is synthesized, four solutions for the same elliptical filter in example one is shown in Table A.2.As we can see, solution 1 is the most symmetrical result, and solution 2 will simplify our design since no output coupler is needed. Filter designer might select the most stable design or the one with less wavelength dispersion.

The pole-zero plot and corresponding transfer function for the coupled ring-loaded MZI are shown in Fig. A.3(a) and Fig. A.3(b). In Fig. A.3(a), the target pole and zero positions overlap with the fitted ones, and we see a perfect correspondence for their spectrum response. The pole-zero plot and corresponding

transfer function for the conventional ring loaded MZI are shown in Fig. A.3(c-d). In Fig. A.3(c), the target poles and zeros are in the right half of the z plane, while the fitted one is in the left half plane. This corresponds to a shift of the spectral response with half a free spectral range (FSR), or a mirroring on the Nyquist frequency axis. Since the spectrum response is repeated with the FSR, so the final spectrum response of the targeted result and the fitted result show no difference with each other.

Now we consider a second filter example, let's construct a Chebyshev type II filter cheby2(2 ,20, 0.9, 'low'). The a_i and b_i coefficients are as following:

$$b_1 = [0.6326, 1.2339, 0.6326] a_1 = [1.0000, 1.0928, 0.4063] \qquad (A.18)$$

cheby2(2,20,0.9,'low')	b1=[0.6326,1.2339,0.6326] a1=[1,1.0928,0.4063]
our design	ring loaded MZI
$k_0 = k4 = 0.9962, k_1 = k_3 = 0.5937$ $k_2 = 0.2652, phi_1 = 0$	$k_0 = k_3 = 0.5, k_1 = k_2 = 0.5730$ $phi_1 = 0.8388pi$ $phi_2 = -phi_3 = 0.4077pi$
$b = [(-0.6326, 1.2339, -0.6326)]$	$b = [(-0.6124 + 0.1585j),$ $(-1.1945 + 0.3091j),$ $(-0.6124 + 0.1585j)]$
$a = [1, -1.0928, 0.4108]$	$a = [(-0.8745 + 0.4851j),$ $(-0.3734 + 0.2071j),$ $(-0.3734 + 0.2071j)]$

Table A.3: Parameters For Fig. A.4

The pole-zero diagram and the corresponding spectrum response of the coupled ring filter in configuration II ($\phi_1 = \pi$) are shown in Fig. A.4(a-b).The pole-zero diagram and the corresponding spectrum response of the conventional ring loaded MZI is shown in Fig. A.4(c-d). The corresponding parameters for Fig. A.4 is given in Table A.3.

The two circuits perform equivalently. The spectrum responses are the same if we would like to systhesize a given bandpass filter, and the only difference would lie in the configuration of the filter and its corresponding a_i and b_i coefficients.

For the third example, the a_i and b_i coefficients are not calculated from any bandpass filters. We try to set the following values to our design, $k_0 = 0.6$, $k_1 = 0.9$, $k_2 = 0.5$, $k_3 = 0.1$, $k_4 = 0.4$ and $\phi_1 = \pi$. The a_i and b_i coefficients are calculated, and then we try to fit the ring loaded MZI with the calculated coefficients, the a_i and b_i values are given in Eq. A.19:

$$b_1 = [-0.6197, 0.8582, -0.6197] a_1 = [-1.0000, 0.8944, -0.3000] \qquad (A.19)$$
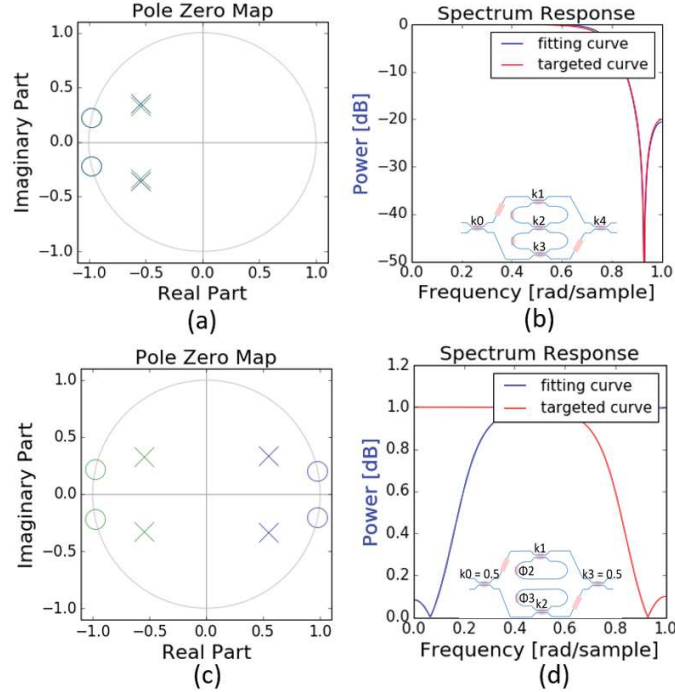
Figure A.4: The second example filter has been synthesized by both the classical and the coupled ring-loaded MZI. (a) and (c) represent the pole-zero diagrams of the synthesized filters, while (b) and (d) show their spectrum responses compared with the targeted curve. (a) and (b) corresponds to structure of the coupled ring-loaded MZI of Fig. A.1(b), and (c) and (d) corresponds to the classical ring-loaded MZI of Fig. A.1(a).

The pole-zero diagram and the corresponding spectrum response of the coupled ring-loaded MZI in configuration II are shown in Fig. A.5(a-b).The pole-zero diagram and the corresponding spectrum response of ring loaded MZI is shown in Fig. A.5(c-d). The parameters for Fig. A.5 are given in Table A.4. In this case, the fitted curve and the targeted curve in Fig. A.5(d) did not overlap with each other very well, which indicates that the ring loaded MZI could not be configured to match the double ring loaded MZI. The double ring loaded MZI thus is a better candidate for a fully programmable filter. This is important when considering uses other than bandpass filters, such as arbitrary waveform generation.

As we can see from the three examples, the a_i and b_i coefficients in our design are always real numbers. Actually if the ϕ_1 is set not be 0 or π, the a_i and b_i coefficients would also be complex number for our design. If we try to fit such complex a_i and b_i by the given the ring loaded MZI, we can not get a good fit, either. Such situation is very similar to the third example.

	b1=[-0.6197,0.8582,-0.6197]
	a1=[-1,0.8944,-0.3]
our design	ring loaded MZI
$k_0 = 0.6, k_1 = 0.9, k_2 = 0.5$ $k_3 = 0.1, k_4 = 0.4, phi_1 = pi$	$k_0 = k_3 = 0.5, k_1 = k_2 = 0.5730$ $phi_1 = 0.8388pi,$ $phi_2 = -phi_3 = 0.4077pi$
$b = [(-0.6197, 0.8582, -0.6197)]$	$b = [(-0.6021 + 0.1467j),$ $(-0.8339 + 0.2031j),$ $(-0.6021 + 0.1467j)]$
$a = [-1, 0.8944, -0.3]$	$a = [(-0.8880 + 0.4600j),$ $(-0.7942 + 0.4113j),$ $(-0.3612 + 0.1871j)]$

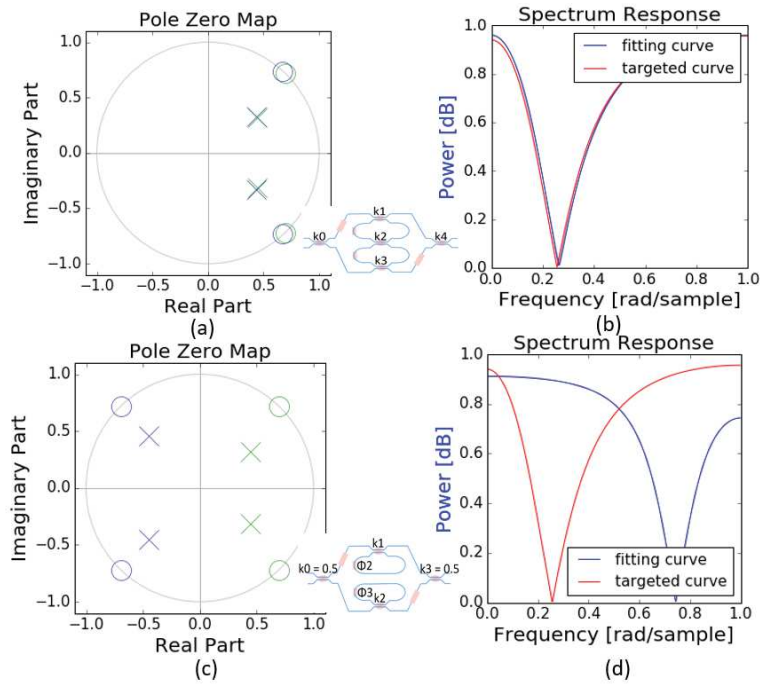*Table A.4: Parameters For Fig. A.5*

Figure A.5: The third example filter has been synthesized for both filter circuits. (a) and (c) are the pole-zero diagrams of the synthesized filters, while (b) and (d) show their spectrum responses as well as the targeted response. (a) and (b) correspond to the coupled ring-loaded MZI of Fig. A.1(b), while (c) and (d) correspond to the classical ring-loaded MZI of Fig. A.1(a).

A.3   Estimation of Q factor

In this section, we will have an estimation of the Q factor [**?**]. We assume the loss for the tunable coupler is 0.12 dB, n_g is 4.3, the loss for the phase shifter is around 0.02 dB. The resonance wavelength is 1.55 um, and the round trip length L of the ring is calculated according to the FSR measured and it is 712 um, the length of the tunable coupler is 173.4 um and the length of the heater is 50 um. The waveguide loss is estimated to be 1.3 dB/cm. r is the critical coupling and g is the amplitude attenuation coefficient.

The loss of power of the single ring is composed of waveguide loss, loss for two tunable couplers and the loss of the phase shifter, the loss of the single ring is 0.300976 dB.

$$Loss_{dB} = -10\log_{10}(P_{out}/P_{in}) = -20\log_{10}(e^{-gL}) = 20gL \cdot \log_{10}e \quad \text{(A.20)}$$

The Q factor of the single ring is calculated by the following equation:

$$Q - factor = -\pi\frac{L_{ring}}{\lambda_{res} \cdot (\ln r - g \cdot L_{ring})} \quad \text{(A.21)}$$

The Q at the critical coupling (i.e. $r = g$) is estimated to be 18184.

References

[1] Mi Wang, Antonio Ribero, Yufei Xing, and Wim Bogaerts. *Tolerant, broadband tunable 2× 2 coupler circuit.* Optics express, 28(4):5555–5566, 2020.

[2] C.K. Madsen. *Efficient architectures for exactly realizing optical filters with optimum bandpass designs.* IEEE Photonics Technology Letters, 10(8):1136–1138, 1998.